

MRI Guided Analysis of Changes in Tumor Oxygenation in Response to
Hypoxia Activated/Targeted Therapeutics

by

Shubhangi Agarwal

A Dissertation Presented in Partial Fulfillment
of the Requirements for the Degree
Doctor of Philosophy

Approved April 2017 by the
Graduate Supervisory Committee:

Vikram D. Kodibagkar, Chair
Landon J. Inge
Mehdi Nikkhah
Mark D. Pagel
Rosalind J. Sadleir

ARIZONA STATE UNIVERSITY

May 2017

ABSTRACT

A tumor is a heterogeneous combination of proliferating tumor cells, infiltrating immune cells and stromal components along with a variety of associated host tissue cells, collectively termed the tumor microenvironment (TME). The constituents of the TME and their interaction with the host organ shape and define the properties of tumors and contribute towards the acquisition of hallmark traits such as hypoxia. Hypoxia imparts resistance to cancer from chemotherapy and radiotherapy due to the decreased production of reactive oxygen species and also promotes angiogenesis, malignant progression and metastasis. It also provides a powerful physiological stimulus that can be exploited as a tumor-specific condition, allowing for the rational design of anticancer hypoxia-activated pro-drugs (HAP). Accurate evaluation of tumor oxygenation in response to therapeutics interventions at various stages of growth should provide a better understanding of tumor response to therapy, potentially allowing therapy to be tailored to individual characteristics. The primary goal of this research was to investigate the utility of prospective identification of hypoxic tumors, by two different Magnetic Resonance Imaging (MRI) based oximetry approaches, in successful treatment with hypoxia activated therapy. In the present study, I report the utility of these two techniques 1) PISTOL (Proton Imaging of Siloxanes to map Tissue Oxygenation Levels) and 2) use of a hypoxia binding T_1 contrast agent GdDO3NI in reporting the modulations of hypoxia pre and post hypoxia activated therapies in pre-clinical models of cancer. I have performed these studies in non-small cell lung cancer (NSCLC) and epidermoid carcinoma (NCI-H1975 and A431 cell lines, respectively) as well as in patient derived

xenograft models of NSCLC. Both the oximetry techniques have the potential to differentiate between normoxic and hypoxic regions of the tumor and reveal both baseline heterogeneity and differential response to therapeutic intervention. The response of the tumor models to therapeutic interventions indicates that, in conjunction with pO_2 , other factors such as tumor perfusion (essential for delivering HAPs) and relative expression of nitroreductases (essential for activating HAPs) may play an important role. The long term goal of the proposed research is the clinical translation of both the MRI techniques and aiding the design and development of personalized therapy (e.g. patient stratification for novel hypoxia activated pro-drugs) particularly for cancer.

DEDICATION

I dedicate this dissertation to my mother Neelam Singhal and my husband Shubhanshu Nagar. Without the love, support and sacrifice from my mother, this effort would not have been successful. She is the biggest source of my strength and perseverance. I am grateful for the love and unwavering support of my husband who always showed confidence in me and my work. His positive attitude and contagious smile got me through the toughest days as a Ph.D. student.

ACKNOWLEDGEMENTS

I would like to thank the very many people who have guided me in honing my scientific career and personal life over the past 4.5 years of my Ph.D. journey. Firstly, I would like to thank my Ph.D. advisor and mentor, Prof. Vikram D. Kodibagkar, for improving my research skills and for being a constant pillar of support. His extraordinary skill of encouraging his students to conduct quality scientific research has generated a passion in me for conducting impactful research. I shall always be thankful to him for giving me the opportunity to do great research and installing a passion for solving scientific problems. His perspective towards science will always be a constant source of inspiration for me.

I wish to express my sincere thanks to Dr. Landon J. Inge at Norton Thoracic Institute for his guidance, support and encouragement. I am grateful to him for providing the PDX models used in this work. I also thank Dr. Adam Patterson and Dr. Jeff Smaill at The University of Auckland for providing the prodrug used in this work and their valuable input. I would like to thank my dissertation committee members Dr. Mark D. Pagel, Dr. Rosalind Sadleir, and Dr. Mehdi Nikkhah for their guidance and inputs over the course of my Ph.D. at ASU. Sincere thanks to Dr. Yanqing Tian and Dr. Xiangxing Kong for synthesis of the MR contrast agent. In addition, a thank you to Dr. Greg Turner for access to the ASU-BNI Pre-clinical imaging center. I will always be thankful to Mr. Qingwei Liu for teaching me how to operate the MR imaging system and for being always available to clarify my doubts and troubleshooting any issues that I encountered while running my experiments. Sincere thanks to Christine Howison (University of

Arizona) for teaching me intravenous injection without which I would not have been able to generate half of the data for my studies.

I joined ASU in August 2012 and from the very first day Dr. Rohini Vidya Shankar was there to help me as I began this journey. She provided constant support, intellectual as well as emotional, and was an excellent scientist with whom I could discuss research ideas. I would also like to thank Alex Cusick for being the wonderful human being that he is and I am thankful for his friendship that I will cherish all my life. I had the pleasure of mentoring and interacting with many undergraduate students (a special mention for Eugene, Courtney, Carlos, Troy and Richard) and I would like to thank them for giving me a chance to learn from them. Over the course of my research experience at ASU, I had a chance to meet some of the most smart and hard-working colleagues and was lucky enough to form a bond of friendship with them. In particular, I would like to thank Vimala Bharadwaj, Sai Pavan Taraka Grandhi, Nutandev Bikkamane Jayadev, Swathy Sampath Kumar, Aprinda Indahlastari, Caroline Addington, Priya Nair and Dipankar Dutta. A sincere thanks to the administration staff at SBHSE, especially Ms. Laura Hawes, Ms. Tamera Cameroon, and Ms. Tomi St. John, for being supportive and efficient in taking care of all the administrative tasks.

Lastly, and most importantly, I would like to thank my family. Everything that I have and will achieve in my life is because of the undying love and support from my family. They provide me the inspiration and motivation to become the best version of myself and instill in me the confidence that I can achieve anything with dedication and hardwork.

TABLE OF CONTENTS

	Page
LIST OF TABLES.....	x
LIST OF FIGURES.....	xi
CHAPTER	
1 INTRODUCTION	1
1.1 Tumor Microenvironment.....	1
1.1.1 Tumor vasculature and hypoxia	2
1.1.2 Significance of hypoxia.....	5
1.1.3 Hypoxia activated bioreductive pro-drugs	7
1.2 Magnetic Resonance Imaging.....	13
1.2.2 Paramagnetic relaxation enhancement	15
1.3 Assessment of tissue oxygenation.....	18
1.3.1 Existing methods for measurement of pO ₂	19
1.3.2 Quantitative MR oximetry using PISTOL.....	22
1.3.3 Qualitative MR oximetry using GdDO3NI	25
2 QUANTITATIVE ASSESSMENT OF CHANGES IN TUMOR OXYGENATION	
POST HYPOXIA ACTIVATED THERAPY USING PISTOL.....	27
2.1 Abstract	27
2.2 Introduction	28
2.3 Materials & Methods.....	29
2.3.1 Animal models.....	29

CHAPTER	Page
2.3.2 Hypoxia-targeted therapy	29
2.3.3 Tumor Volume Measurements	30
2.3.4 MR imaging protocol.....	30
2.3.5 Tumor collection and immunohistochemical analysis	33
2.3.6 Edema fraction analysis.....	34
2.3.7 Data analysis.....	34
2.4 Results	35
2.4.1 Baseline tumor oxygenation and edema fraction	35
2.4.2 Treatment response.....	37
2.4.3 In-vivo Imaging	38
2.4.3.1 In-vivo Imaging: Treatment response of epidermoid carcinoma A431	38
2.4.3.2 In-vivo imaging: Treatment response of non-small cell lung cancer NCI-H1975.....	43
2.4.4 Edema fraction.....	47
2.4.5 A431 vs. NCI-H1975 tumor oxygenation	51
2.5 Discussion	56
3 QUALITATIVE MRI ASSESSMENT OF CHANGES IN TUMOR HYPOXIA POST HYPOXIA-TARGETED THERAPY USING A NOVEL HYPOXIA-TARGETING T₁ CONTRAST AGENT-GdDO3NI.....	62
3.1 Abstract	62
3.2 Introduction	63

CHAPTER	Page
3.3 Materials and Methods:.....	65
3.3.1 Relaxivity measurements.....	65
3.3.2 Animal models.....	66
3.3.3 Hypoxia activated treatment.....	66
3.3.4 In-vivo MR imaging.....	67
3.3.5. Immunohistochemical analysis of hypoxia.....	69
3.3.6 Edema fraction analysis.....	70
3.3.7 Data analysis.....	70
3.3.8 Image registration.....	72
3.4 Results.....	73
3.4.1 Baseline tumor hypoxia and edema fraction.....	73
3.4.2 Treatment response.....	76
3.4.2.1 Tumor volume and edema fraction.....	76
3.4.2.2 Treatment effect on hypoxic fraction and intensity.....	77
3.4.3 Kinetics of GdDO3NI in NCI-H1975 tumors.....	78
3.4.4 Co-registration of MRI and IHC images.....	80
3.5 Discussion.....	85
4 MRI ASSESSMENT OF CHANGES IN HYPOXIA AND OXYGENATION IN PATIENT DERIVED XENOGRAFT MODELS OF NSCLC POST HYPOXIA ACTIVATED THERAPY.....	89
4.1 Abstract.....	89

CHAPTER	Page
4.2 Introduction	90
4.3 Materials and Methods	91
4.3.1 Animal models.....	91
4.3.2 Hypoxia activated treatment.....	92
4.3.3 MR imaging protocol.....	93
4.3.4 Data analysis.....	94
4.4 Results	95
4.4.1 Baseline tumor oxygenation and edema fraction	95
4.4.2 Treatment response.....	98
4.4.2.1 Tumor volume and edema fraction	98
4.4.2.2 Treatment induced changes in oxygenation.....	99
4.4.2.3 Hypoxic fraction and intensity.....	103
4.5 Discussion	105
5 CONCLUSIONS & FUTURE DIRECTIONS	109
REFERENCES	118
APPENDIX.....	142
A MORE BULLETS FOR PISTOL: LINEAR SILOXANE REPORTER PROBES FOR ¹ H OXIMETRY	142
B PERMISSION TO USE FIGURES	159
C APPROVAL DOCUMENTS FOR STUDIES INVOLVING ANIMAL SUBJECTS	163

LIST OF TABLES

Table	Page
2.1: Tumor Doubling Times of A431 and NCI-H1975 Treated Tumors.....	38
2.2: Mean Oxygenation of A431 and NCI-H1975 Xenograft Tumor Models from day 0 - 15.	47
2.3: Mean Edema Fraction of A431 and NCI-H1975 Xenograft Tumor Models.....	50
2.4: Mean Hypoxic Fraction of A431 and NCI-H1975 Treated Tumors	55
4.1: Mean Oxygenation of M112004 and M1005 PDX Tumor Models Pre and Post- Treatment.	102
A.1: Calibration Constants of HMDSO at 7 T and 9.4 T.	148
A.2: Calibration Constants of OMTSO at 4.7 T, 7 T and 9.4 T.	151
A.3: Calibration Constants of PDMSO at 7 T.	153

LIST OF FIGURES

Figure	Page
1.1: The Hallmarks of a Tumor Microenvironment.....	2
1.2: Representation of Vasculature in Normal Tissues and Tumors	4
1.3: The Schematic Presentation of Hypoxia Mediated Cycles in a Tumor.	6
1.4: The Mechanism of Action of Tirapazamine.	10
1.5: Structure and Mechanism of Action of TH-4000.	11
1.6 Structure of the Hypoxia Activated Pro-drugs Discussed in this Chapter.....	11
1.7: Factors Influencing the Solvent Water Relaxation and Strategies for Controlling Rotational Dynamics of Multimeric, Targeted Contrast Agents	18
1.8: A) Chemical Structure of Hexamethyldisiloxane (HMDSO).....	23
1.9: Schematic Representation of the Pulse Sequence for PISTOL.	24
1.10: Structure of GdDO3NI.....	26
2.1: The Representation of Experiment Set-up.....	32
2.2: Schematic Representation of the Study Protocol.....	32
2.3: Schematic Representation of the Imaging Protocol.....	32
2.4: Representation of The Image Segmentation Procedure for Data Analysis..	33
2.5: The Baseline Mean Tumor Oxygenation (A) and Baseline Edema Fraction (B) of A431 and NCI-H1975 Tumors.	36
2.6: The Mean Normalized Tumor Volumes of A431 and NCI-H1975 Tumor Treated with TPZ, PR509, PR509E and Untreated Control and Their Statistical Differences.	38

Figure	Page
2.7: The Oxygenation Changes of Untreated Control and TPZ Treated A431 Cohorts and Their Statistical Comparison.....	40
2.8: The Oxygenation Changes of PR509 and PR509E Treated A431 Cohorts and Their Statistical Comparison.	41
2.9: Overlay of the Reference T ₂ -weighted Tumor Image and the Respective pO ₂ Map from Day 0 – 15 for All the Four A431 Cohorts.	42
2.10: The Oxygenation Changes of Untreated Control and TPZ Treated NCI-H1975 Cohorts and Their Statistical Comparison.	44
2.11: The Oxygenation Changes of PR509 and PR509E Treated NCI-H1975 Cohorts and Their Statistical Comparison.....	45
2.12: Overlay of the Reference T ₂ -weighted Tumor Image and the Respective pO ₂ Map from Day 0 – 15 for all the Four NCI-H1975 Cohorts.	46
2.13: Treatment Induced Changes in Edema Fraction of A431 Tumors.	48
2.14: Treatment Induced Changes in Edema Fraction of NCI-H1975 Tumors.....	49
2.15: Treatment Induced Changes in Edema Fraction A431 vs. NCI-H1975.	50
2.16: A431 vs. NCI-H1975 Oxygenation.	52
2.17: The Mean Hypoxia Fractions of A431 and NCI-H1975 Cohorts, Measured at Day 15 Post-treatment, by Pimonidazole Staining.....	54
2.18: Pimonidazole Stained NCI-H1975 Tumor Sections Treated with (a) Untreated (b) TPZ (c) PR509 and (d) PR509E.	55

Figure	Page
2.19: Pimonidazole Stained A431 Tumor Sections Treated with (a) Untreated (b) TPZ (c) PR509 and (d) PR509E.....	56
3.1: Co-Registration and Hypoxic Thresholding of IHC and MR Percentage Enhancement Images.	64
3.2: Schematic Representation of the Study Protocol.....	68
3.3: Schematic Representation of the Imaging Protocol.....	69
3.4: Representation of the Image Segmentation Procedure for Data Analysis.....	72
3.5: Relaxivity of GdDO3NI at 7 T, in DI.....	74
3.6: Baseline Distribution and Intensity of Hypoxia in NCI-H1975 Tumors.....	75
3.7: Correlation Analysis Between Baseline Characteristics of Hypoxia and Tumor Volume.....	75
3.8: Mean of Normalized Tumor Volumes of Treated and Untreated Control NCI-H1975 Tumors.....	76
3.9: The Edema Fraction Before and After Treatments.....	77
3.10: The Treatment Induced Changes in Distribution and Intensity of Hypoxia.....	78
3.11: The Kinetics of Mean Agent Concentration for Normoxic and Hypoxic Regions in NCI-H1975 Tumors.....	79
3.12: The Correlation Analysis between Pimonidazole Stained Tumors vs. MR Obtained Hypoxia Maps.....	81

Figure	Page
3.13: Percentage Enhancement Maps of a Single Slice of Untreated Control NCI-H1975 Tumor at 125 Minutes Post-injection of GdDO3NI with Respect to Pre-injection Intensity.....	82
3.14: Percentage Enhancement Maps of a Single Slice from the Same NCI-H1975 Untreated Tumor (at a Distance of 5 mm from the Previous Slice) at 125 Minutes Post-Injection of GdDO3NI with Respect to Pre-injection Intensity.....	83
3.15: Percentage Enhancement Maps of a Single Slice of TPZ Treated NCI-H1975 Tumor at 125 Minutes Post-injection of GdDO3NI with Respect to Pre-injection Intensity.....	84
4.1: Schematic Representation of the Imaging Protocol.....	94
4.2: Baseline Mean Oxygenation of M112004 and M1005 PDX Tumors.	96
4.3: The Baseline Distribution and Intensity of M112004 and M1005 PDX Tumors.....	97
4.4: Baseline Mean Edema Fraction of M112004 and M1005 PDX Tumors.	97
4.5: The Mean of Normalized Tumor Volumes Post-treatment of M112004 and M1005 PDX Tumors.	98
4.6: The Mean Edema Fraction Post-treatment of M112004 and M1005 PDX Tumors..	99
4.7: The Changes in Oxygenation Post Therapy in M1005 PDX Tumors	100
4.8: The Changes in Oxygenation Post Therapy in M112004 PDX Tumors	101
4.9: The Changes in Hypoxic Fraction Post Therapy in M112004 and M1005 PDX Tumors.....	103

Figure	Page
4.10: The Changes in Hypoxic Intensity Post Therapy in M112004 and M1005 PDX Tumors.	104
A.1: Neat HMDSO R_1 Dependence on pO_2 at Different Temperatures at 7 T.....	149
A.2: Neat OMTSO R_1 Dependence on pO_2 at Different Temperatures at 7 T.	150
A.3: Neat PDMSO R_1 Dependence on pO_2 at 7 T.	152
A.4: The Comparison of Simulated Error in pO_2 Determination for Neat (A) HMDSO, (B) OMTSO and (C) PDMSO with a 1°C Change in Temperature in a Hypoxia Relevant pO_2 Range at 37°C at 4.7, 7 and 9.4 T.	154

CHAPTER 1

INTRODUCTION

1.1 Tumor Microenvironment

Cancer is the leading cause of death in the world and years of research has brought into light the complexity of the tumors and their transformations [1]. Cancer is a collective organization of malignant tumor cells and non-malignant tumor promoting cells. Together these constituents form the tumor microenvironment which differs significantly from the surrounding host tissue as it contains several modified cellular and molecular signatures [2-4]. These signatures or “hallmarks” [5] define the properties of a tumor and distinguish it from the host both morphologically and functionally (figure 1.1). The tumor microenvironment is a heterogeneous combination of proliferating malignant cells, infiltrating inflammatory cells, cancer associate fibroblast cells, endothelial cells, pericytes, adipocytes, extracellular matrix. The interaction of these components shapes and defines the pathophysiology of malignant tumors and contribute at varying degree towards the acquisition of hallmark traits such as decreased apoptotic potential, angiogenesis, resistance to treatment, metastasis, invasion and hypoxia [3-15]. The components of the tumor stroma are initially recruited from the host tissue and reprogramed to take various tumor promoting roles as the tumor progresses [15]. In order to curb the growing tumor it is necessary to fight the environment that is contributing to its growth [3, 4, 9, 16]. These underlying signatures of the tumor microenvironment can be exploited for diagnosis and treatment of a tumor by developing novel targeted drugs and drug delivery agents for tumor specific accumulation and action [17-22].

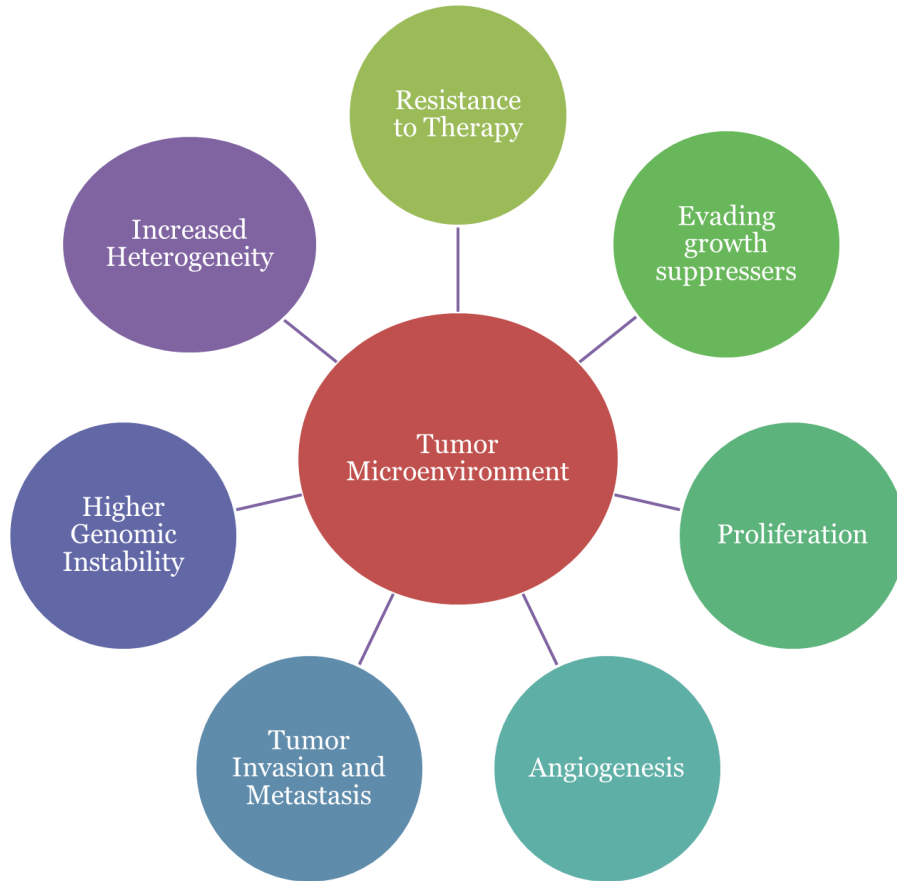


Figure 1.1: The hallmarks of a tumor microenvironment. The non-malignant and malignant cells comprising the TME form a complex organ, which is regularly recruiting and transforming cells to acquire and maintain the hallmark characteristics for its survival and progression. Modified from reference [5]

1.1.1 Tumor vasculature and hypoxia

The vasculature in normal tissues is a well-organized network of arteries, veins and capillaries that are maintained by well-regulated expression of pro- and anti-angiogenic factors. A functioning lymphatic system along with the efficient vasculature helps in draining the excess build-up of fluid and removal of waste metabolic products from the interstitium [23]. The highly proliferating tumor cells quickly outgrow their blood supply which leads to formation of regions with hypoxia ($\leq 10\text{-}15$ torr pO_2) [4, 5, 8, 10, 11, 24-31]. The lack of oxygen leads to hypoxia-induced expression of hypoxia

inducible factor- α (HIF1 α) which up-regulates pro-angiogenesis factors such as vascular endothelial growth factor-A (VEGF-A) and vascular endothelial growth factor receptor 2 (VEGFR2) [32-35]. The poorly regulated expression of angiogenesis growth factors within the tumor microenvironment such as VEGF induces formation of neo-vasculature that is extremely inefficient in structure and function. The fundamental properties of a tumor vasculature are: 1) hyper permeability, 2) immature (lack of pericyte coverage), 3) chaotic organization, 4) deteriorating diffusion geometry, 5) lack of blood vessel hierarchy and 6) arteriovenous shunts (figure 1.2 A). The discontinuous diameter of the vessels along with abrupt blunt ends, abnormal budes and irregular shape results in inefficient delivery of the blood and nutrients to the tumors [36, 37]. Paired with a poor lymphatic system, this leads to fluid and waste build up in the vessels and tumors which leads to increase interstitial fluid pressure [38, 39]. The tumor vasculature is well organized and mature at the tumor-host interface and deteriorates as we move towards the center of the tumors. As the tumor grows, the vascular density decreases and leads to formation of regions with necrosis.

Depending on the characteristics of tumor vasculature, hypoxia can be subdivided into chronic (diffusion limited) and acute (perfusion limited) (figure 1.2 B). The capacity of oxygen to diffuse is limited to 100-150 μm [40] from the nearest blood vessels due to consumption: regions that are farther than this diffusion limit develop chronic hypoxia. The transient changes in blood flow due to tumultuous, collapsed and dilated blood vessels and abrupt blunt ends leads to development of transient, acute hypoxia in the tumors.

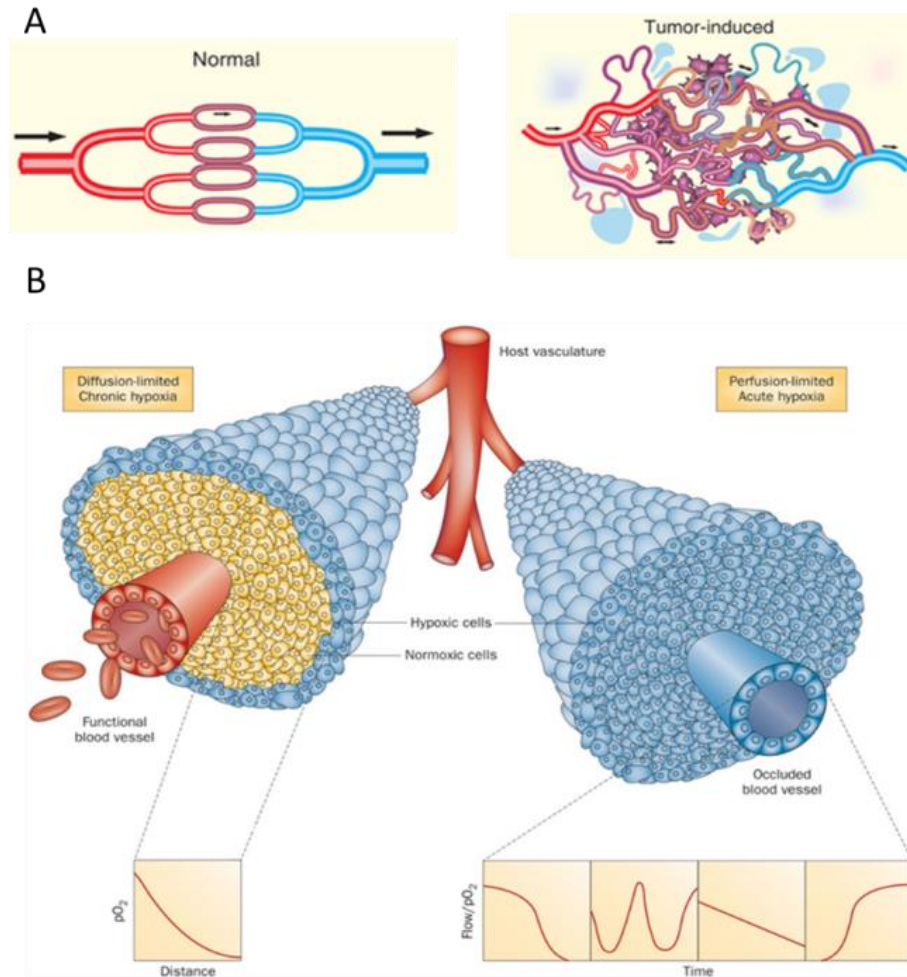


Figure 1.2: Representation of vasculature in normal tissues and tumors. (A) The vasculature in normal tissues is well organized with balanced hierarchy and a functional lymphatic system. In tumors the vasculature is tumultuous, lacking vascular hierarchy, underdeveloped with improper lining of the pericytes and smooth muscle cells leading to leaky vessels. The inefficient blood vessels are not capable of meeting the increased requirement of oxygen and nutrients by the tumor cells which leads to formation of hypoxia. (B) The combination of poor vasculature network and highly proliferating cells leads to formation of chronic or diffusion limited hypoxia as the oxygen is not able to diffuse further than 100-150 μm in distance. Conversely, presence of abrupt blunt ends, arteriovenous shunts, blockages and temporary collapse of vessels causes acute or perfusion limited hypoxia. Reproduced from [22] and [21].

1.1.2 Significance of hypoxia

Several studies have highlighted the direct or indirect contribution of hypoxia towards the acquisition and regulation of hallmark properties of tumors. Hypoxia is one of the most prominent features of a tumor's microenvironment, that varies between different tumor types and plays an important and complex role in the regulation of many hallmark characteristics of a tumor, thus making its evaluation crucial for understanding a tumor's characteristics and for the development of a personalized treatment protocol [10, 41-47]. Hypoxia is known to promote angiogenesis, invasion and metastasis and its presence is considered a marker for poor clinical prognosis [5, 11, 28, 41-46, 48-50]. Hypoxia also promotes resistance to apoptosis, chemotherapy and radiation thus limiting the number of potentially useful therapeutic options. The persistence of hypoxia leads to selection of genetic variants that are able to adapt and grow in the stressful environment and develop resistance to therapy. Hypoxia provides a powerful physiological stimulus that can be exploited as a tumor-specific condition, allowing for the rational design of hypoxia targeted therapies as well as hypoxia imaging techniques [18, 48, 51-57]. Recent studies have shown that cancer stem cells,(neoplastic cells or tumor initiating cells) that may play a role in various tumor promoting factors such as metastasis, invasion and resistance to therapy [58-64], are more likely to be present in hypoxic regions and that hypoxia aids in their regulation and maintenance [65-68]. The extent and severity of hypoxia can be spatially heterogeneous in tumors and fluctuate over time as the disease progresses [69-72]. Figure 1.3 depicts the cycle of events mediated by hypoxia that makes it a prevalent condition for tumors.

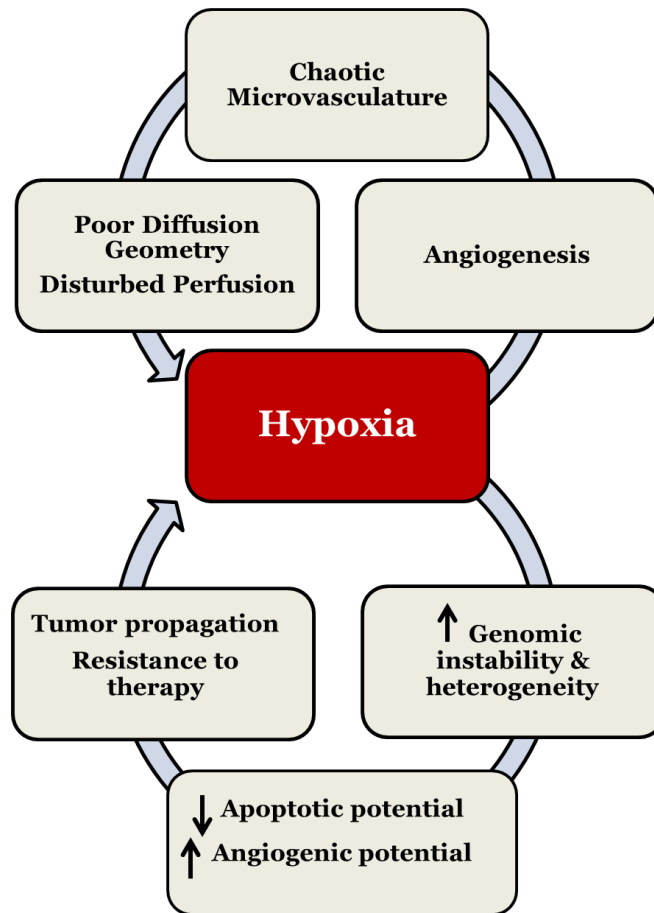


Figure 1.3: The schematic presentation of hypoxia mediated cycles in a tumor. As the tumor out-grows its initial vasculature, regions with hypoxia develop. Hypoxia in turns regulates the expression of pro-angiogenesis factors that lead to formation of neovasculature which is chaotic in nature. The consequence of chaotic and underdeveloped vasculature is an increase in regions of hypoxia, thus the vicious cycle continues. The chronic development of hypoxia leads to increase in mutations and clonal selection of variants with decreased apoptotic potential and increased angiogenic potential thus resulting in tumor propagation and resistance to therapy. Image modified from [73].

The outstripping of nutrients and oxygen supply in neoplasms due to the inability of vasculature to meet the increased demand by proliferating cells leads to formation of hypoxia, which results in induction of angiogenesis. The unchecked expression of

angiogenesis factors lead to development of chaotic vasculature which in turn increases the presence of hypoxia and thus the cycle continues (figure 1.3).

The various contributions of hypoxia can be summarized as follows:

1. Resistance to radiotherapy due to lack of the reactive oxygen species,
2. Hypoxic stress slows the proliferation of cancer cells leading to development of resistance against chemotherapeutic drugs that target highly proliferating cells. The associated lack of blood vessel supply to the hypoxic regions also makes it difficult for the drugs to penetrate into these regions.
3. Hypoxia induces increase in genomic instability (high mutation frequency) and heterogeneity,
4. Due to the increased stress in the hypoxic microenvironment, the cells that survive are usually clonal variants with anti-apoptotic mutations and increased aggressiveness,
5. Hypoxia also contributes towards increased tumor survival by evading the immune response,
6. Hypoxia is known to upregulate factors that promote angiogenesis, tumor invasiveness, malignancy and metastasis.

1.1.3 Hypoxia activated bioreductive pro-drugs

Targeted cancer therapeutics has garnered increased interest in the last few decades as a means to selectively target the tumor regions with increased toxicity. The plethora of tumor promoting factors induced by hypoxia indicates that selective targeting

of hypoxic regions in the tumors has the potential to improve the therapeutic efficacy. Hypoxia was recognized as a high-priority target for the development of cancer selective therapeutics and was first demonstrated by hypoxia selective toxicity of nitroimidazoles [74]. Hypoxia targeted therapeutics are mainly classified into hypoxia activated bio-reductive pro-drugs or HAPs and drugs for molecular targeting of hypoxia specific pathways such as HIF pathways [54]. The focus of this dissertation will be the application of HAPs and their dependence and effect on the tumor hypoxia. Hypoxia activated bioreductive pro-drugs are a category of hypoxia targeted therapies that selectively target the hypoxic regions by getting reduced into their toxic counterparts known as ‘effectors’ in the presence of hypoxia and exert toxicity via various mechanisms.

An ideal HAP should have the following fundamental properties : 1) ability to reach the hypoxic regions of the tumor that are contributing towards tumor resistance and are particularly present towards the center of the tumor, 2) a higher hypoxic threshold for conversion into the toxic counterpart, 3) ability to impart toxicity to the hypoxic cells especially the non-proliferating population within the hypoxic fraction and 4) ability to exert a bystander effect towards the less hypoxic and proliferating tumor population. Other important characteristics include high stability and solubility of the drug. Apart from these intrinsic properties of the HAPs, the extrinsic properties are more tumor type dependent, such as the presence of reductases that would convert the pro-drug to its toxic counterpart and sensitivity of the tumor cells towards the toxic metabolite. These

properties determine the efficacy of HAP in a tumor model and thus should be considered while developing a novel HAP.

A typical HAP is composed of three components: a trigger, linker and an effector [75]. The trigger determines the hypoxic selectivity and the hypoxic threshold for the pro-drug conversion and the linker makes sure the drugs stays deactivated in a normoxic environment. The effector imparts toxicity to the hypoxic cells and then exerts its toxicity to surrounding cells via bystander effect. The clinical relevance of hypoxia has led to the development of several HAPs, for example, PR-104 [76], AQ4N [77], EO9 [78], TH-302 [79], TH-4000 [80, 81] and tirapazamine [82]. A few of these HAPs are discussed in detail below.

The efficacy of two HAPs, tirapazamine and PR509, were evaluated in this study. Tirapazamine, (3-amino-1,2,4-benzotriazine 1,4-N-oxide, TPZ [83-88], figure 1.4) is a prototypical HAP that was developed in mid-1980s. The agent shows selective cytotoxicity to hypoxic cells and causes DNA single and double strand breaks. TPZ gets activated (under mild hypoxia) by the one-electron reduction activation by cytochrome P450 reductase to form an intermediate radical. In the absence of oxygen, the radical gets converted to hydroxyl or benzotriazinyl radicals that cause DNA double of single strand breaks. In the presence of oxygen, the intermediate gets re-oxidized to form the parent compound. TPZ can also undergo 2-electron reduction pathway via NQO1 to form mono-N-oxide with very low toxicity (figure 1.4). TPZ showed promising results in the preclinical studies [89] and phase I and II trials in combination with cisplatin, etoposide and radiotherapy, but failed in phase III studies [90].

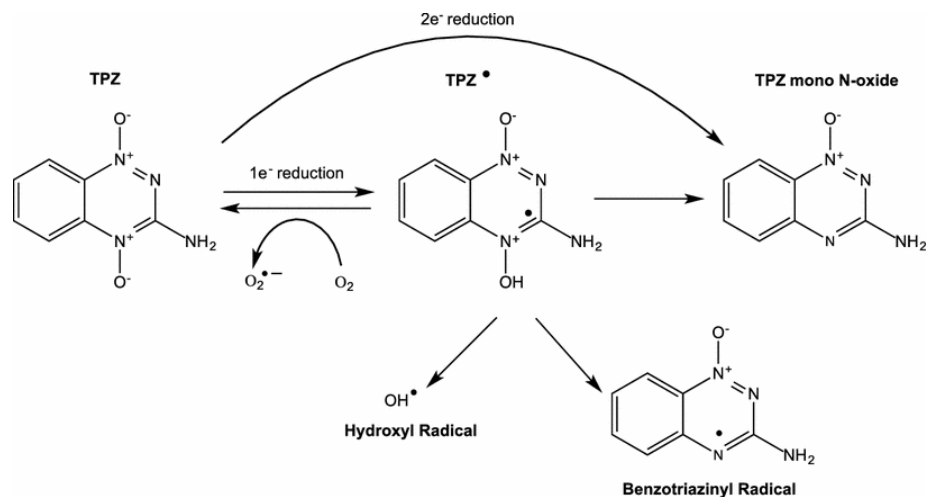


Figure 1.4: The mechanism of action of tirapazamine. TPZ gets activated (mild hypoxia) by the one-electron reduction activation by cytochrome P450 reductase to form an intermediate radical. In the absence of oxygen, the radical gets converted to hydroxyl or benzotriazinyl radicals that cause DNA double or single strand breaks. In the presence of oxygen, the intermediate gets back oxidized to form the parent compound. TPZ can also undergo 2-electron reduction pathway via NQO1 to form mono-N-oxide with very low toxicity Reproduced from [54] (<http://creativecommons.org/licenses/by/4.0/>).

PR509 is a novel hypoxia-activated bioreductive pro-drug that gets converted to its toxic counterpart PR509E in hypoxic regions [91]. It is an irreversible multikinase inhibitor that targets the EGFR family of kinases and was developed by a group of scientists at the University of Auckland led by Dr. Adam Patterson. Currently, an analog of PR509 called TH4000 [80, 81] (HypoxinTM, Threshold Pharmaceuticals, San Francisco, USA) is currently undergoing phase II clinical trial in advanced NSCLC and metastatic squamous cell carcinoma of the head and neck. The mechanism of action of PR509 is similar to that of TH4000 (figure 1.5). Briefly, TH4000 undergoes 1 electron reduction in regions with hypoxia and gets converted to a nitro radical anion that undergoes further fragmentation to form the toxic product. The pre-clinical studies with

PR-610 have shown its activity against NSCLC with wild-type and mutant EGFR [54, 80, 81].

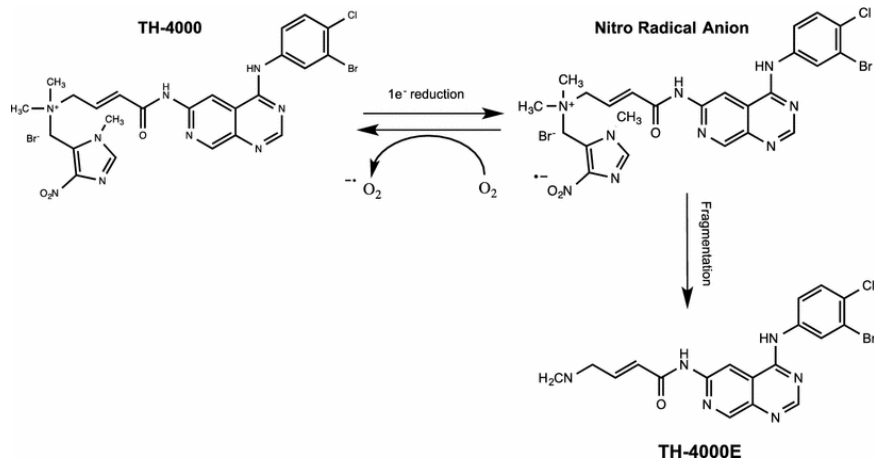


Figure 1.5: Structure and mechanism of action of TH-4000. TH-4000 gets converted to a nitro radical anion via one electron reductases in the presence of hypoxia. The nitro radical anion undergoes further fragmentation to form the effector TH4000E that causes inhibition of the EGFR family of kinases. PR509 is an analog of TH4000 with chlorine replaced with fluorine. Reproduced from [54] (<http://creativecommons.org/licenses/by/4.0/>).

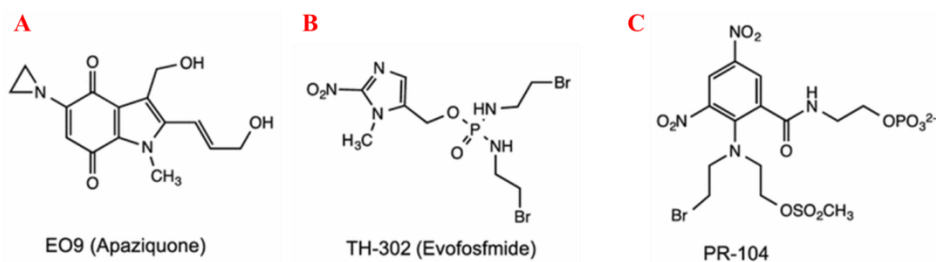


Figure 1.6 Structure of the hypoxia activated pro-drugs discussed in this chapter. Reproduced from [54] (<http://creativecommons.org/licenses/by/4.0/>).

The HAPs can also be broadly classified on the basis of their mechanism to impart toxicity to the hypoxic regions. Typically the toxic counterpart of the HAP either causes DNA damage via introducing breaks in DNA or inhibition of cell proliferation via

kinase inhibiting pathways. The DNA damaging agents have a cytotoxic effect resulting in the death of cancer cells while kinase inhibiting agents induce antiproliferative effects resulting in cytostasis [92]. The goal of our study was to investigate the effect of TPZ and PR509 (changes in tumor volume as well as oxygenation) in pre-clinical tumor models as the drugs represent both the class of HAPs respectively. We also studied the effect of PR509E in order to evaluate the role of molecular targets (EGFR in the case of PR509) in determining the effect of the toxic effectors as their efficacy is independent of the presence of hypoxia.

EO9 (apaziquone [78, 93]) is an indolequinone derivative of mitomycin C that causes generation of DNA damaging species (figure 1.6 A). The drug showed selective toxicity to hypoxic cells that are devoid of NAD(P)H:quinone oxidoreductase 1 (NQO1, a cytosolic flavoprotein), but is also showed toxicity to aerobic cells that express high levels of NQO1. EO9 showed poor penetration and fast degradation and thus failed to show good results in the clinical trials with NSCLC, pancreatic, breast, colorectal and gastric cancers.

TH-302 (evofsoamide [79, 94] (figure 1.6) is a recently developed 2-nitroimidazole containing HAP that showed great potential in the pre-clinical [95, 96] as well as clinical trials, but failed in the phase III trials in pancreatic adenocarcinoma and soft tissue sarcoma and was discontinued in phase II trials of NSCLC [55]. The TH-302 effector causes DNA cross-linking and cell cycle arrest [97].

PR-104 [76] is a nitroaromatic compound that causes DNA cross-linking in hypoxic cells via reduction by cytochrome P450 reductase (figure 1.6 C). The agent also

shows toxicity to aerobic cells due to the oxygen-independent reduction by AKR1C3 (aldo-ketoreductase 1C3). The PR-104 performed well in the pre-clinical [98] studies and phase I/II clinical trials[99] but unfortunately failed to show survival benefit and were discontinued [55].

1.2 Magnetic Resonance Imaging

MRI is a non-invasive tomographic imaging technique based on the phenomenon of nuclear magnetic resonance (NMR). MRI utilizes the fundamental property of nuclear spin to detect measurable signals arising from bulk nuclear spin polarization in presence of an external magnetic field (nuclear paramagnetism). Two- and three-dimensional images of the body with high spatial resolution and contrast can be generated using MRI by acquiring these signals in the presence of position encoding gradients [100]. Advances in the last three decades have led to a substantial improvement in the quality of the MR images generated with higher signal to noise ratio and sensitivity.

Signal in MRI is generated from the electromagnetic radiations emitted when a nuclear spin is exposed to static and oscillating magnetic fields. Hydrogen atom contains a single proton with $+1/2$ and $-1/2$ nuclear spin states which results in a bulk magnetic moment in presence of a strong external magnetic field. This forms the basis for proton MRI that is widely prevalent in clinical settings. The human body is $\sim 70\%$ water by body weight and (along with hydrogen from fat) provides plenty of hydrogen protons that can be used as NMR active nuclei. Image contrast is defined as the ability to discriminate tissues based on their relative brightness and darkness on an image. Contrast obtained in the MRI images depends on several intrinsic properties of the tissue such as proton

density (ρ), diffusion, perfusion, spin-lattice relaxation time (T_1), spin-spin relaxation time (T_2), observed spin de-phasing time (T_2^*), magnetization transfer and chemical exchange effects. The images are generated by using specific “weighting” (e.g. T_1 or T_2 weighting). Based on the choice of scanner settings, that exploits the differences in the above mentioned properties between the pathology and healthy tissue and results in image contrast that reflects the variation in the chosen property. For example the T_1 and T_2 of water at 1.5 T are ~ 4000 ms and 2000 ms, respectively [101]. Cerebrospinal fluid has similar T_1 and T_2 as water because the hydrogen protons are less restricted while fat protons have restricted mobility, resulting in shorter T_1 (280-340 ms) and T_2 (60-100 ms). In comparison, the T_1 and T_2 of white matter are ~ 800 ms and 80 ms, respectively, while those for gray matter are slightly longer with values ~ 1100 ms and 90 ms, respectively. Abnormalities such as edema, tumor, inflammation, infarction and infection have increased water content (in the case of tumors, lower cell density as well) and can be detected by using T_2 weighting during the MRI acquisition as they appear bright compared to their surrounding normal tissue. In a routine clinical examination, T_2 weighted scan is often the first indicator of presence of an abnormality. A T_1 -weighted scan is often used at lower clinical magnetic field such as 1 or 1.5 T.

The first images of a tumor were generated in 1971 and paved the path for use of MR for discrimination of tumors from surrounding tissues based on differences in relaxation times [102]. MRI provides an excellent platform for non-invasive in-vivo molecular imaging of cancer, providing superior soft tissue contrast and high resolution with moderate sensitivity compared to other imaging modalities [103]. MRI can generate

images depicting anatomical, biochemical and functional information while offering a good balance between image resolution and imaging time [104]. Additionally, MRI can also help in identifying the hallmarks of cancer and lead to development, analysis and therapeutic response assessment of improved targeted therapies on tumors.

1.2.2 Paramagnetic relaxation enhancement

MRI contrast agents are biocompatible, small-molecular or nanoscale chemical entities introduced exogenously into the body to improve the contrast between the area of interest and the surrounding tissue. The properties and advantages of contrast agents were first outlined by Lauffer in 1987 [105] and since then tremendous improvements have been achieved in the field of contrast agents and several new agents are developed each year [103, 106-111]. MRI based contrast agents typically use paramagnetic molecules (e.g. chelates of gadolinium or iron oxide) to enhance the contrast of the region of their accumulation by shortening the relaxation times of the water protons around them [105]. The majority of gadolinium based contrast agents are T_1 relaxation agents and improve the contrast of the region of accumulation in a T_1 weighted image. On the other hand, iron oxide based contrast agents are predominantly T_2 weighted agents and make the accumulation region appear dark on a T_2 or T_2^* weighted image. The efficiency of a contrast agent is based on its relaxivity (r_1 or r_2), which is the change in spin-lattice relaxation rate R_1 ($= 1/T_1$) or spin-spin relaxation rate R_2 ($=1/T_2$), respectively, of water per unit concentration of contrast agent. The relaxivity is typically calculated by measuring the relaxation rate (R_1 or R_2) as a function of agent concentration and by

determining the slope of the graph (R_1 or R_2 vs. concentration). The relationship between the relaxation times, the relaxivity and the concentration of the contrast agent is given by the following equation:

$$1/T_{i(\text{measured})} = 1/T_{i(\text{water})} + r_i [\text{Agent}]; i= 1 \text{ or } 2 \quad [1.1]$$

Here $i= 1$ or 2 and refers to the T_1 and T_2 relaxation times, respectively. The important properties that influence contrast agent relaxivity are (a) spin S and the electronic relaxation times T_{ie} of the paramagnetic ion (b) the number of inner (directly coordinated to the Ln atom) and outer (hydrogen-bonded) coordination sphere water molecules (q and q' respectively), (c) the residence lifetime of the inner and outer sphere water molecule(s) (τ_m and τ_m' respectively), (d) the tumbling time of the agent in solution (τ_R , rotational correlation time), (e) the distance between water proton and metaland (f) magnetic field strength (figure 1.7).

The major contribution to the relaxation properties of the contrast agents is due to the inner sphere mechanisms. This contribution is given by:

$$r_i^{IS} = \frac{P_m q}{T_{1m} + \tau_m}; \quad i= 1 \quad [1.2]$$

Where; P_m = the mole fraction of metal ion;

q = number of bound water molecules per metal ion;

T_{1m} = relaxation time of the bound water protons; and

τ_m = residence lifetime of the bound water.

Magnetic field strength alters the relaxation rate of the contrast agent which

typically decreases with increasing field strength (at slower tumbling time) [112]. The relaxation rate at clinically relevant field depends mainly on the τ_m and τ_R properties of the agent. Reduction in the rotational correlation time of the agent, which can be achieved by increasing the molecular weight of the agent, causes an increase in the relaxivity of the agent but the increases in r_2 dominate over r_1 at higher fields, as discussed by Caravan et al. in detail [113]. If the residence time of water protons in the inner sphere is long then the corresponding exchange of relaxed water with the bulk water is limited, thus resulting in lower relaxation rate. On the other hand, very short residence time also results in lower relaxation rates due to an inefficient relaxation of the bound water. Thus there is an optimum range of residence time for which the relaxation of the agent is highest. Many of these properties can be altered in order to develop improved contrast agents for cancer imaging by rational design of the chelate ligand [107].

Targeted exogenous contrast agents can alter the T_1 (and T_2 or T_2^*) of the tissues and result in increased contrast as compared to non-targeted contrast agents. The factors influencing the relaxivity of targeted contrast agents is described in figure 1.7.

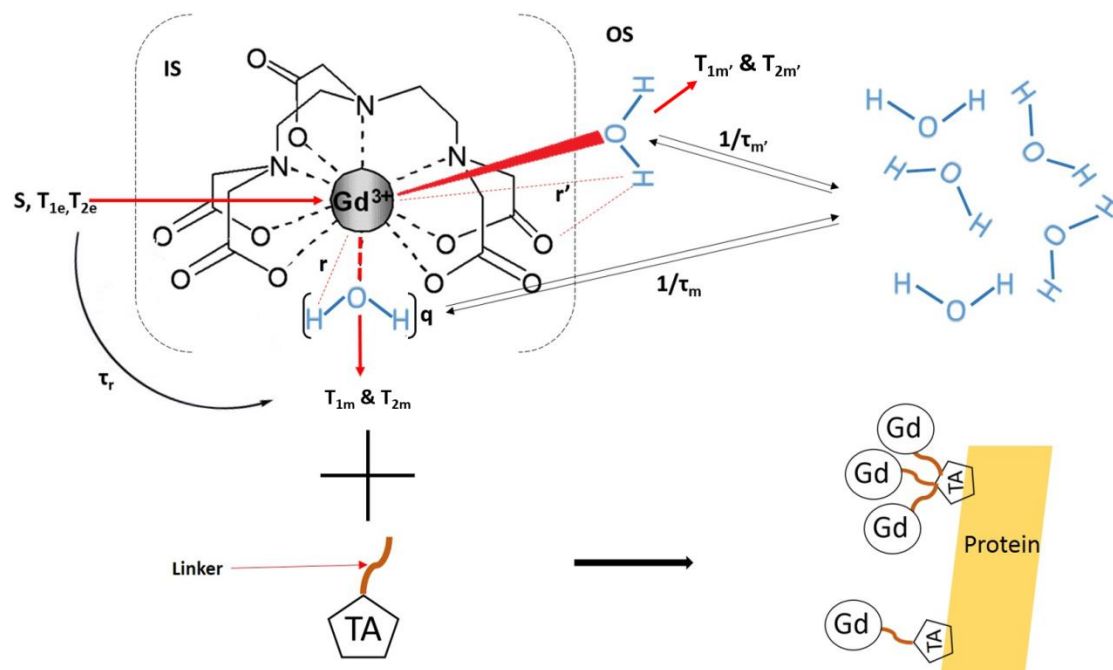


Figure 1.7: Factors influencing the solvent water relaxation and strategies for controlling rotational dynamics of multimeric, targeted contrast agents. IS: inner sphere, OS: outer sphere, T_{1e}/T_{2e} : electronic relaxation times, S : electron spin, τ_r : rotation tumbling time, τ_m : residence lifetime of water molecule, T_{1m}/T_{2m} : relaxation times of bound water, r : Ln-H distance for IS water molecules, q : number of IS water molecules, TA: targeting agent/ligand). Corresponding parameters for OS water molecules are denoted with a prime (') e.g r' : Ln-H distance for OS water molecules.

(Note Section 1.2 is based on the paper - Agarwal S and Kodibagkar VD. "Targeted Contrast Agents for 1H MRI of tumor microenvironment" *Cancer Therapeutics and Imaging: Molecular and Cellular Engineering and Nanobiomedicine* World Scientific Publishing. Eds, Rege K and Goklany S. 2016 (In press, accepted 4/9/16))

1.3 Assessment of tissue oxygenation

As discussed before in detail, the assessment of tumor oxygenation is crucial and an effective oximetry technique that can facilitate the identification of hypoxic regions within the tumor can drastically improve our understanding of the tumor behavior and

eventually result in better cancer therapeutics. In this section, I will be discussing the various established and novel oximetry techniques for qualitative and quantitative assessment of tissue oxygenation. In particular, I will discuss in detail the two novel oximetry techniques that I used for the assessment of hypoxia in my research.

1.3.1 Existing methods for measurement of pO_2

Assessment of oxygenation status can be achieved by various invasive and non-invasive techniques [114, 115]. In-vivo invasive techniques such as polarographic needle electrodes[116] and fiber optic probe[117] techniques can measure the local pO_2 and can facilitate multiple measurements throughout the tumor to get an estimate of the oxygenation distribution throughout the tumor. Ex-vivo immunohistochemical hypoxic markers (EF5 [118], HIF1 α [119], pimonidazole, CAIX) [120, 121] enable visualization of hypoxia or related molecular events throughout the tumor at higher resolution and can also be used to analyze necrosis, perfusion and expression of hypoxia regulated proteins when paired with other IHC agents. The technique provides qualitative information of hypoxia and given the dynamic nature of hypoxia might not reflect the status of the tumor by the time treatment is administered, if the ex-vivo analysis is performed with tissue samples obtained well before the start of treatment.

Non-invasive oximetry techniques include imaging agents for NIR spectroscopy [122], phosphorescence quenching [123], positron emission tomography (PET) [124], single photon emission computed tomography (SPECT) [106, 125] and MR based imaging techniques [114]. NIR spectroscopy is a non-invasive, portable technique that detects the changes in vascular oxygen saturation with high temporal resolution and can

facilitate measurements from limited depth in the tissue [126]. PET imaging agents [¹⁸F]fluoromisonidazole (¹⁸F-MISO), [¹⁸F]fluoroazomycin arabinoside (FAZA), [¹⁸F]-EF5, [¹⁸F] fluoroerythronitroimidazole (FETNIM) and [⁶⁴Cu]-diacetyl-bis(N(4)-methylthiosemicarbazone (Cu-ATSM) and [¹⁹F] Tri-Fluoromisonidazole (TF-MISO) contain the 2-nitroimidazole moiety and have been evaluated as hypoxia binding agents [127]. Nitroimidazoles were discovered to be radiosensitizers for hypoxic cells in 1974 [128] and since then significant research has been carried out on their ability to sensitize cancer cells [129-131]. The PET or SPECT agents show selective binding to the hypoxic regions and facilitate the differentiation between hypoxic and normoxic regions of a tumor. Agents such as ¹⁸F-AZA and ¹⁸F-MISO have shown the ability to determine the hypoxic fraction [132] of tumors and predict the treatment outcome in clinical studies [133, 134] respectively. However PET and SPECT based techniques lack spatial resolution, cannot provide quantitative oximetry information, are not suitable for repeated measurements.

The current MR based oximetry techniques can be sub-divided into qualitative techniques Blood Oxygen Level Dependent (BOLD) [135], Tissue Oxygen Level Dependent (TOLD) [136], oxygen-enhanced MRI [137] and quantitative techniques EPR [138], ¹⁹F NMR of perfluorocarbon emulsions, e.g. FREDOM (utilizing ¹⁹F MRI of hexafluorobenzene, a reporter for oxygen [139]) and its ¹H MR analog HMDSO based imaging called PISTOL [140, 141]. BOLD-MRI signal is dependent on the paramagnetic deoxyhemoglobin (R_2^*) and can facilitate oxygenation imaging at high spatial and temporal resolution. Previous studies have shown that BOLD signal changes are

correlated with the changes in pO_2 [135, 142]. TOLD and OE-MRI signals are also qualitative oximetry imaging methods and dependent on the paramagnetic molecular oxygen's influence on the water spin-lattice relaxation rate (R_1). OE-MRI has shown great potential for measuring the hypoxic fraction of tumors and can be used to study cyclic hypoxia (as it facilitates repeated measurements) and the effect of carbogen breathing [143].

The EPR oximetry technique is a minimally invasive technique that can provide quantitative oxygenation information via measuring the change in linewidth of an exogenously administered paramagnetic spin probe as it interacts with molecular oxygen. The technique can be used to obtain multiple measurements of the same region in tumors. Some of the EPR probes are LiPc, LiNc, Fusinite, Gloxy, India Ink, TAM etc, of which only India Ink is approved for clinical use [138, 144]. The ^{19}F NMR oximetry uses exogenous perfluorocarbon reporters such as perfluoro-15-crown-5-ether (15C5 [145]) as oxygen reporters. FREDOM (Fluorocarbon Relaxometry using Echo planar imaging for Dynamic Oxygen Mapping) is a technique that exploits the linear relationship of the relaxation rate of hexafluorobenzene (HFB) with oxygenation and has the potential to provide quantitative measurements of the tissue oxygenation sequentially and can be used to monitor the response of tumors to hyperoxic gas.

1.3.2 Quantitative MR oximetry using PISTOL

PISTOL (Proton Imaging of Siloxanes to Map Tissue Oxygenation Levels) is a quantitative ^1H MR oximetry technique that was developed by Kodibagkar et al. [140, 141]. PISTOL exploits the linear relationship of relaxation rate (R_1) of oxygen reporter probe (siloxanes) with $p\text{O}_2$.

The molecular oxygen is paramagnetic in nature and shortens the longitudinal relaxation time. The oxygen reporter molecules should possess high hydrophobicity to ensure exchange of gases between the reporter molecule and environment, and a high solubility for oxygen. Various linear siloxanes such as hexamethyldisiloxane (HMDSO, figure 1.8 A), octamethyltrisiloxane (OMTSO), decamethyltetrasiloxane (DMTSO), dodecamethylpentasiloxane (DDMPSO), polydimethylsiloxane (PDMSO, trimethylsiloxy terminated, M.W. 410) and cyclic siloxanes octamethylcyclotetrasiloxane (OMCTSO) and decamethylcyclopentasiloxane (DMCPSO) as well as perfluorocarbons have the characteristics to be utilized as oxygen reporter molecules. PISTOL has been established as a quantitative oximetry technique that allows for accurate, non-invasive and repeated measurement of tissue oxygenation using HMDSO and HMDSO based nanoemulsions at 4.7 T [140, 141, 146]. The calibration of HMDSO at 4.7 T showed the reporter's sensitivity to changes in $p\text{O}_2$ while less prone to changes in temperature (figure 1.8 B).

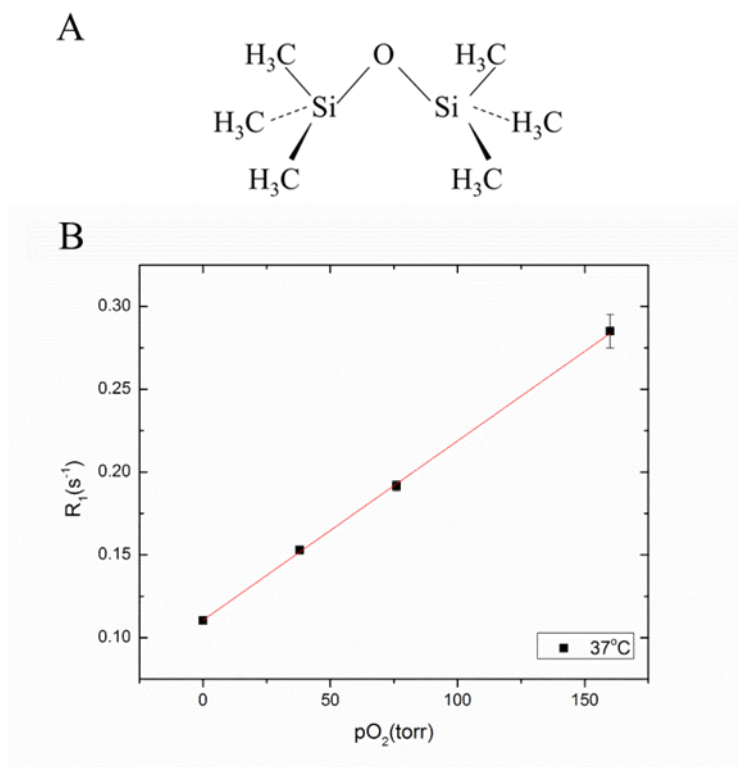


Figure 1.8: A) Chemical structure of hexamethyldisiloxane (HMDSO). B) Calibration of neat HMDSO at 0%, 5%, 10%, and 21% Oxygen Concentrations at 37°C. Fitting data to the linear model $R_1 = A' + B' \cdot pO_2$ resulted in calibration constants $A' = 0.11056 \pm 6.54 \times 10^{-4}$ and $B' = 0.00108 \pm 1.7 \times 10^{-5}$.

The pulse sequence for PISTOL consists of the following components: 1) 20 non-selective saturation pulses, followed by a tau delay for magnetization recovery, 2) 3 CHESS pulses for selective saturation of water and fat, 3) An EPI based spin-echo acquisition with frequency selective $\pi/2$ pulse (on-resonance for siloxane), followed by a 4) slice selective π pulse, and an EPI readout (figure 1.9).

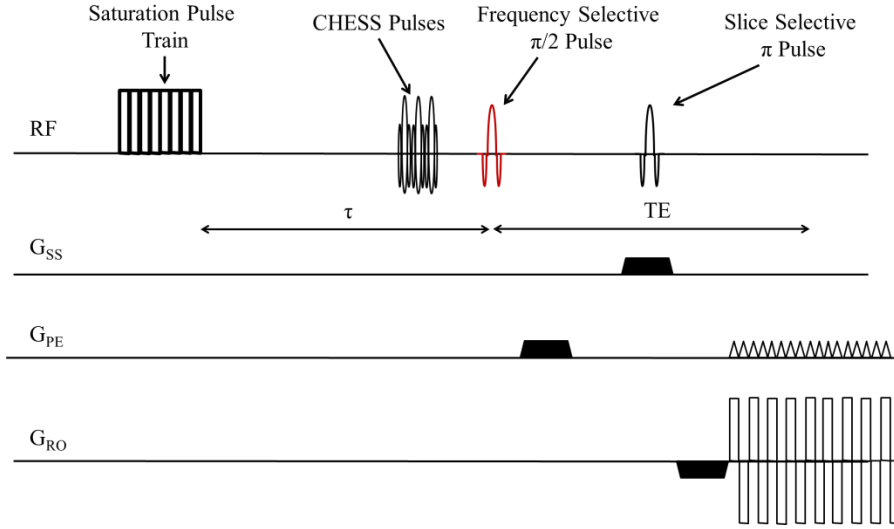


Figure 1.9: Schematic representation of the pulse sequence for PISTOL. Modified from reference [141].

The relationship between the relaxation rate of reporter molecule and pO_2 can be obtained by considering two pools of protons: a diamagnetic component that is due to the longitudinal relaxation rate of protons without oxygen in its neighborhood (R_{1d}) and a combined paramagnetic (R_{1p}) and diamagnetic component due to the proton in the vicinity of oxygen ($R_{1d} + R_{1p}$). The relaxation rate for both the pools of protons can be represented as a molar weighted average, where x is the molar fraction of the oxygen:

$$R_1 = (1 - x) * R_{1d} + x * (R_{1d} + R_{1p}) = R_{1d} + x * R_{1p} \quad [1.3]$$

According to Henry's law, the partial pressure of oxygen is directly related to the mole fraction of dissolved oxygen.

$$pO_2 = k * x \quad [1.4]$$

where k is the solubility coefficient of oxygen. Thus, equation 1.3 can be rewritten as:

$$R_1 = A' + B' * pO_2 \quad [1.5]$$

Where, A' is the diamagnetic i.e. anoxic component (R_{1d}) and B' is the paramagnetic component that is dependent on pO_2 (R_{1p}/k).

The temperature dependence of the A' and B' components can be approximated as:

$$\begin{aligned}A' &= A + C * T \\B' &= B + D * T\end{aligned}\quad [1.6]$$

Thus, a temperature dependent model for estimation of pO_2 can be obtained by substituting the values from equation 1.8 in equation 1.7.

$$R_1 = A + B * pO_2 + C * T + D * T * pO_2 \quad [1.7]$$

The above equation can be used to determine oxygenation levels as well as errors in estimation $pO_2/^\circ C$, thus providing a more accurate and reliable quantification. The following equation can be used to determine error in pO_2 determination for change in temperature by $1^\circ C$ at a particular temperature T and oxygenation level:

$$\frac{\Delta pO_2}{\Delta T} = \frac{|C + D * pO_2|}{B + D * T} \quad [1.8]$$

1.3.3 Qualitative MR oximetry using GdDO3NI

An important alternate strategy for imaging hypoxia exploits the principle of selective enzyme mediated reduction of the nitro group in 2-nitroimidazole containing compounds under hypoxic conditions. Rojas-Quijano, et al., in 2012 reported a novel hypoxia-targeted contrast agent GdDO3NI [147]. The agent was prepared by conjugation of DO3A-monamide with 2-nitroimidazole moiety, which has been used to sensitize the

hypoxic tumors to radiotherapies [148]. The hypoxia selective enzyme mediated reduction of nitro group leads to accumulation and binding of the contrast agent in the hypoxic regions [149, 150]. The agent (figure 1.10) has r_1 relaxivity of $5.21 \pm 0.04 \text{ mM}^{-1}\text{s}^{-1}$ and r_2 relaxivity of $4.74 \pm 0.03 \text{ mM}^{-1}\text{s}^{-1}$ in PBS at 4.7 T. The in-vivo hypoxia imaging of rat prostate adenocarcinoma AT1 tumors with GdDO3NI reported the utility of the agent in distinguishing between the normoxic and hypoxic regions within the tumor [151]. The agent has also shown ability in mapping the differential response of tumor hypoxia to hyperoxic gas breathing in prostate cancer sublines [152]. The agent has the potential to generate three-dimensional distribution maps of hypoxia, which can be utilized by clinicians for planning radiation and therapy.

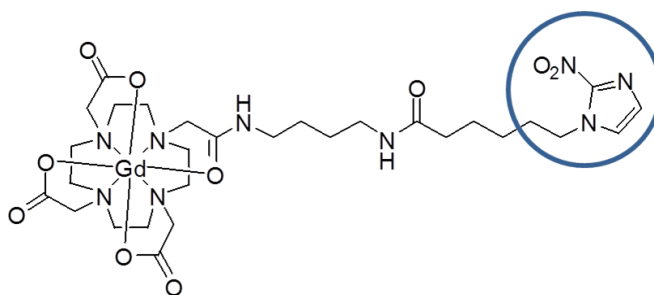


Figure 1.10: Structure of GdDO3NI. The 2-nitroimidazole moiety is highlighted in the blue circle.

CHAPTER 2

QUANTITATIVE ASSESSMENT OF CHANGES IN TUMOR OXYGENATION POST HYPOXIA ACTIVATED THERAPY USING PISTOL

2.1 Abstract

In the present study, a novel pO_2 measuring technique PISTOL (Proton Imaging of Siloxanes to map Tissue Oxygenation Levels) was used to determine the baseline oxygenation of pre-clinical xenograft tumor models of NSCLC (NCI-H1975) and epidermoid carcinoma (A431) and their response to hypoxia-activated pro-drugs (HAPs) PR509, its effector PR509E and tirapazamine (TPZ). The A431 tumor model had lower baseline oxygenation than the NCI-H1975 tumor model ($p < 0.05$). PR509 and PR509E were effective slowing the growth of NCI-H1975 ($p < 0.05$) and A431 tumors ($p < 0.01$) as compared to untreated control cohorts. PR509E and TPZ resulted in a significant increase in the oxygenation of A431 tumor centers ($p < 0.05$). TPZ was effective in slowing the tumor growth only in NCI-H1975 tumors despite the fact that A431 tumors were more hypoxic ($p < 0.05$). TPZ resulted in a significant decrease in the oxygenation of NCI-H1975 tumor centers as a result of its anti-vascular effect ($p < 0.05$). In conclusion, PISTOL was able to report the changes in tumor oxygenation in both the tumor xenografts. The results indicate that other factors such as tumor perfusion (essential for delivering TPZ) and relative expression of nitroreductases (essential for activating HAPs) may play an important role.

2.2 Introduction

Hypoxia is a characteristic feature of many tumor types, for example, prostate [153, 154], cervical [154, 155], lung [29-31, 156-158], glioblastoma [159, 160], breast [154] and head and neck cancer [49, 154, 161]. The clinical relevance of hypoxia has led to the development of several hypoxia-targeting therapeutics (discussed in detail in section 1.1.3). The failure of several promising HAPs calls for an in-depth evaluation of tumor hypoxia, its heterogeneity and its contribution towards treatment resistance and progression to improve clinical decision-making [127, 162-166].

PISTOL (Proton Imaging of Siloxanes for mapping Tissue Oxygenation Levels) ([140, 141]) is a recently developed oximetry technique, and as discussed earlier in section 1.3.2, has the potential to provide direct quantitative measurement of oxygenation non-invasively and longitudinally along with the spatial distribution and degree of hypoxia. Here I used PISTOL to quantitatively map the oxygenation of tumor xenograft models pre and post hypoxia-activated therapies (HAPs). I investigated the efficacy of a novel pro-drug PR509 and its effector PR509E and compared it with tirapazamine, a prototypical DNA damaging hypoxia-activated pro-drug, in non-small cell lung cancer (NCI-H1975) and epidermoid carcinoma (A431) xenograft models. The main purpose of this study was to 1) study the baseline oxygenation of tumor xenograft models, 2) investigate the relationship between tumor oxygenation and the efficacy of hypoxia-activated pro-drugs, 3) demonstrate the potential of PISTOL for identifying, and categorizing tumors with hypoxia and 4) to test the hypothesis that identification of tumors with hypoxia could assist in predicting the treatment outcome.

2.3 Materials & Methods

2.3.1 Animal models

Human NCI-H1975 non-small cell lung cancer and A431 epidermoid carcinoma cells (ATCC Inc.) were cultured in Roswell Park Memorial Institute (RPMI 1640) media and Dulbecco's Modified Eagle's Medium (DMEM) respectively, supplemented with 1% penicillin/streptomycin and 10% fetal bovine serum (Life Technologies, Carlsbad, CA, USA), in a 5% CO₂-containing humidified atmosphere at 37⁰C. The tumor models were selected based on the studies conducted by our collaborators by our collaborators, Dr. Adam Patterson and Dr. Jeff Smaill from The University of Auckland, to test the novel hypoxia-activated pro-drug PR509 and its toxic counterpart PR509E. Immunocompromised nu/nu mice (5-11/per cohort, Charles River Laboratories, USA) were implanted subcutaneously with 2x10⁶/40 µl cells of the respective cell line (A431 or NCI-H1975) in the right thigh. The animals were monitored and maintained as per the guidelines by The Arizona State University Institutional Animal Care and Use Committee (IACUC).

2.3.2 Hypoxia-targeted therapy

The mice bearing NCI-H1975 and A431 tumors were treated with a multi-kinase inhibitor hypoxia-activated prodrug called PR509 (60 µmole/kg), its effector PR509E (60 µmole/kg) and tirapazamine (TPZ, 60 µmole/kg, Sigma Aldrich). The respective therapies were administered immediately after the acquisition of baseline PISTOL maps. PR509 and TPZ were dissolved in 5% dextrose while PR509E was dissolved in an acidic

buffer at pH 4.5 and administered intraperitoneally. The vehicle 5% dextrose was administered as a control agent. PR509 and PR509E were generously provided by Dr. Adam Patterson from University of Auckland, New Zealand.

2.3.3 Tumor Volume Measurements

Tumor volume measurements were made using Vernier calipers every 3rd day from the day of tumor appearance until tumor excision (day 20). The formula for an ellipsoid ($\pi abc/6$), where a , b and c are three longest orthogonal dimensions (with a being the longest), was used to calculate the tumor volumes. Tumor volumes were normalized to baseline imaging (pre-treatment) volumes and then compared with post-treatment volumes to study the treatment response. Tumor doubling times were measured by fitting the mean normalized tumor volumes to a standard exponential growth curve.

2.3.4 MR imaging protocol

The following imaging protocol was followed to assess the baseline oxygenation of NCI-H1975 and A431 tumor models: Baseline (day 0) PISTOL maps were acquired once the tumors reached $\sim 300 \text{ mm}^3$ in volume. Neat HMDSO (Sigma Aldrich., 10-50 μL) was injected directly into the tumor using a Hamilton syringe with 32 Gauge needle and HMDSO droplets were deposited in a fan pattern, as shown in reference [167], along a single plane (figure 2.1). The mice were then placed on a mouse bed a mouse brain receiver coil was placed over the tumor. The mouse bed was then pushed inside the magnet and imaged using a mouse surface receiver and a volume transmitter coil. The

body temperature of mice was maintained by keeping them on a heated water-bed at 37°C. After positioning the mouse inside the scanner, a standard multi-slice multi-echo (MSME) T₂ mapping sequence was used to calculate T₂ (TR = 3 s & TE = 14-210 ms, total 15 TEs, matrix 128 x 128 and FOV 2 cm) of tumor followed by acquisition of three consecutive PISTOL T₁ maps. The mice were kept under anesthesia (air and 1.5% isoflurane; Veterinary Anesthesia Systems Inc.) during the entire course of experiment. At the end of the imaging protocol, respective therapy (TPZ, PR509, PR509E or 5% dextrose) was injected intraperitoneally. Subsequent imaging was conducted every 5th day until day 15 post baseline imaging i.e. at day 5, 10 and 15.

A custom built T₁ mapping MATLAB code was used to compute mean pO₂ from the PISTOL maps, as described previously [141]. The T₁ values obtained were used to obtain the pO₂ values via equation [1.5]. Based on the calibration of neat HMDSO at 37°C at 7 T (shown in section 1.3.2) the T₁ threshold was set at <9.05 s (i.e. pO₂ greater than 0 torr) and >3.5 s (i.e. pO₂ less than 160 torr). Mean pO₂ value from the three pO₂ maps generated from the respective three PISTOL maps was computed and compared for each tumor. In order to study the heterogeneity in tumor, we used a T₂ weighted image from the acquired MSME T₂ images to delineate the tumor and segmented it into periphery and central regions (outer and inner 50% voxels in order to equally segment the tumor into two regions, respectively, figure 2.4) and average pO₂ for both the regions as well as the whole tumor were analyzed.

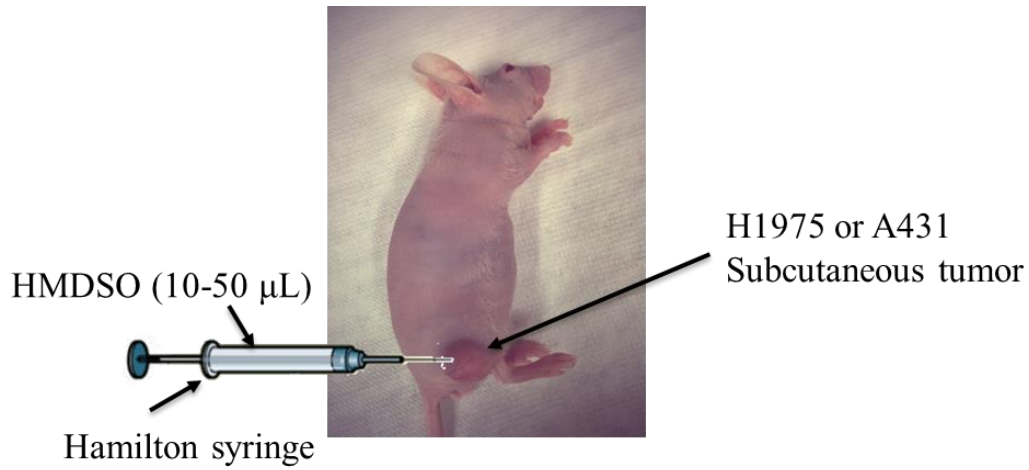


Figure 2.1: The representation of experiment set-up. Neat HMDSO droplets were deposited directly into the tumor using a Hamilton syringe in a fan pattern at axial plane.

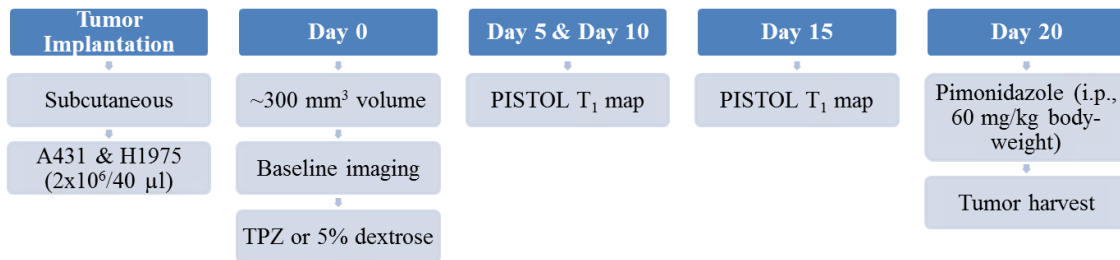


Figure 2.2: Schematic representation of the study protocol.

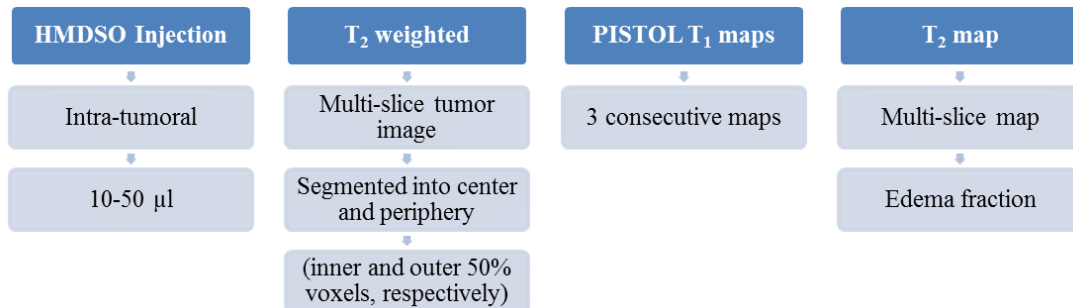


Figure 2.3: Schematic representation of the imaging protocol.

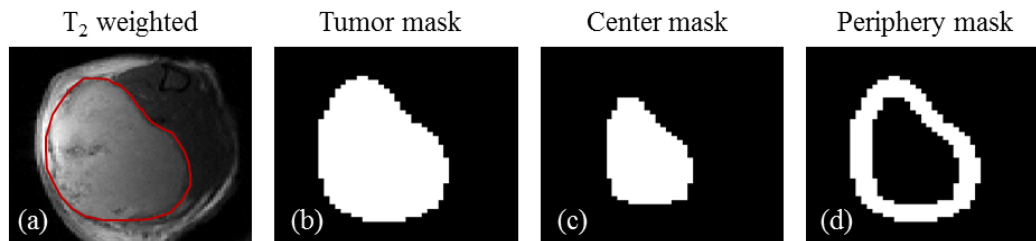


Figure 2.4: Representation of the image segmentation procedure for data analysis. (a) tumor region with the ROI applied to delineate tumor from thigh region. (b) The generated tumor mask and the corresponding center (c) and periphery (d) masks.

2.3.5 Tumor collection and immunohistochemical analysis

Three different tumors from each cohort were examined. 60 minutes prior to euthanization, the mice were injected intraperitoneally with 60 mgs/kg/body weight pimonidazole HCL (Hypoxyprobe Inc.). The mice were then placed under anesthesia and then euthanized by cervical dislocation. The tumors were surgically removed and embedded in optimum cutting temperature compound (OCT) placed in a cryomold and frozen on dry ice and stored at -80°C until further processing. For ex-vivo analysis of hypoxia, 25 μm thick tumor sections were obtained using a cryostat and placed on a microscope slide. The tumor section corresponding to the slice location of PISTOL maps were selected and stained with FITC conjugated anti-pimonidazole antibody (1:200) overnight at 4°C and counterstained with DAPI (300 nM, nucleic acid stain). The stained section were visualized under a fluorescence microscope (Leica Biosystems) using the GFP channel (EX: 450-490 nm, EM: 500-550 nm) for pimonidazole and the blue channel (EX: 355-425 nm, EM: 470 nm) for DAPI at 5X magnification. Hypoxic fractions were calculated using a custom made MATLAB code. Briefly, the image was split into blue (DAPI) and green (Pimo) channels. The blue channel image was used to delineate the

tumor and applied to the green channel image. A region of interest was then drawn within the green channel image corresponding to the tumor around a region with minimum intensity and its mean and standard deviation was calculated. Regions with value 2 standard deviations above the mean of were considered as hypoxic and used to calculate the hypoxic fraction. The hypoxic fractions of all the cohorts were then compared for analysis.

2.3.6 Edema fraction analysis

We investigated the occurrence of edema in the tumors pre and post treatment and analyzed the correlation with the treatment. The inefficient vasculature and lymphatic system in the tumors leads to formation of regions with higher fluid accumulation or edema. Edema can also result from the necrosis and treatment induced cell-death. Edema has higher T_2 as compared to the tumors [168]. The edema fraction was calculated by applying a bi-exponential fit model, a modification of the model described here [169, 170], to the acquired T_2 maps using a custom made MATLAB code. Pixel by pixel computation of short (0-200 ms) and long T_2 (>200 ms) components was conducted to calculate the edema fraction. Mean edema fraction (fraction of pixels with long T_2 component) was then calculated for the entire volume of the tumor.

2.3.7 Data analysis

Statistical analyses of all the tumor volume, oxygenation and edema fraction data were conducted via a Student T-Test using the GraphPad PRISM 7.0 Software

(GraphPad Inc., La Jolla CA). For statistical analysis alpha of <0.05 was considered as significant. Un-paired T-Tests were conducted between the normalized tumor volumes for A431 and NCI-H1975 tumor bearing cohorts treated with PR509, PR509E, TPZ and untreated control to evaluate the treatment response. Un-paired T-Tests were also conducted to analyze the difference between the mean baseline oxygenation and mean edema fraction of the two tumor models. Paired t-tests were conducted to determine the baseline intra-tumoral variation in oxygenation of central and peripheral region. Paired T-Tests were also conducted to determine the significance of changes between the oxygenation of tumors as well as edema fraction post treatment i.e. at day 5-15 from day 0. Paired t-tests were also conducted between the oxygenation of central and peripheral region for each cohort. Un-paired T-Tests were conducted between the A431 and NCI-H1975 tumor bearing mice treated with the same therapy. Tumor doubling times were calculated using the Origin 8.1 software (OriginLab Corporation).

2.4 Results

2.4.1 Baseline tumor oxygenation and edema fraction

A total of 31 A431 and 32 NCI-H1975 tumor bearing animals were studied. In order to understand the baseline characteristics of A431 and NCI-H1975 tumors, the mean pO_2 values derived from the PISTOL maps for each tumor type were compared using an unpaired t-test. The mean baseline (day 0) oxygenation of A431 tumors (32 ± 12.5 torr) was found to be significantly lower than the NCI-H1975 tumors (47 ± 14 torr) ($p < 0.0001$) (figure 2.5 A). Further comparison between the mean pO_2 of tumor center and

periphery showed that A431 tumor centers had significantly lower oxygenation (27 ± 12 torr) as compared to NCI-H1975 tumor centers (50 ± 17 torr , $p < 0.0001$). The oxygenation of A431 tumor periphery (39 ± 15 torr) was also significantly lower than the NCI-H1975 tumors' periphery (47 ± 15 torr, $p < 0.05$).

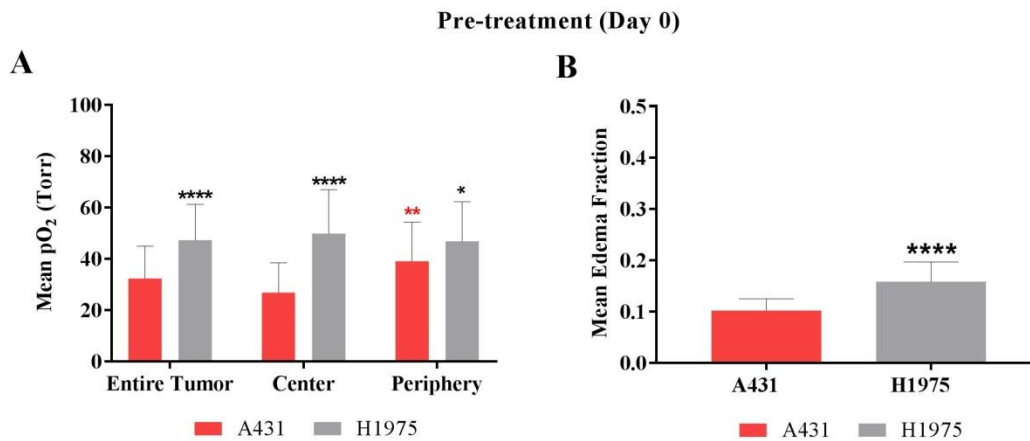


Figure 2.5: The baseline mean tumor oxygenation (A) and baseline edema fraction (B) of A431 (n = 31) and NCI-H1975 (n = 32) tumors. A431 tumors were significantly more hypoxic and had smaller edema fraction than NCI-H1975 tumors. Note: Black * represent statistical difference between A431 and NCI-H1975 tumors. Red * represent difference between the center and periphery of the respective tumor type (**** represents $p < 0.0001$ and ** represents $p < 0.01$).

In order to determine the intra-tumoral variations we compared the mean oxygenation of the central and peripheral regions (figure 2.5 A). Paired t-tests showed that the A431 tumor centers had significantly lower oxygenation as compared to the periphery ($p < 0.005$), while the center of NCI-H1975 tumors had slightly higher oxygenation than the tumor periphery but the difference was not statistically significant. Furthermore, we computed and compared the baseline mean edema fraction between the tumor models and found that A431 tumors (0.1 ± 0.02) had significantly lower edema fraction as compared to the NCI-H1975 tumors (0.16 ± 0.04 , $p < 0.0001$, figure 2.5 B).

2.4.2 Treatment response

The efficacy of the HAP treatment was determined by analyzing the normalized mean tumor volume differences between the treated and untreated control cohorts. The mean normalized tumor volumes of PR509 and PR509E treated A431 tumors were significantly lower than the untreated control tumors ($p < 0.0001$) at day 15 while TPZ treated A431 tumors were comparable to the control tumors (figure 2.6 A). The mean normalized tumor volumes of PR509 and PR509E treated NCI-H1975 tumors were significantly lower than the untreated control tumors ($p < 0.001$ and $p < 0.05$) at day 15 (figure 2.6 B). TPZ treated NCI-H1975 tumors were also significantly smaller as compared to the untreated control tumors at day 15 ($p < 0.05$, figure 2.6 B). A significant difference was also observed between control A431 and NCI-H1975 normalized mean tumor volumes at day 15 with A431 control tumors being smaller than the NCI-H1975 control tumors ($p < 0.05$). PR509 was more effective than PR509E in NCI-H1975 xenografts ($p < 0.06$).

We also investigated the tumor volume doubling times in order to evaluate the therapeutic effect and tumor prognosis. The mean volume doubling time for untreated A431 tumors was 7 ± 0.4 days while for NCI-H1975 tumors was 5 ± 0.4 days. PR509 and PR509E treated A431 tumors showed regression while those treated with TPZ had a doubling time of 7.5 ± 0.5 days. PR509, PR509E and TPZ treated NCI-H1975 tumors had a doubling time of 9 ± 0.8 , 7 ± 0.2 and 7 ± 0.2 days respectively (Table 2.1).

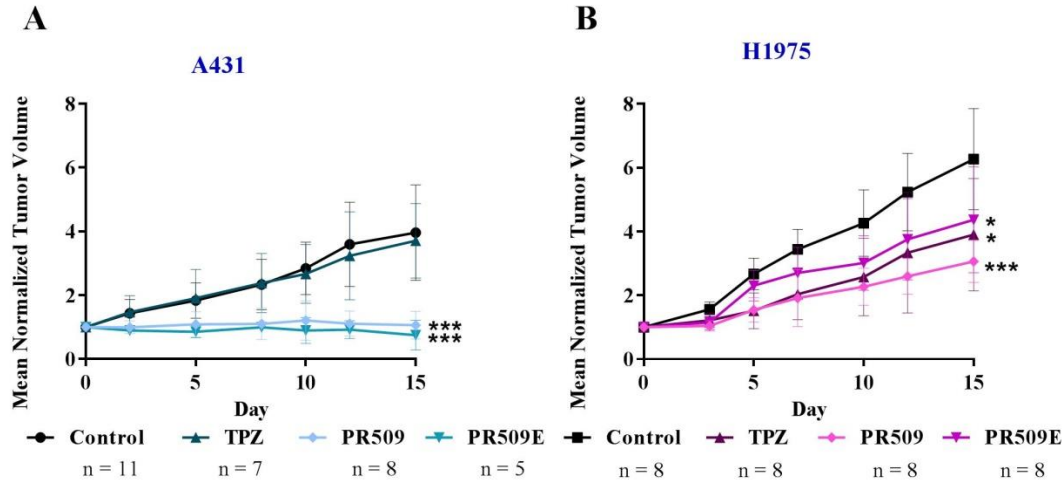


Figure 2.6: The mean normalized tumor volumes of A431 and NCI-H1975 tumor treated with TPZ, PR509, PR509E and untreated control and their statistical differences. The PR509 and its effector PR509E treated A431 tumors had significantly lower mean normalized tumor volumes than the TPZ and untreated control tumors. While all the three treatments were successful in slowing down the tumor growth in NCI-H1975 cohorts and had significantly lower mean normalized tumor volumes than the untreated control. Note: The error bars represent the standard deviation. The statistical difference were calculated between the treated and untreated control normalized tumor volumes for both the tumor types (***) represents $p < 0.001$ and * represents $p < 0.05$).

Table 2.1: Tumor doubling times of A431 and NCI-H1975 treated tumors.

	Tumor doubling time (Days)			
	Untreated Control	TPZ	PR509	PR509E
A431	7 ± 0.4	7.5 ± 0.5	N/A	N/A
NCI-H1975	5 ± 0.4	7 ± 0.2	9 ± 0.8	7 ± 0.2

2.4.3 In-vivo Imaging

We evaluated the therapy induced changes in the tumors' oxygenation and compared them to baseline levels. We investigated the changes in the overall tumor oxygenation as well as in tumor center and periphery.

2.4.3.1 In-vivo Imaging: Treatment response of epidermoid carcinoma A431

Untreated Control: The untreated control A431 tumor centers had a significant increase in the oxygenation at day 15 (34 ± 10 torr) from the baseline levels (24 ± 12.5

torr, $p < 0.05$). While, no significant change was observed in the periphery. The tumor did not show any significant intra-tumoral heterogeneity (center vs. periphery) in the oxygenation. The behavior of the untreated control cohort is shown in figure 2.7 (A).

TPZ: The oxygenation of TPZ treated tumors increased post treatment and the difference was significant between day 15 (54 ± 11 torr, $p < 0.05$) and baseline (30 ± 14 torr) for the tumor centers. The behavior of the TPZ treated cohort is shown in figure 2.7 (B). On the other hand, the changes in oxygenation of tumor periphery were not significant. We also observed that the tumor center (59 ± 11 torr) had significantly higher oxygenation than the tumor periphery (47 ± 13 torr, $p < 0.01$) post-treatment at day 15.

PR509: PR509 treated tumors initially showed a decrease in the mean oxygenation at day 10 (28 ± 7 torr) but a not significant increase was observed at day 15 (38 ± 8 torr, $p < 0.08$, fig 3C). The mean oxygenation at day 5 (28 ± 10 torr, $p < 0.08$) of the tumor periphery was lower as compared to the baseline (41 ± 17 torr). The post-treatment (day 5) oxygenation of tumor centers was significantly lower as compared to the periphery. The behavior of the PR509 treated cohort is shown in figure 2.8 (A).

PR509E: PR509E treatment of the A431 cohort resulted in a significant increase in the oxygenation of tumor centers at day 5 (41 ± 7 torr) and day 15 (52 ± 18 torr) from baseline (23 ± 8 torr, $p < 0.01$). The peripheral regions' oxygenation did not show any significant change for post-treatment. There were no significant intra-tumoral differences observed. The behavior of the PR509E treated cohort is shown in figure 2.8 (B).

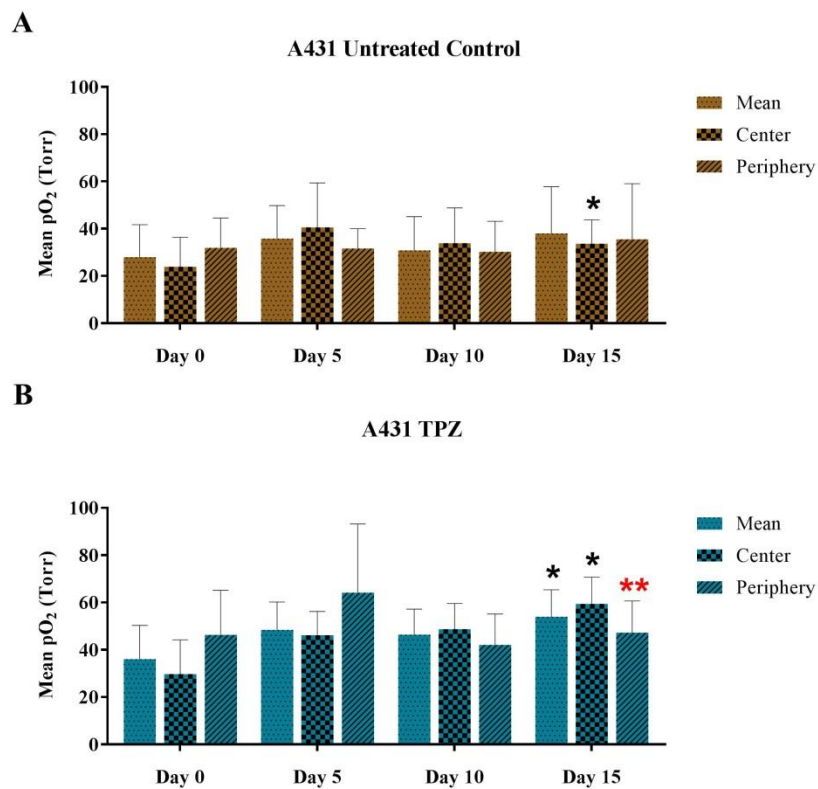


Figure 2.7: The oxygenation changes of untreated control (n = 11) and TPZ treated (n = 7) A431 cohorts and their statistical comparison. Note: The error bars represent the standard deviation. The black colored * represents the significant difference from baseline and the red colored * represents the significant difference between the center and periphery (* represents $p < 0.05$ and ** represents $p < 0.01$).

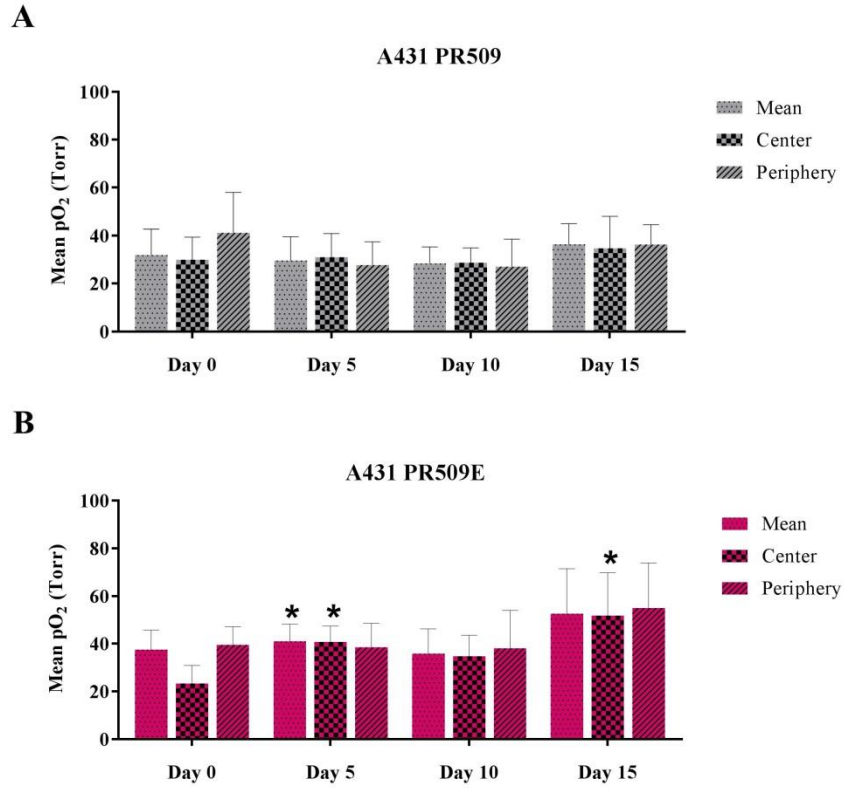


Figure 2.8: The oxygenation changes of PR509 (n = 8) and PR509E (n = 5) treated A431 cohorts and their statistical comparison. Note: The error bars represent the standard deviation. The black colored * represents the significant difference from baseline (* represents $p < 0.05$).

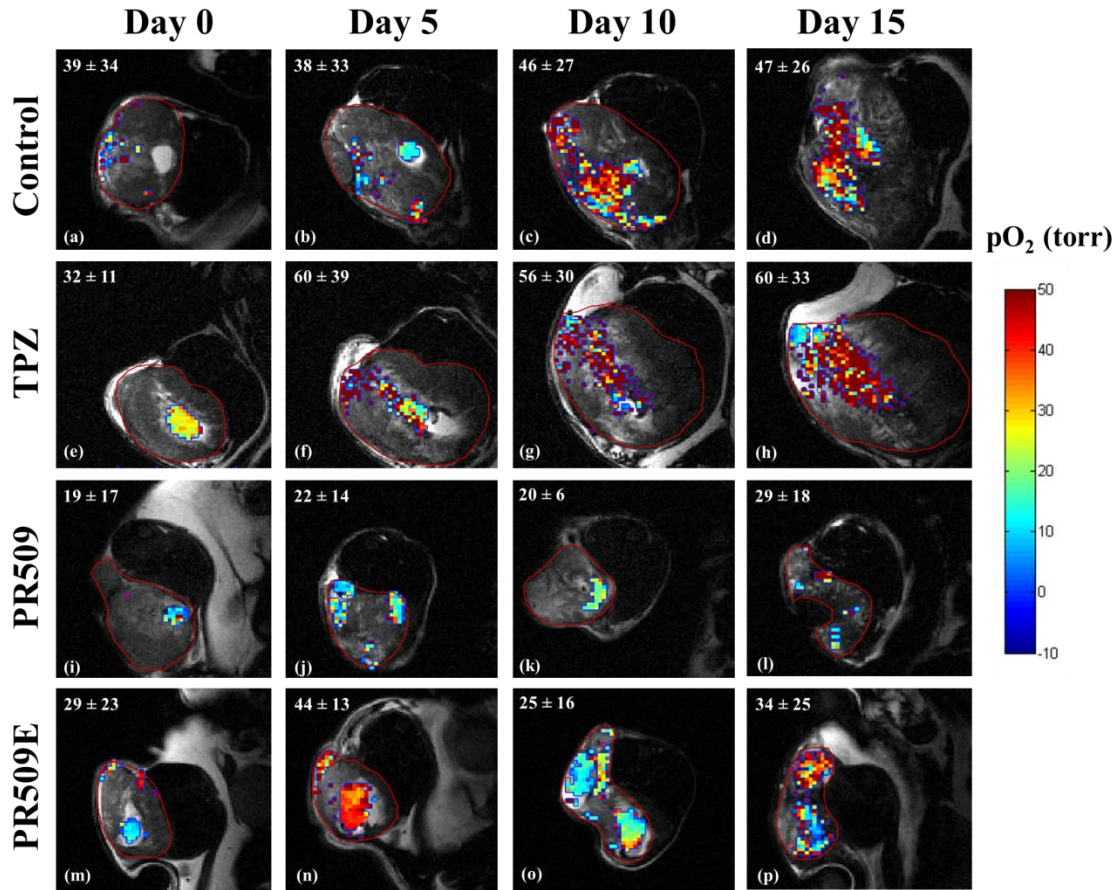


Figure 2.9: Overlay of the reference T₂-weighted tumor image and the respective pO₂ map from day 0 – 15 for all the four A431 cohorts. The region of interest (shown as red boundary) represents the segmentation that was conducted to delineate the tumor from surrounding tissue and also to segment the tumor into center and periphery.

2.4.3.2 In-vivo imaging: Treatment response of non-small cell lung cancer NCI-H1975

Untreated control: Untreated control NCI-H1975 tumor centers as well as periphery had a significant decrease in the mean oxygenation of the tumor at day 5 from baseline ($p < 0.01$). The tumor periphery had significantly lower oxygenation also at day 10 (33.5 ± 9 torr) as compared to baseline (55 ± 19 torr). The behavior of the untreated control cohort is shown in figure 2.10 (A).

TPZ: The TPZ treatment of NCI-H1975 tumors resulted in a decrease in the oxygenation at day 5 (40 ± 11 torr) and day 10 (40 ± 10 torr) of tumor centers from the baseline (55 ± 15 torr, $p < 0.05$). The behavior of the TPZ treated cohort is shown in figure 2.10 (B).

PR509 & PR509E: The statistical analysis showed that PR509 treatment resulted in a significant decrease in the oxygenation of the tumor periphery at day 5 (24 ± 5 torr, $p < 0.05$) from baseline (37 ± 11.5 torr, $p < 0.05$). Post day 5, the oxygenation increased for both tumor center as well as periphery till day 15 and the increase was significant for tumor periphery at day 15. In PR509E treated tumors, the oxygenation of tumor centers decreased significantly at day 15 (33 ± 18 torr) from baseline (47 ± 20 torr). The behavior of the PR509 and PR509E treated cohorts are shown in figure 2.11 (C & D).

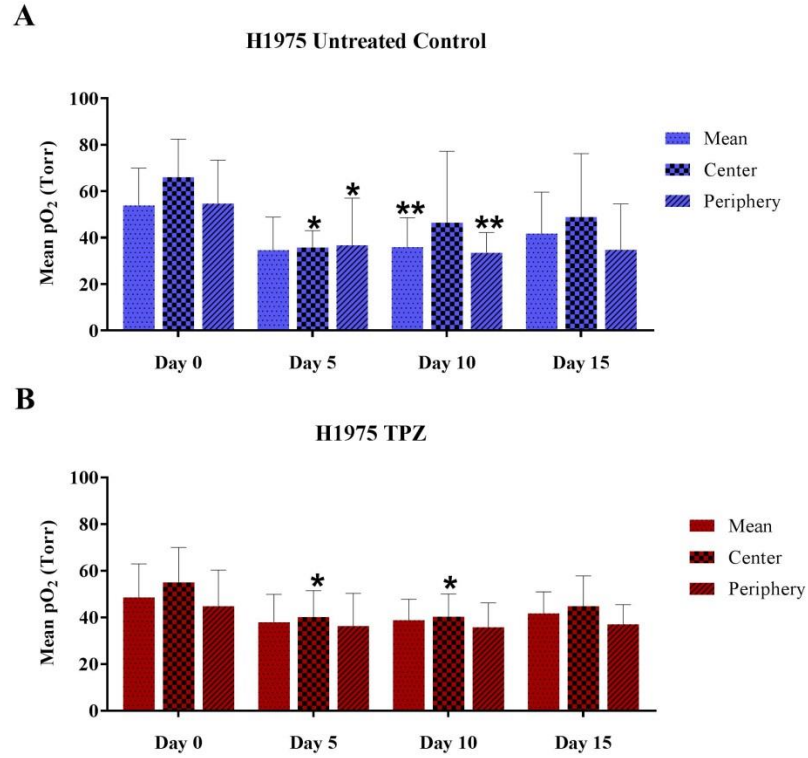


Figure 2.10: The oxygenation changes of untreated control (n = 8) and TPZ treated (n = 8) NCI-H1975 cohorts and their statistical comparison. Note: The error bars represent the standard deviation. The black colored * represents the significant difference from baseline. (* represents $p < 0.05$ and ** represents $p < 0.01$)

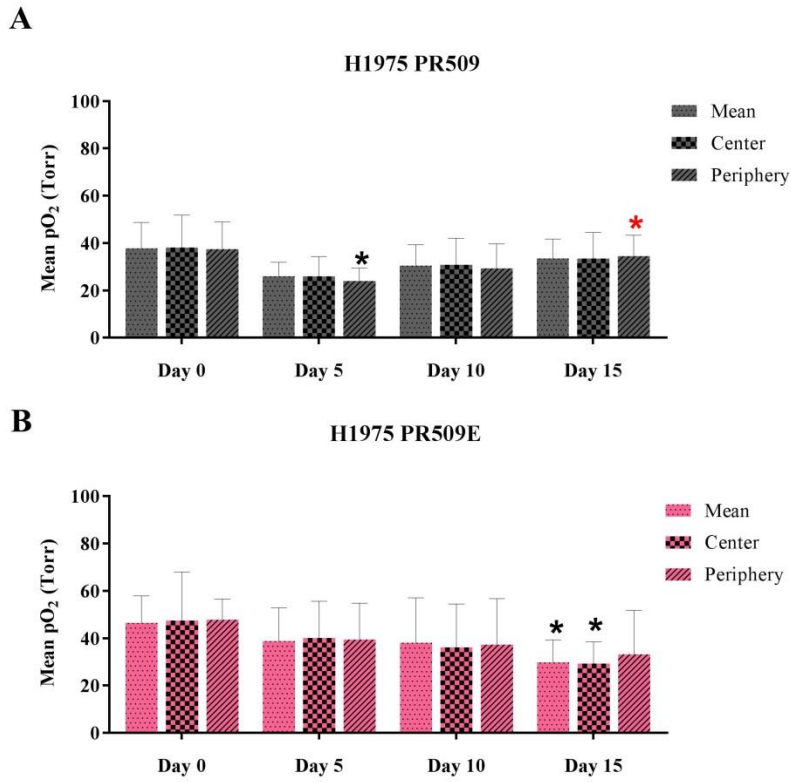


Figure 2.11: The oxygenation changes of PR509 (n = 8) and PR509E (n = 8) treated NCI-H1975 cohorts and their statistical comparison. Note: The error bars represent the standard deviation. The black colored * represents the significant difference from baseline and the red colored * represents the significant difference from day 5. (* represents $p < 0.05$)

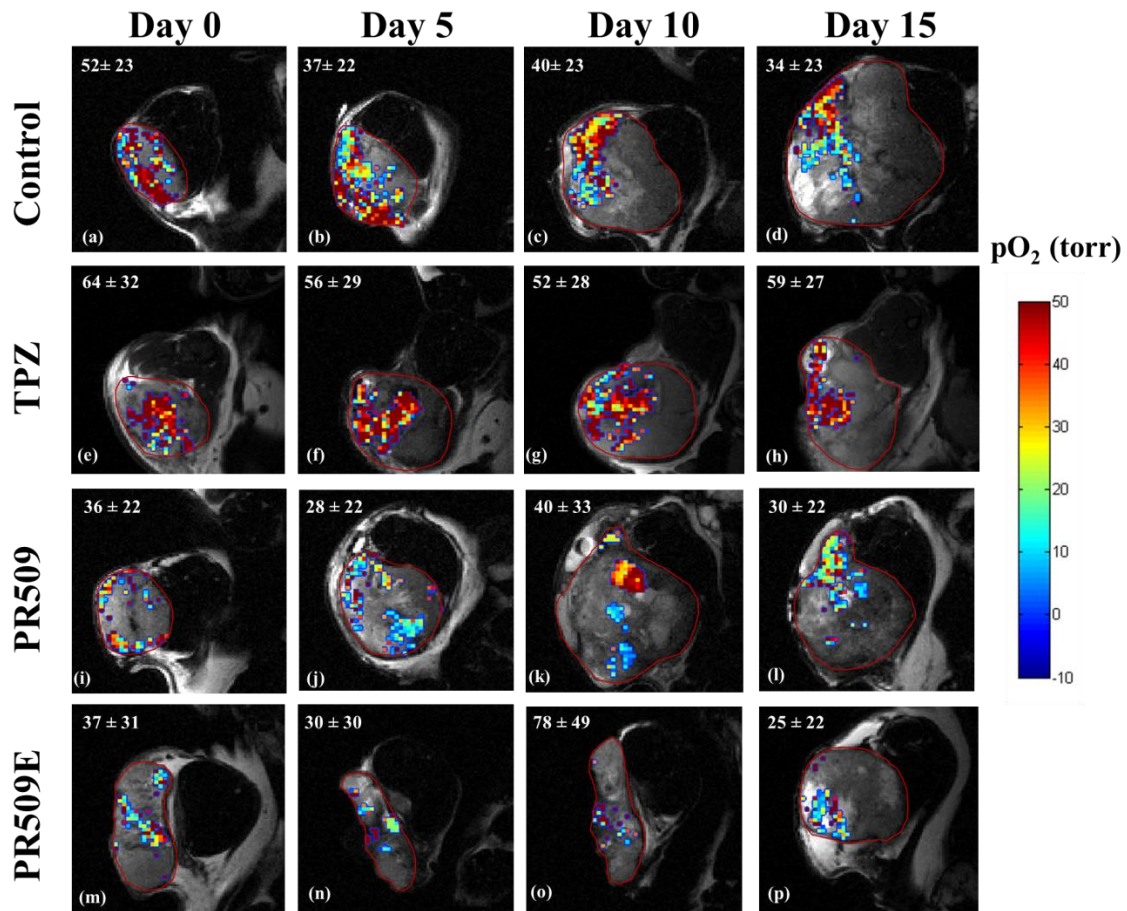


Figure 2.12: Overlay of the reference T₂-weighted tumor image and the respective pO₂ map from day 0 – 15 for all the four NCI-H1975 cohorts. The region of interest (shown as red boundary) represents the segmentation that was conducted to delineate the tumor from surrounding tissue and also to segment the tumor into center and periphery.

Table 2.2: Mean oxygenation of A431 and NCI-H1975 xenograft tumor models from day 0 -15.

Tumor Model	Treatment		Mean pO ₂ (torr)			
			Day 0	Day 5	Day 10	Day 15
A431	Untreated Control (n = 8)	Mean	28 ± 14	36 ± 14	31 ± 14	38 ± 20
		Center	24 ± 11.5	41 ± 19	34 ± 15	34 ± 10
		Periphery	32 ± 13	32 ± 13	30 ± 13	36 ± 23
	TPZ (n = 8)	Mean	36 ± 14	48 ± 12	46 ± 11	54 ± 11
		Center	30 ± 14	46 ± 10	49 ± 11	59 ± 11
		Periphery	46 ± 19	64 ± 29	42 ± 13	47 ± 13
	PR509 (n = 8)	Mean	32 ± 11	30 ± 10	28 ± 7	36 ± 8
		Center	30 ± 9	31 ± 10	29 ± 6	35 ± 13
		Periphery	41 ± 17	28 ± 10	27 ± 11	36 ± 8
	PR509E (n = 8)	Mean	37.5 ± 8	41 ± 7	36 ± 10	53 ± 19
		Center	23 ± 8	41 ± 7	35 ± 9	52 ± 18
		Periphery	39.5 ± 8	38.5 ± 10	38 ± 16	55 ± 19
NCI-H1975	Untreated Control (n = 11)	Mean	54 ± 16	35 ± 14	36 ± 13	42 ± 18
		Center	66 ± 14	36 ± 7	46 ± 31	49 ± 27
		Periphery	55 ± 19	37 ± 20	33.5 ± 9	35 ± 20
	TPZ (n = 7)	Mean	48.5 ± 14	38 ± 12	39 ± 9	42 ± 9
		Center	55 ± 15	40 ± 11	40 ± 10	45 ± 13
		Periphery	45 ± 15	36 ± 14	36 ± 10	37 ± 8
	PR509 (n = 8)	Mean	38 ± 11	26 ± 6	30 ± 9	33.5 ± 8
		Center	38 ± 14	26 ± 8	31 ± 11	33 ± 11
		Periphery	37 ± 11.5	24 ± 5	29 ± 10	35 ± 9
	PR509E (n = 5)	Mean	46.5 ± 11	39 ± 14	38 ± 19	30 ± 10
		Center	47 ± 20	40 ± 16	36 ± 18	29 ± 9
		Periphery	48 ± 9	39 ± 15	37 ± 19	33 ± 19

2.4.4 Edema fraction

Edema fractions were calculated from the analysis of T₂ maps. We investigated the changes in edema fraction as a response to therapy and also compared the intra-treatment differences in the mean edema fraction for each tumor model. Untreated control A431 tumors had a significant decrease in the edema fraction at day 10 (0.09 ±

0.02, $p < 0.05$) and day 15 (0.08 ± 0.01 , $p < 0.05$) from the baseline (0.11 ± 0.03) (figure 2.13). There were no significant changes observed in all the three treated A431 cohorts. Even a comparison among the edema fraction of treatments at same time point did not show any significant difference. Next, we compared the edema fractions of NCI-H1975 tumors. The edema fraction of TPZ treated cohort was significantly lower than the untreated control cohort at all the time point post-treatment (figure 2.14). The edema fraction was even significantly lower than PR509E at day 10. The treatment with PR509 resulted in a significantly lower edema fraction than untreated control at day 15. We also observed that the mean edema fraction of PR509 treated tumors were lower than the PR509E treated ($p < 0.06$).

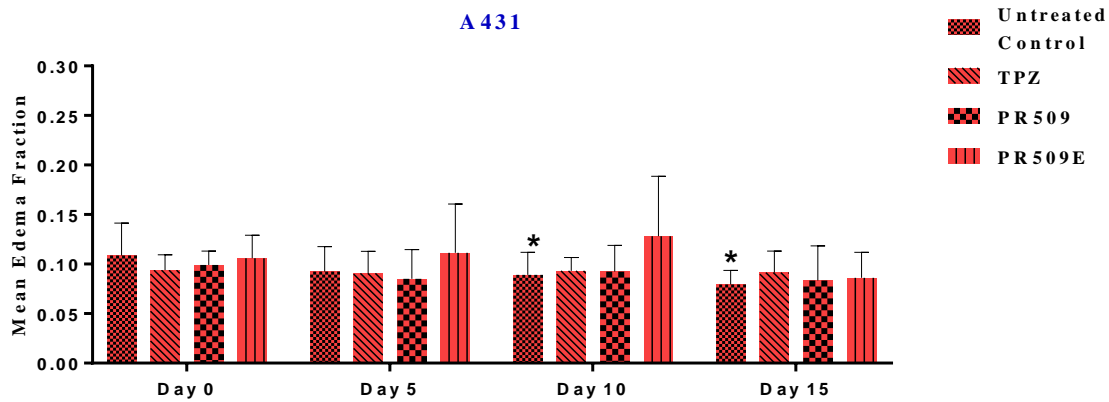


Figure 2.13: Treatment induced changes in edema fraction of A431 tumors. Note: The error bars represent the standard deviation. The black colored * represents the significant difference from baseline (* represents $p < 0.05$).

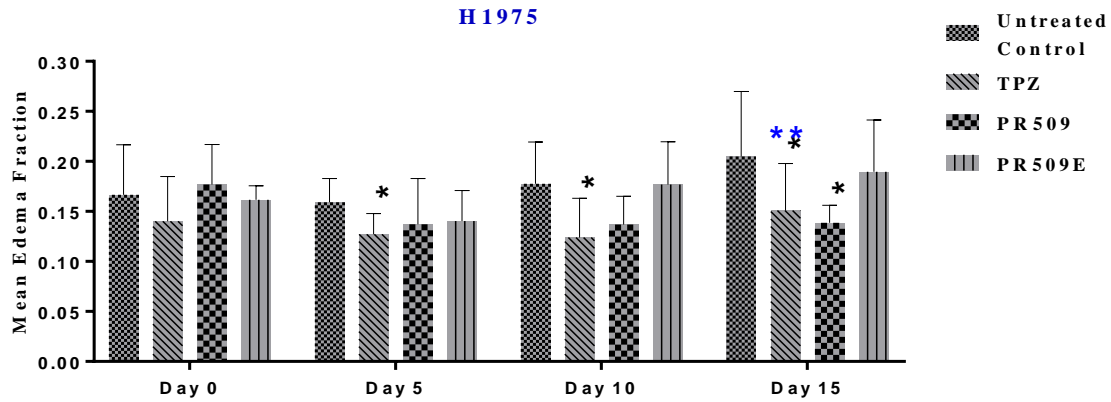


Figure 2.14: Treatment induced changes in edema fraction of NCI-H1975 tumors. Note: The error bars represent the standard deviation. The black colored * represents the significant difference from untreated control cohort and the blue colored * represents the significant difference from at day 15 from day 10 of TPZ treated cohort (* represents $p < 0.05$ and ** represents $p < 0.01$).

As stated above, the baseline edema fractions were significantly different for A431 and NCI-H1975 tumors. Next, we wanted to see the differences among the two tumor models treated with respective therapies. The statistical analysis of mean edema fraction changes between the respective A431 and NCI-H1975 cohorts showed that NCI-H1975 tumors consistently had higher edema fraction post-treatment than their A431 counterparts (figure 2.15). Table 2.3 lists all the mean edema fractions for all the 8 cohorts.

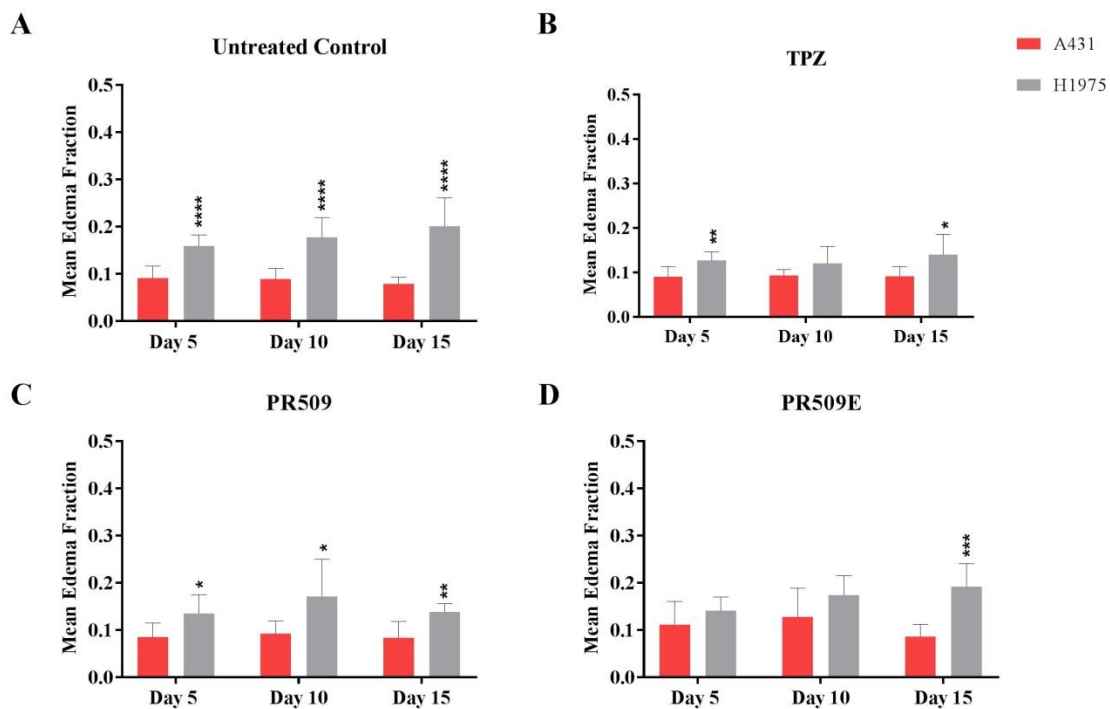


Figure 2.15: Treatment induced changes in edema fraction A431 vs. NCI-H1975. Note: The error bars represent the standard deviation (* p<0.05, ** p<0.01, *** p<0.005 and **** p<0.0001).

Table 2.3: Mean Edema fraction of A431 and NCI-H1975 xenograft tumor models.

		Mean Edema Fraction			
Tumor Model	Treatment	Day 0	Day 5	Day 10	Day 15
A431	Untreated control	0.11 ± 0.03	0.09 ± 0.03	0.09 ± 0.02	0.08 ± 0.01
	TPZ	0.09 ± 0.02	0.09 ± 0.02	0.09 ± 0.01	0.09 ± 0.02
	PR509	0.10 ± 0.01	0.08 ± 0.03	0.09 ± 0.03	0.08 ± 0.03
	PR509E	0.10 ± 0.02	0.11 ± 0.05	0.13 ± 0.06	0.09 ± 0.03
NCI-H1975	Untreated control	0.17 ± 0.05	0.16 ± 0.02	0.18 ± 0.04	0.22 ± 0.05
	TPZ	0.14 ± 0.05	0.13 ± 0.02	0.12 ± 0.04	0.15 ± 0.05
	PR509	0.18 ± 0.04	0.14 ± 0.05	0.14 ± 0.03	0.14 ± 0.02
	PR509E	0.16 ± 0.01	0.14 ± 0.03	0.18 ± 0.04	0.19 ± 0.05

2.4.5 A431 vs. NCI-H1975 tumor oxygenation

The heterogeneity of tumor behavior as a response to therapy is not well documented, thus we wanted to investigate the differences in behavior of our tumor models with respect to treatments. The comparison between the untreated control A431 and NCI-H1975 tumors showed that the oxygenation between the cohorts was not significantly different (figure 2.16 A). The periphery of A431 tumors treated with TPZ had significantly higher mean oxygenation as compared to the NCI-H1975 tumors at day 5 and day 15 (figure 2.16 B). The tumor centers of A431 cohort treated with PR509 had significantly lower oxygenation as compared to the NCI-H1975 cohort at day 10 (figure 2.16 C). While periphery of A431 tumors treated with PR509E were significantly higher than the NCI-H1975 tumors at day 15 (figure 2.16 D).

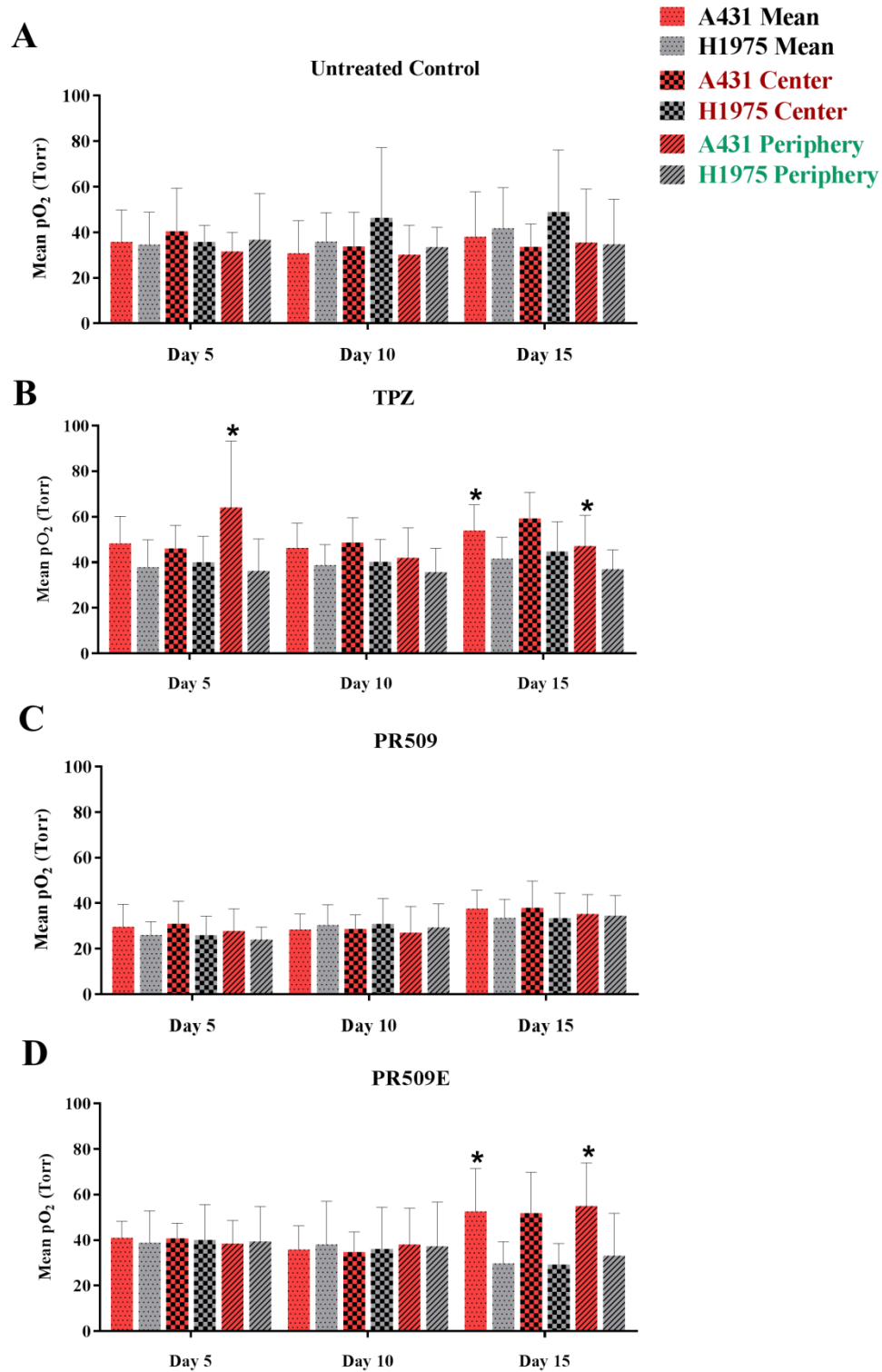


Figure 2.16: A431 vs. NCI-H1975 oxygenation (* $p < 0.05$). Note: The error bars represent the standard deviation.

In order to confirm the existence of hypoxia within the tumors post day 15 post-therapy, we analyzed the distribution of hypoxia in tumors by immunohistochemical analysis of pimonidazole adducts based measurement of hypoxic fractions (gold standard for hypoxia). Three tumors from each cohort were selected for the ex-vivo analysis of hypoxia. The center of TPZ treated NCI-H1975 tumors (0.27 ± 0.10) had significantly higher hypoxic fraction than the PR509E treated tumors (0.08 ± 0.04 , figure 2.17 C). PR509 treated NCI-H1975 tumor centers (0.10 ± 0.04) had lower hypoxic fraction than the tumor periphery (0.22 ± 0.04 , figure 2.17 C). No significant difference was observed in the hypoxic fractions of rest of the cohorts. Table 4 contains all the mean hypoxic fractions from each cohort.

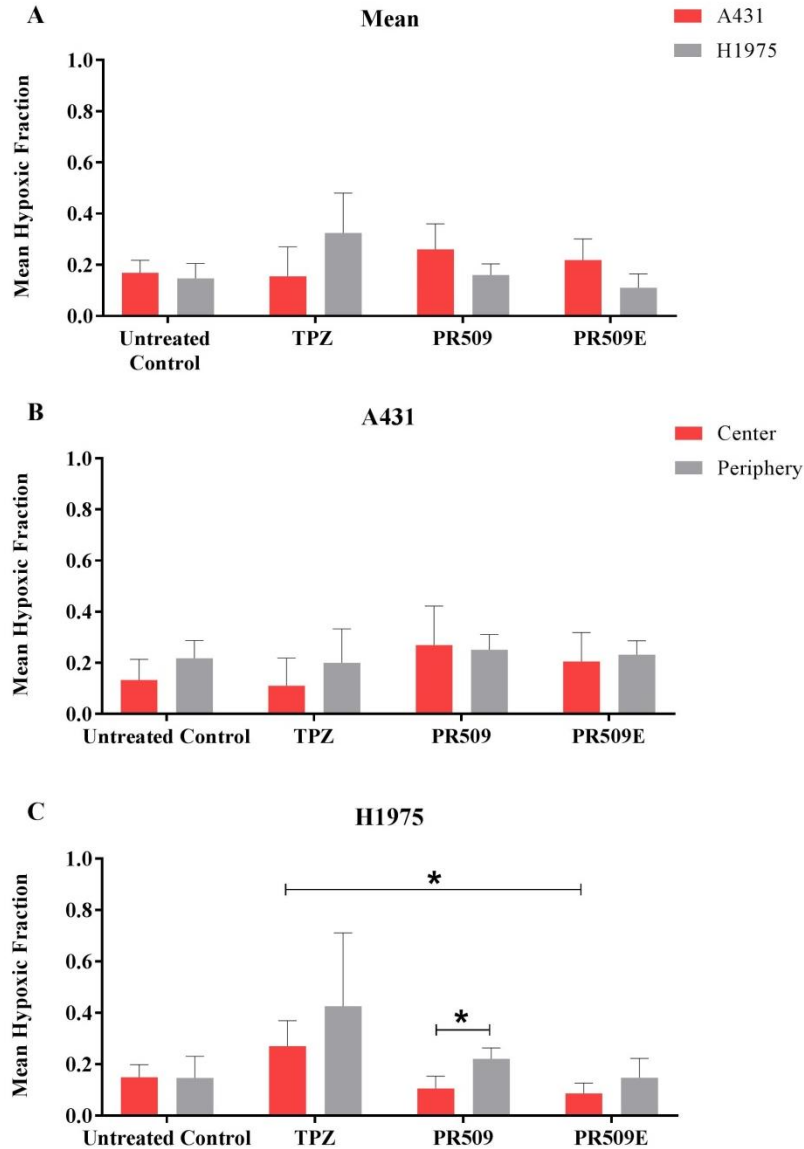


Figure 2.17: (A) The mean hypoxia fractions of A431 and NCI-H1975 cohorts, measured at day 15 post-treatment, by pimonidazole staining (n = 3). TPZ treatment of NCI-H1975 tumors resulted in a higher extent of hypoxia as compared to other three NCI-H1975 cohorts. The mean hypoxia fraction of (B) A431 and (C) NCI-H1975 tumors segmented into center and periphery. No significant changes were observed in the A431 tumors. In NCI-H1975 tumors, the TPZ treated tumor centers had significantly higher hypoxic fraction than the PR509E treated tumors and PR509 treated tumor centers had lower hypoxic fraction than the tumor periphery (* represents $p < 0.05$).

Table 2.4: Mean hypoxic fraction of A431 and NCI-H1975 treated tumors computed from immunohistochemistry.

	Mean Hypoxic Fraction			
	Untreated Control	TPZ	PR509	PR509E
A431	0.21 ± 0.02	0.24 ± 0.08	0.3 ± 0.1	0.19 ± 0.08
NCI-H1975	0.19 ± 0.03	0.4 ± 0.1	0.21 ± 0.06	0.18 ± 0.07

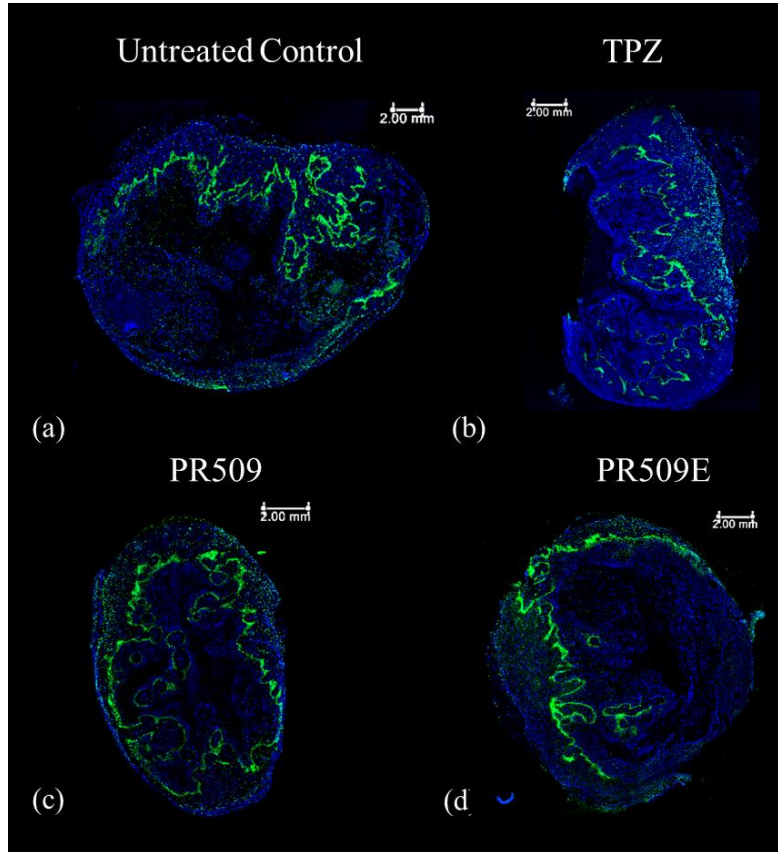


Figure 2.18: Pimonidazole stained NCI-H1975 tumor sections treated with (a) untreated (b) TPZ (c) PR509 and (d) PR509E. The green color represents regions with Pimonidazole and the blue represents DAPI nuclear stain.

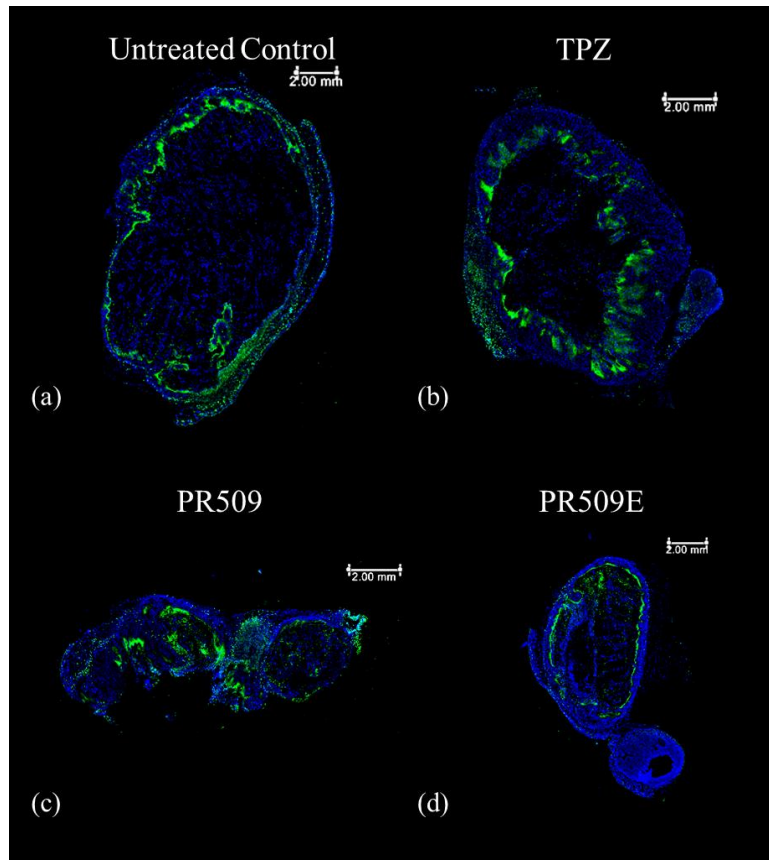


Figure 2.19: Pimonidazole stained A431 tumor sections treated with (a) untreated (b) TPZ (c) PR509 and (d) PR509E. The green color represents regions with Pimonidazole and the blue represents DAPI nuclear stain.

2.5 Discussion

Hypoxia, mostly chronic, modulates various cellular responses and signaling pathways that lead to selection of aggressive phenotype, malignant progression, invasion and metastasis [41-45]. Hypoxia targeted therapies have been in focus since the last 30 years and are aimed at targeting the treatment limiting regions in the tumor microenvironment. The failure of various extensively studied HAPs calls for an in-depth

analysis of the design and functioning of HAPs as well as the contribution of hypoxia in their efficacy.

Previous studies have shown that incorporation of hypoxia and perfusion imaging techniques (^{18}F -FMISO PET and EPR oximetry) were able to predict the response to TH-302 in squamous cell carcinoma SCCVII, human colon cancer cell line HT29, C6 glioblastomas and 9L gliosarcomas [171, 172]. In this study, I investigated the efficacy of a novel HAP called PR509, its effector PR509E and tirapazamine in tumor xenograft models of non-small cell lung cancer (NCI-H1975) and epidermoid carcinoma (A431). The hypothesis was that information about the baseline oxygenation of tumor pre-therapy could be predictive and can throw light on other factors and complex processes that are involved in the effective working of these hypoxia-activated drugs in-vivo. The PISTOL technique was used in my study measure the tumor oxygenation before and after therapy.

A lower baseline oxygenation in A431 was observed as compared to NCI-H1975 tumors. Previous PET based hypoxia imaging studies have shown the presence of hypoxia in A431 and NSCLC tumors [127, 173-175]. The distribution of hypoxia varies within the tumor regions and therefore the tumor was delineated into central and peripheral regions. A431 tumors had higher baseline intra-tumoral heterogeneity in the oxygenation of center and periphery, with center being more hypoxic. Both A431 and NCI-H1975 tumors responded to the PR509 and PR509E treatments. As expected, the more hypoxic A431 tumors had higher response than the NCI-H1975 tumors. The toxicity of PR509E is independent of the presence of hypoxia and thus highlights two important factors about the multi-kinase inhibitor HAPs: the presence of molecular

targets in the tumors and the toxicity level of the HAP. The efficacy of PR509 was higher as compared to PR509E in NCI-H1975 tumors as evidenced by the tumor doubling times.

Previous clinical studies have shown that most NSCLC tumors acquired resistance against the first generation multi-kinase inhibitors such as gefitinib and erlotinib [176]. The efficacy of EGFR-TKIs is dependent on the expression of wild-type EGFR and the types of mutations in EGFR (sensitizing or resistance inducing) and their level of expression. NCI-H1975 expresses the double-mutant L858R/T790M EGFR which imparts resistance against tyrosine kinase inhibitors [177], while A431 has overexpression of wild type EGFR [178]. EGFR receptors are over-expressed in regions with tumor hypoxia and are known to contribute towards increase tumor proliferation and resistance to therapy [179]. The efficacy of PR509E in A431 demonstrates that hypoxia was not the sole contributor towards the efficacy and that over-expression of EGFR kinases also contributed towards it. The efficacy of PR509E and PR509 in NCI-H1975 tumors indicates the possibility that hypoxia was a contributor towards increased efficacy of PR509 than its effector. Studies conducted over TH4000, the analog of PR509 have shown that TH4000 was able to overcome the resistance to conventional tyrosine kinase inhibitors such as erlotinib in mutant EGFR NSCLC model [80]. Hypoxia is known as a driving factor for resistance to therapy, but it is not always the case in all the cancer subtypes [55]. It is important that HAPs are able to target the hypoxic regions that are contributing towards resistance to conventional therapies. The effect of PR509 in NCI-H1975 tumors shows that it was able to target the highly aggressive, tumor promoting regions of the tumors.

TPZ, on the other hand, showed a completely different efficacy between A431 and NCI-H1975. Despite the fact that A431 tumors were more hypoxic, the TPZ treatment was only effective in NCI-H1975 tumors. The mild activation threshold of TPZ might affect its diffusion range, resulting in early metabolism of the drug before reaching the severe hypoxic regions of the A431 tumors [180]. Previous studies have shown that TPZ does not work well with highly dense tumors [181-184]. The lower edema fraction of A431 tumors indicates more cellularly dense tumors as compared to NCI-H1975 tumors. The drug has also been known to exert a limited bystander effect [185]. Overall higher levels of baseline hypoxia may indicate poorer perfusion, leading to lower transport of the pro-drug and hence reduced efficacy.

The determinants of HAP efficacy have been discussed in detail in section 1.1.3. It is also important to identify the expression of reductases to predict sensitivity of the tumor cells to the effector. Analysis for the presence of these reductases in A431 and NCI-H1975 cell lines would assist in analyzing the response and correlate with the results obtained. The efficacy of HAP is also dependent on the half-life of the cytotoxic counterpart. A longer half-life would enable the effector to target more regions in the tumors before being metabolized and excreted. The effector should have high potency and ability to kill cells in different pH and different cell cycles states such as proliferating as well as non-proliferating, which are predominantly present in the hypoxic regions.

Therapy induced changes in oxygenation are an important factor for examining treatment effect. Previous studies have shown that treatment with EGFR-TKIs gefitinib and erlotinib resulted in tumor regression as well as a decrease in hypoxia in NSCLC

tumors [173, 186]. PR509 inhibits the proliferation and differentiation in the tumors expressing the EGFR family of tyrosine kinase receptors, thereby resulting in the tumor regression in some tumor models. EGFR has been shown to regulate angiogenesis [92, 187] and thus inhibition of EGFR via PR509 might explain the reduction in oxygenation post PR509 therapy in NCI-H1975 tumors and no significant improvement in the oxygenation of A431 tumors.

In NCI-H1975, the TPZ treatment resulted in a significant decrease in the oxygenation of tumor centers at day 5 and day 10 post-treatment, which is in agreement with the previous studies that show tirapazamine causes vascular shutdown in the center of the tumor [188-191]. This pattern was further validated by the significantly higher hypoxic fraction (obtained from pimonidazole staining) in TPZ treated NCI-H1975 tumors as compared to the untreated control. The successful treatment with PR509 and its effector resulted in an increase in the oxygenation of A431 tumors. While in NCI-H1975 tumors, PR509 resulted in maintaining the oxygenation of tumor centers and a significant increase in the tumor periphery. On the other hand, PR509E treated tumors had a reduction in the oxygenation of tumor centers at day 15 post-treatment.

With the use of the PISTOL technique we were able to determine the baseline levels of oxygenation and the intra-tumoral heterogeneity in tumor. The technique was also successful in determining the therapy-induced changes in tumor oxygenation can differentiate between the different levels of hypoxia. Pimonidazole is considered to be a gold-standard for hypoxia and thus we analyzed the distribution of hypoxia post-therapy. The hypoxic fractions obtained from IHC cannot be used to differentiate between mild

hypoxia, severe hypoxia and anoxia. Pimonidazole is limited to the tumor regions that are well perfused and thus might fail to generate an accurate map of distribution of hypoxia.

A potential limitation of our current PISTOL probe is that pO_2 measurements can only be extracted from the regions that contain HMDSO droplets, which might not represent the oxygenation of the entire tumor. Keeping this limitation in mind we aimed at depositing the HMDSO droplets uniformly at a single plane in the tumor. The significant differences observed in the center vs. periphery of the tumors suggest that this method was able to report the heterogeneity in the tumors. There is also a possibility that HMDSO droplets might fall in the anoxic or necrotic regions of the tumor, affecting the measured mean pO_2 , thus it is necessary to consider this experimental limitation and exclude pO_2 measurements from such regions in future.

The results obtained so far show us that there not a direct correlation between HAP efficacy and occurrence of hypoxia. Identification of predictive hypoxic biomarkers in individual patients is critical in designing a treatment plan and evaluating response of HAP therapies. Given the heterogeneity of hypoxia and perfusion in different tumor types and also within different patients, there is need for improved stratification strategies and also for development of novel and better hypoxia targeted/activated therapeutics. Screening of multiple tumor models for hypoxia and their response to the HAPs is necessary in planning therapies and development of better therapeutics. The parameters such as oxygen consumption and its dependence on pO_2 measured for various cancer cell types add to our understanding of the metabolic consequences of cancer progression and provide an opportunity to engineer new therapeutics.

CHAPTER 3

QUALITATIVE MRI ASSESSMENT OF CHANGES IN TUMOR HYPOXIA POST HYPOXIA-TARGETED THERAPY USING A NOVEL HYPOXIA-TARGETING T₁ CONTRAST AGENT-GdDO3NI

3.1 Abstract

The goal of this study was to investigate the potential of GdDO3NI in generating high-resolution maps of tumor hypoxia before and after administration of hypoxia activated therapy. The r_1 and r_2 relaxivities of GdDO3NI at 7 T were measured to be $4.75 \pm 0.04 \text{ mM}^{-1} \text{ s}^{-1}$ and $7.52 \pm 0.07 \text{ mM}^{-1} \text{ s}^{-1}$ respectively, in deionized water. GdDO3NI was able to report the baseline distribution and intensity of hypoxia in non-small cell lung cancer xenograft models (NCI-H1975) as well as a response to the hypoxia activated pro-drug tirapazamine. Heterogeneous distribution of hypoxia was found within the NSCLC tumors. The agent was able to differentiate between the hypoxic vs. normoxic regions in the tumor. NCI-H1975 tumors had a hypoxic fraction of 0.48 ± 0.28 and a normoxic fraction of 0.45 ± 0.26 . The baseline mean percentage enhancement (i.e. the hypoxic intensity) was found to be $23\% \pm 6.5\%$. Tirapazamine was effective in slowing down the growth in treated tumors as compared to the untreated control tumors ($p < 0.05$). An increased distribution of hypoxia was observed post Tirapazamine treatment as compared to the untreated control tumors ($p < 0.05$). Furthermore, a significant increase was observed in the hypoxic intensity of untreated control tumors from baseline. GdDO3NI is

therefore a promising hypoxia imaging agent for detection and evaluating the modulations of hypoxia non-invasively and longitudinally.

3.2 Introduction

Hypoxia is a physiological condition associated with various pathologies, including cancer, ischemic heart disease, peripheral vascular disease and stroke [192]. Given that hypoxia is a prominent contributor toward tumor growth and therapeutic resistance, it is important to evaluate the presence, distribution and degree of hypoxia before and after therapeutic interventions. A hypoxia mapping technique that can provide accurate three-dimensional maps of degree and distribution of hypoxia non-invasively and in real time could assist clinicians in therapy planning and potentially improve the treatment outcome.

Despite advances in imaging techniques, there is still a lack of an efficient hypoxia imaging technique that can provide accurate, high-resolution 3-D distribution and intensity maps of hypoxia longitudinally and non-invasively in the clinical setting. Hypoxia is highly variable throughout the tumor and information about its location and intensity in the tumors can assist clinicians in determining the radiation dosage, region of maximum impact and also drug combinations to improve therapy outcome. As a 3D hypoxia mapping agent [152], GdDO3NI has the potential to provide accurate maps of the distribution and severity of hypoxia before and after therapeutic interventions. Preliminary in-vivo studies carried out on nu\mu mice implanted subcutaneously with NCI-H1975 (NSCLC) tumor cell line demonstrated the efficacy of GdDO3NI in reporting regions of hypoxia when compared with the gold-standard pimonidazole.

Briefly, 1 mm thick T₁-weighted images were acquired pre and post intra-peritoneal injection of 0.3 mmol/kg body weight GdDO3NI for every 5 minutes up to 130 minutes post injection to a total time of 150 minutes. Pimonidazole was used as an ex-vivo marker for hypoxia and tumors were harvested for IHC staining. A single MR percentage enhancement image corresponding to the pimonidazole stained image was co-registered. R² values between the tumor boundaries and hypoxia boundaries were then determined using custom MATLAB code to determine the degree of correlation for the images. When registered, the tumor boundaries yielded R² values of 0.9034 and hypoxia-thresholded R² values of 0.4752 (figure 3.1). The preliminary results motivated us to investigate the baseline heterogeneity in NCI-H1975 tumors and their response to TPZ treatment via GdDO3NI and compare the results with PISTOL analysis.

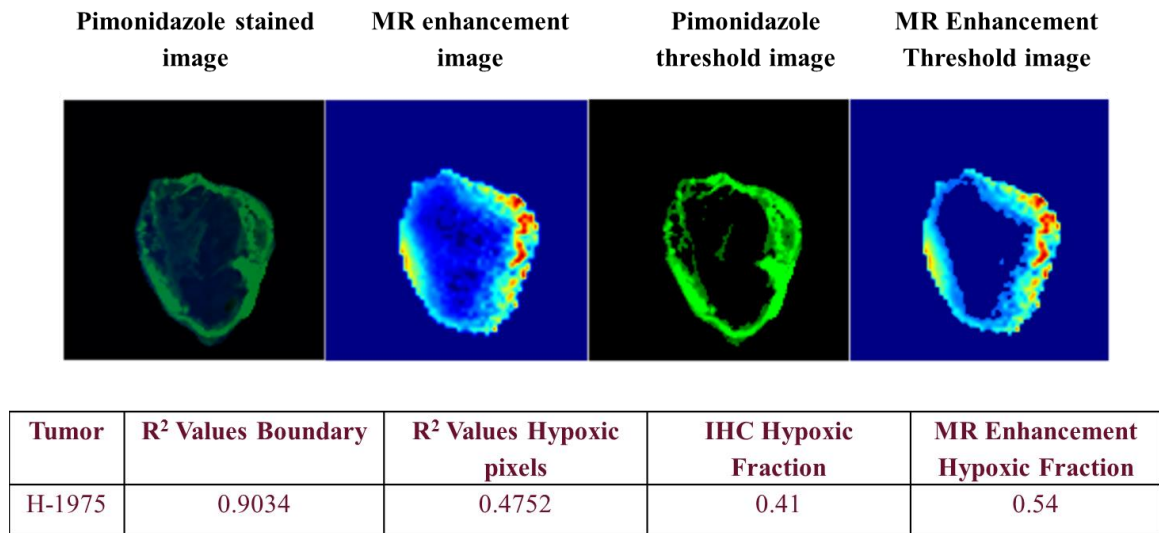


Figure 3.1: Co-Registration and hypoxic thresholding of IHC and MR percentage enhancement images.

3.3 Materials and Methods:

The GdDOTA monoamide conjugate of 2-nitroimidazole, GdDO3NI (molecular weight 0.912 kD), was prepared as previously described [147]. All the MR Studies were performed on a Bruker BioSpec 7 Tesla (7 T) preclinical scanner (Bruker BioSpin Corporation, USA).

3.3.1 Relaxivity measurements

The in-vitro relaxivity studies were conducted at bore temperature (~23.6 °C) and 37 °C. Serial dilution phantoms of GdDO3NI (0-2mM) in deionized water (DI) were prepared. The solutions (100 µl) were added to a 96 well plate that was cut into a 4 × 2 grid and placed inside the magnet on a heated water bed. A volume trans/receiver coil was used to conduct the imaging. The temperature of the phantoms was monitored using a fiber optic probe. A RARE T₁ mapping sequence with a variable TR ranging between 148 ms and 5 s (total 10 TR times) and a TE of 11 ms was used to determine the T₁ of the samples. A MSME T₂ mapping sequence with a variable TE ranging between 11-330 ms (total 30 TEs) and a TR of 2.5 ms was used to determine the T₂ of the samples. The relationship between R_i (1/T_i) values and contrast agent concentration (eqn. 1.1) was used to determine the r_i relaxivity of GdDO3NI (where i = 1 or 2). The T₁ values were obtained at by fitting the acquired T₁ maps to a single exponential, three parameter saturation recovery equation:

$$M_z(t) = M_0(1 - e^{-TR/T_1})$$

The T_2 values were obtained at by fitting the acquired T_2 maps to a single exponential, three parameter saturation recovery equation:

$$M_{xy}(t) = M_0 e^{-TE/T_2}$$

3.3.2 Animal models

Human NCI-NCI-H1975 non-small cell lung cancer cells (ATCC Inc.) were cultured in Roswell Park Memorial Institute (RPMI 1640) media and Dulbecco's Modified Eagle's Medium (DMEM) respectively, supplemented with 1% penicillin/streptomycin and 10% fetal bovine serum (Life Technologies, Carlsbad, CA, USA), in a 5% CO_2 -containing humidified atmosphere at $37^{\circ}C$. Immunocompromised ν/ν mice (5-6/per cohort, Charles River Laboratories) were implanted subcutaneously with $2 \times 10^6/40 \mu l$ cells of the respective cell line in the right thigh. The animals were monitored and maintained as per the guidelines by The Arizona State University Institutional Animal Care and Use Committee (IACUC).

3.3.3 Hypoxia activated treatment

Hypoxia activated pro-drugs have a characteristic hypoxic threshold at which they convert into their toxic counterpart. We wanted to examine the correlation between the baseline distribution and extent of hypoxia in our tumor model with HAP efficacy. The efficacy of hypoxic activated pro-drug tirapazamine (SR 4233) was analyzed in this study. TPZ was administered intra-peritoneally at the dosage of $60 \mu mole/kg/body-weight$ in 5 % dextrose to each mouse after the completion of baseline MR imaging.

In order to determine the efficacy of treatment, tumor volume measurements were made using calipers every 3rd day from the day of baseline imaging and until tumor excision (day 5). The formula for an ellipsoid ($\pi abc/6$), where a , b and c are three longest orthogonal dimensions (with a being the longest), was used to calculate the tumor volumes. Tumor volumes were normalized to baseline imaging volumes and then compared to study the treatment response.

3.3.4 In-vivo MR imaging

11 nu/nu mice were imaged in this study to evaluate the efficacy of the GdDO3NI in mapping the tumor hypoxia pre and post therapeutic intervention. All the imaging procedures were approved by The Arizona State University Institutional Animal Care and Use Committee (IACUC). The imaging was done once the tumors reached $\sim 300 \text{ mm}^3$ in volume. The mice were anesthetized (1.5% isoflurane in Air) and placed inside the magnet on a circulating heated water bed with a mouse body surface coil positioned on the tumor for imaging. The water bed was maintained at 37°C throughout the experiment. Multi-slice T_1 and T_2 maps were acquired pre and post GdDO3NI injection with the following parameters: T_1 mapping with a variable TR of 0.2 – 5 s (9 TRs) and a TE of 8 ms and T_2 mapping with a variable TE of 8-160 ms (15 TEs) and TR of 3 s (FOV= 2 cm \times 2 cm, matrix=128 \times 64 (RO x PE, reconstructed to 128 x 128), slice thickness = 1 mm, resolution 156 μm). The pre-injection T_1 and T_2 mapping images were followed by acquisition of a 3D gradient echo imaging with a TE of 3 ms, TR of 80 ms and an alpha of 35° (FOV= 2 cm \times 2 cm \times 2 cm, matrix=128 \times 64 \times 64 (RO x PE₁ x PE₂, reconstructed

to 128 x 128 x 128)). Three consecutive multi-slice T₁-weighted images (TR/TE = 200/8 ms, FOV= 2 cm × 2 cm, matrix=128 × 64 (RO x PE reconstructed to 128 x 128), slice thickness = 1 mm) were then acquired and were immediately followed by intravenous administration of 0.1 mmol/kg/body-weight of GdDO3NI. Serial T₁-weighted images with the same parameters were acquired every 5 min for a total of 130 min along with two 3D gradient echo images at 60 min and 125 min post-GdDO3NI injection (total 24). TPZ was administered after the completion of day 0 MR imaging and the same imaging protocol was followed at day 5. The following relationship was used to determine the concentration of Gd: $[Gd] = (R_{1,post} - R_{1,pre})/r_1$, where R_{1,pre} and R_{1,post} are the relaxation rates and r₁ is the relaxivity of the contrast agent. The spin-echo based signal equation was used to compute the concentration of the agent for all the T₁-weighted scans.

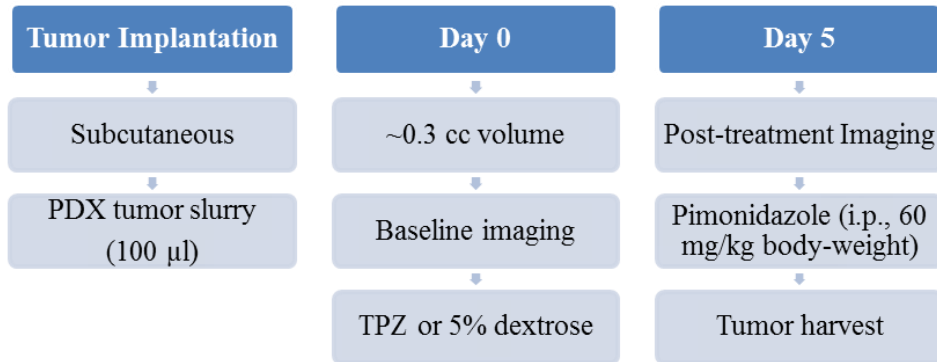


Figure 3.2: Schematic representation of the study protocol.

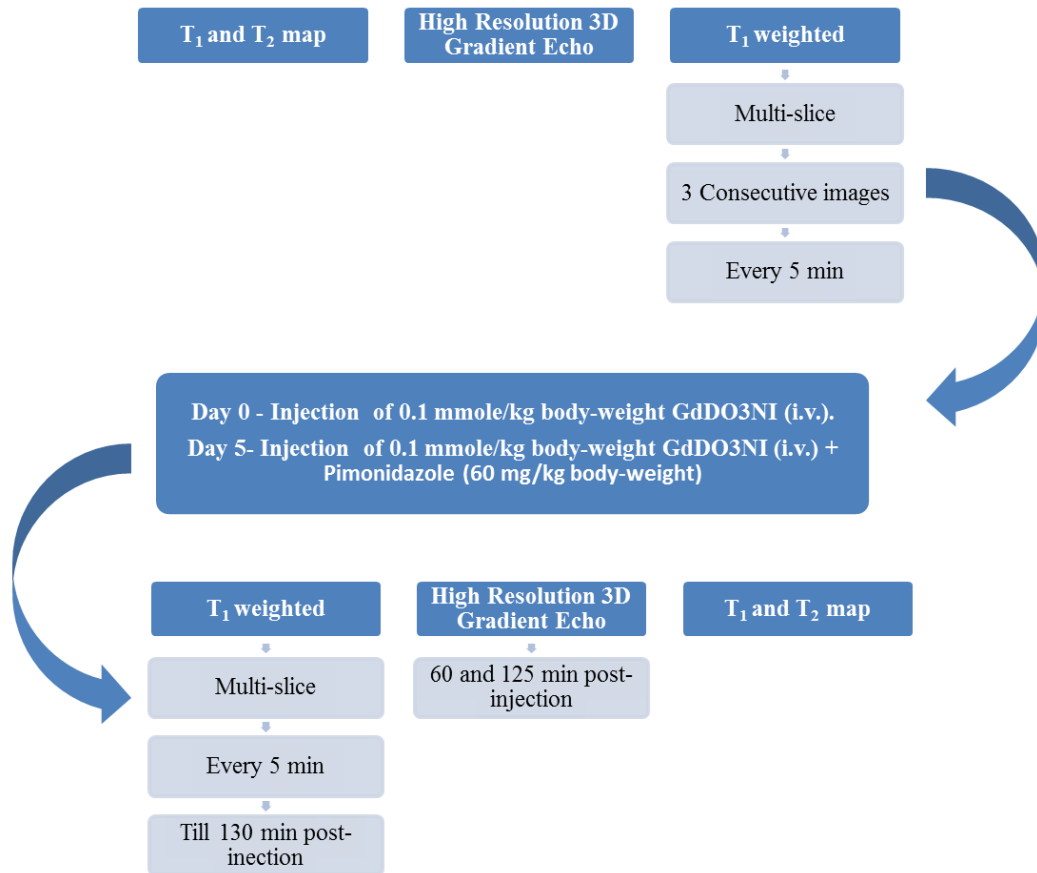


Figure 3.3: Schematic representation of the imaging protocol.

3.3.5. Immunohistochemical analysis of hypoxia

In order to determine the efficacy of GdDO3NI as a hypoxia-imaging agent, we compared the hypoxia distribution pattern with that of gold standard pimonidazole. Pimonidazole HCL (60 mgs/kg/body-weight (Hypoxyprobe Inc.)) was administered simultaneously with GdDO3NI and the tumors were excised immediately after imaging and embedded in optimum cutting temperature compound (OCT). For ex-vivo analysis of hypoxia, 30 μm thick tumor sections (30 sections) at the same imaging plane as MR were obtained using a cryostat. The tumor section were stained with FITC conjugated anti-pimonidazole antibody (1:500) overnight at 4⁰C and counterstained with DAPI (300

nM, nucleic acid stain). The stained section were mounted with Vectashield medium (Vector Laboratories, Burlingame, CA) and visualized under the DMI 6000B Leica Microsystems microscope using the green channel for pimonidazole and the blue channel for DAPI at 5X magnification.

Hypoxic fractions were calculated using a custom made MATLAB code. Briefly, the image was split into blue (DAPI) and green (Pimo) channels. The blue channel images were used to delineate the tumors and applied to green channel image. A region of interest was drawn around a normoxic region in the green channel image and tumor regions with intensity 2 standard deviations above the mean intensity of the normoxic region were considered as hypoxic and used to calculate the hypoxic fraction.

3.3.6 Edema fraction analysis

The protocol for this calculation has been discussed in detail in chapter 2 section 2.3.6. The edema fraction was calculated for both the cohorts before and after treatment. The mean baseline edema fraction for the tumors was calculated by pooling all the tumors together.

3.3.7 Data analysis

A region of interest was drawn on a T_2 -weighted scout image in order to delineate the tumor. A mean of three baseline T_1 -weighted images was computed and used to obtain percentage enhancement maps. The regions with percentage enhancement $>10\%$ as compared to baseline at the 130 min post injection were considered as hypoxic while

regions with >10% enhancement at 90s and <10% at 130 min post-injection time point were considered normoxic and <10% at 90s and <10% 130 min post-injection were considered to be necrotic. Hypoxic fractions for MR images were calculated based on the percentage enhancements maps calculates based on baseline and 130 min post-injection time point T₁-weighted image. The above mentioned threshold for image analysis are based on the previous in-vivo studies conducted with GdDO3NI and its untargeted counterpart GdDO3ABA (Gd-DOTA-(n-butyl)monoamide, control agent) [151]. The analysis of time course changes in signal intensities and contrast agent concentration based on a threshold of 10% showed a significantly higher intensity and concentration of GdDO3NI than GdDO3ABA in tumors at the late time points (i.e. 130 min post injection). A threshold of <10% enhancement was considered to exclude the regions with necrosis as the contrast agents are prone to accumulate in those regions over time via passive diffusion [193]. Previous studies were successful in differentiating the regions with necrosis based on the threshold as validated with ex-vivo hypoxia imaging using pimonidazole [151].

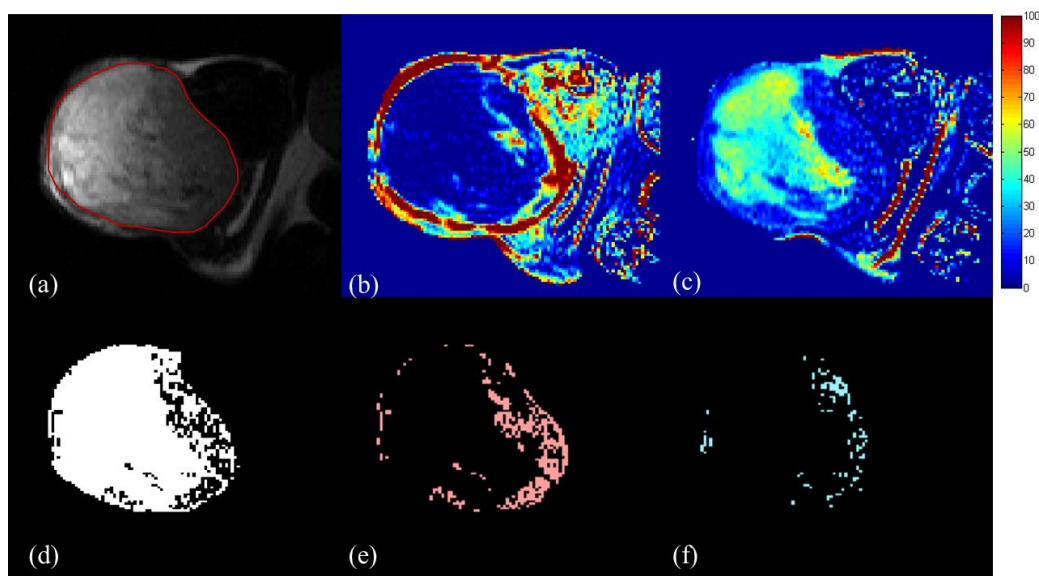


Figure 3.4: Representation of the image segmentation procedure for data analysis. (a) Tumor region with the ROI applied to delineate tumor from thigh region. (b) The percentage enhancement image at (b) 90s and (c) 130 min from the time of injection were used to segment the (e) normoxic (% enhancement <10 % at 130 min post injection and >10% at 90s post injection) and (f) necrotic regions (% enhancement <10 % at 130 min post injection and <10% at 90s post injection). (d) The regions with % enhancement >10% at 130 post-injection were considered hypoxic.

3.3.8 Image registration

The efficacy of GdDO3NI in reporting regions of hypoxia were analyzed by a voxel by voxel correlation with the pimonidazole stained images of the tumors. The mechanism of action for pimonidazole, like other 2-nitroimidazole moiety containing agents, is the irreversible reduction into the hydroxylamine. Thiols play an important role in the binding of pimonidazole in the hypoxic regions. Pimonidazole binds to thiol containing protein such as glutathione and gets trapped in the hypoxic environment.

A strong correlation between the hypoxic maps obtained by the two imaging modalities is indicative of the agent's efficacy. Regions of interest were drawn on a T₂-weighted image and DAPI stained tumor image, and both the images were registered and

the correlation between the ROIs was evaluated using a coefficient of determination, or R^2 . With the images adequately registered, voxel-to-voxel comparison was conducted to show the correlation between the hypoxia maps. A hypoxic threshold of $>10\%$ MR enhancement image was used for the MR images and 2 standard deviations above the mean of normoxic tissue was used for the pimonidazole stained image to calculate the hypoxic fractions. Assuming a normal or Gaussian distribution of the intensity of normoxic regions, approximately 95% of the values would fall between the mean and 2 standard deviation above the mean. Thus choosing a threshold of above the 2 standard deviation would ensure efficient determination of regions with hypoxia. In addition, a structural similarity index between both modalities was used as another metric for establishing the similarity of the images post-thresholding [6], with mean squared error also calculated between the two modalities.

3.4 Results

3.4.1 Baseline tumor hypoxia and edema fraction

The r_1 and r_2 relaxivities of GdDO3NI at 7 T were measured to be 4.75 ± 0.04 $\text{mM}^{-1} \text{s}^{-1}$ and 7.52 ± 0.07 $\text{mM}^{-1} \text{s}^{-1}$ respectively, in deionized water at 37 °C (figure 3.5). 11 NCI-H1975 tumor-bearing animals were studied, 6 mice were given the TPZ treatment and 5 were treated as control (5% dextrose). The mean baseline hypoxic fraction and mean percentage enhancement (using GdDO3NI) of the of NCI-H1975 tumors was found to be 0.48 ± 0.28 and $23\% \pm 6.5\%$ respectively (figure 3.6 A). As expected the mean percentage enhancement of the normoxic region was significantly

lower at $3.7\% \pm 4\%$, but the normoxic fraction was found to be similar to hypoxic fraction at 0.45 ± 0.26 (figure 3.6 B). A threshold of 10% and above enhancement from the baseline was used to calculate the hypoxic fractions. The mean baseline edema fraction of the tumor model was 0.12 ± 0.03 .

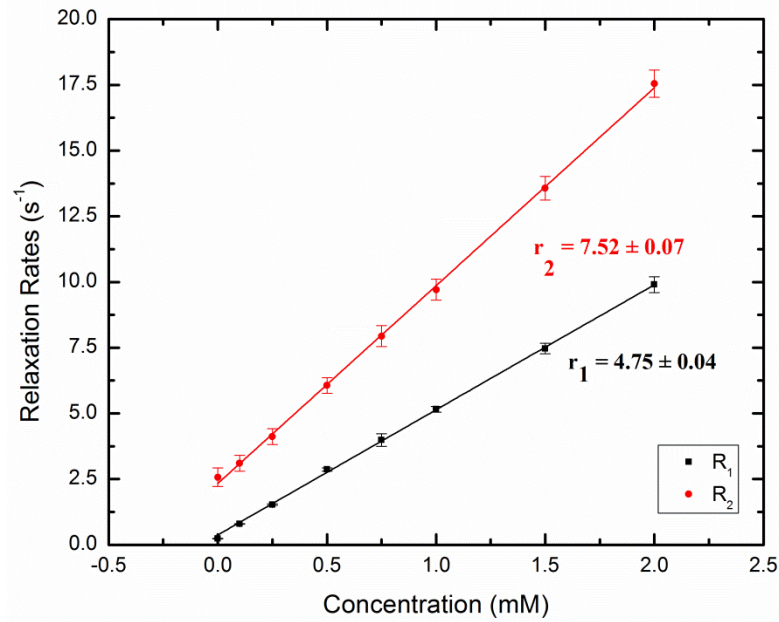


Figure 3.5: Relaxivity of GdDO3NI at 7 T, in DI at 37 °C.

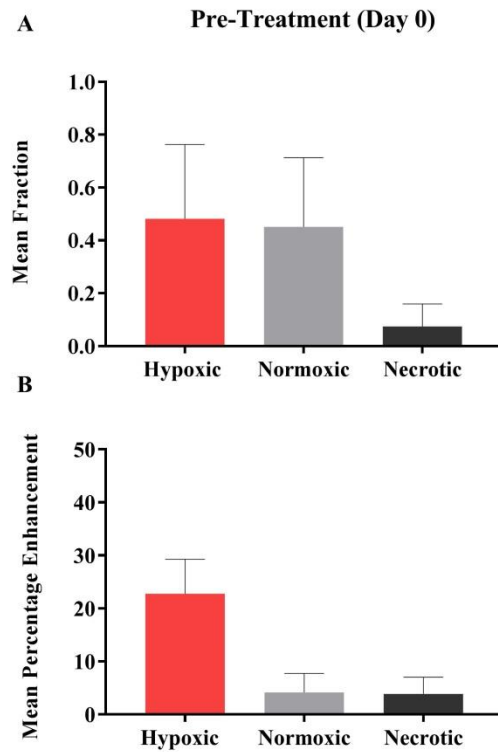


Figure 3.6: Baseline distribution and intensity of hypoxia in NCI-H1975 tumors (n =11).

A correlation analysis between the baseline distribution (figure 3.7 A) and severity of hypoxia (figure 3.7 B) with the tumor volumes showed that the presence of hypoxia was not dependent on the tumor size.

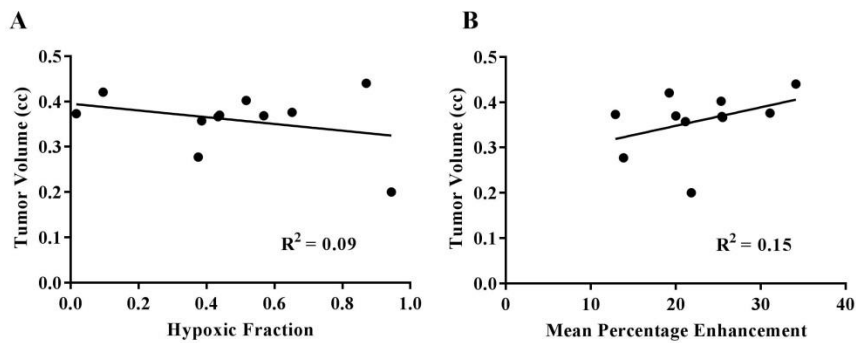


Figure 3.7: Correlation analysis between baseline characteristics of hypoxia and tumor volume.

3.4.2 Treatment response

3.4.2.1 Tumor volume and edema fraction

The efficacy of the HAP treatment was determined by analyzing the normalized mean tumor volume differences between the treated and untreated control cohorts. The mean normalized tumor volumes of TPZ treated NCI-H1975 tumors (2.1 ± 0.28) were significantly lower than the untreated control tumors (2.7 ± 0.50 $p < 0.05$) at day 5 (figure 3.8). The treatment resulted in an increase in the edema fraction of TPZ treated tumors at day 5 (0.15 ± 0.05) from day 0 (0.11 ± 0.03 , $p = \text{ns}$ (not-significant)), while the untreated control tumors did not show any change in the edema fraction at day 5 (0.12 ± 0.04) from day 0 (0.12 ± 0.04) (figure 3.9).

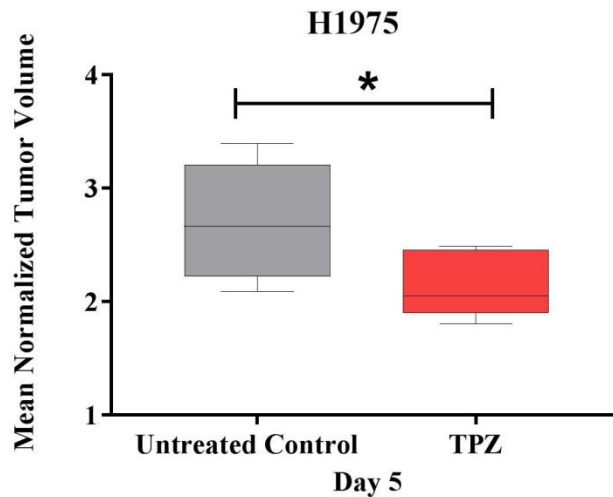


Figure 3.8: Mean of normalized tumor volumes of treated ($n = 6$) and untreated control ($n = 5$) NCI-H1975 tumors (* represents $p < 0.05$). Note: the error bars represents standard deviations.

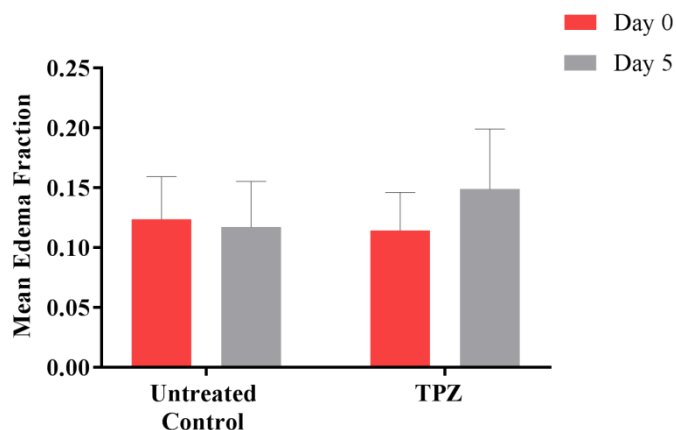


Figure 3.9: The edema fraction before and after treatments. Note: the error bars represents standard deviations.

3.4.2.2 Treatment effect on hypoxic fraction and intensity

Hypoxia is an important indicator of the treatment efficacy and the treatment-induced changes have not been well documented before. I evaluated the changes in mean hypoxic fraction and percentage enhancement in the tumors post-treatment. The hypoxic fraction between the individual cohorts did not show a significant difference from their baseline levels. We observed that TPZ treated tumor had a significantly higher hypoxic fraction at day 5 than the untreated control tumors (figure 3.10 A). The mean percentage enhancement of the tumors increased for both TPZ and untreated control tumors at day 5, although the changes were only significant for untreated control tumors (figure 3.10 B). The mean percentage enhancement of TPZ tumors was higher than the untreated control, but the difference was not significance ($p < 0.09$).

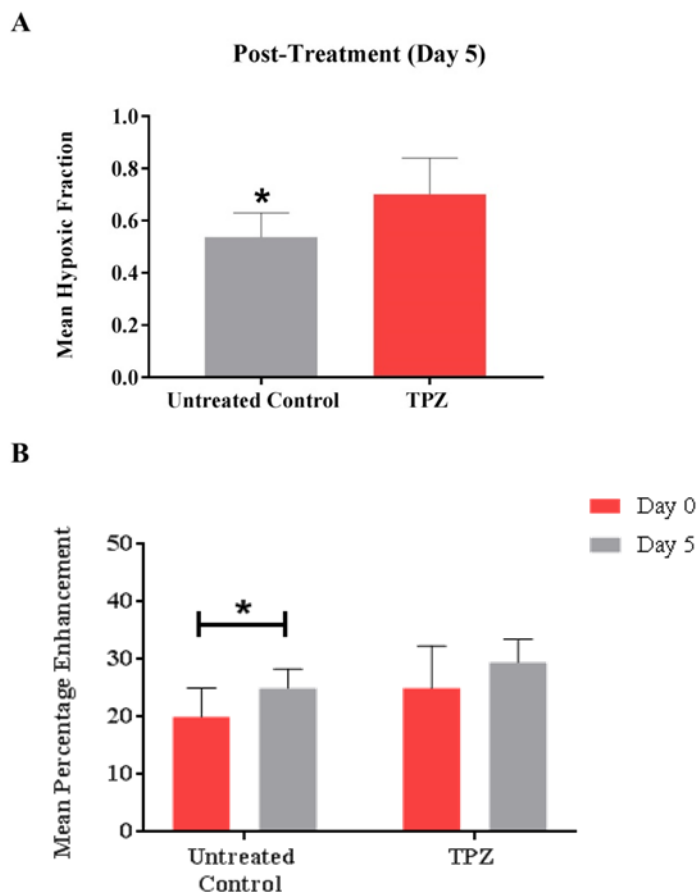


Figure 3.10: The treatment induced changes in distribution and intensity of hypoxia (* represents $p < 0.05$). Note: the error bars represents standard deviations.

3.4.3 Kinetics of GdDO3NI in NCI-H1975 tumors

We investigated the time course changes in the mean percentage enhancement of both the cohorts. Figure 3.11 shows the time course changes in the concentration of the agent for both hypoxic and normoxic regions of the cohorts. The concentration maps were generated from the enhancement maps for each animal pre and post therapy. Quantitatively, the peak concentration of the agent was $41 \pm 10 \mu\text{M}$ in TPZ treated tumors and a peak concentration of $33 \pm 10 \mu\text{M}$ in untreated control tumors ($p = \text{ns}$). The analysis of time course of Gd concentration showed that the time to reach peak

concentration was faster pre-treatment as compared to post treatment for both the treatment groups. As, expected the peak concentrations were higher for the normoxic regions followed by a rapid clearance of the agent.

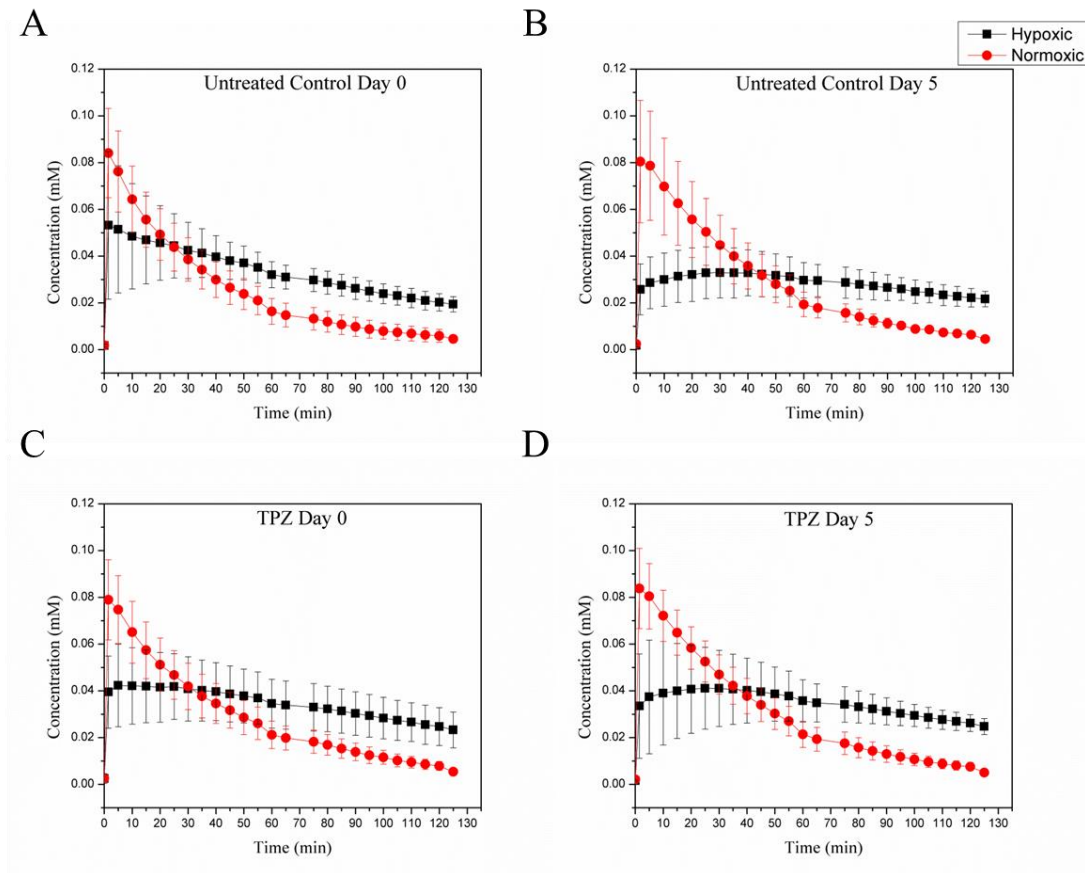


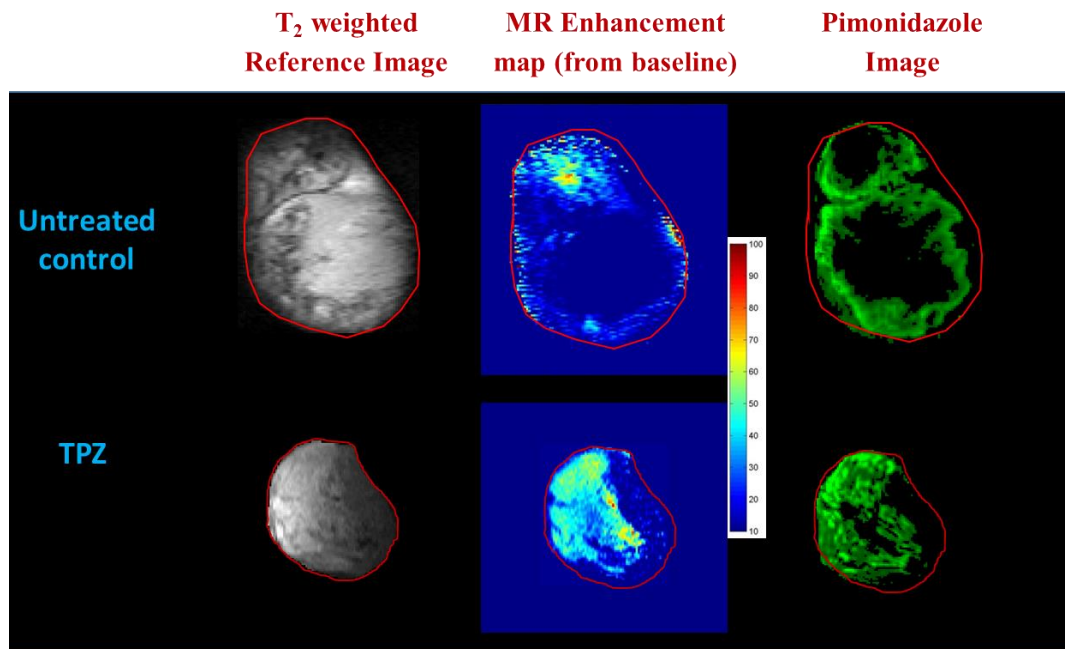
Figure 3.11: The kinetics of mean agent concentration for normoxic and hypoxic regions in NCI-H1975 tumors.

Linear fitting of mean concentrations for end time points (100-125 min post injection) showed no significant difference between the slopes of hypoxic vs. normoxic regions as well as between pre and post treatment hypoxic regions. As expected, linear fitting the early time point (15-35 min post injection) Gd concentrations showed a

significant difference between the slopes of normoxic vs. hypoxic regions for both the treatment groups.

3.4.4 Co-registration of MRI and IHC images

We analyzed one TPZ-treated and one untreated control tumor for correlation analysis. Pimonidazole staining of the NCI-H1975 tumors confirmed the presence of hypoxia within the tumors. Because our goal was to compare the hypoxia maps obtained by GdDO3NI, we conducted a voxel by voxel comparison between the MR and IHC images (figure 3.12). A single 30 μm thick microcopy image was compared with 1 mm thick MR percentage enhancement image. The image similarity indices also showed a strong correlation for each image, with 0.7295 for H-1975 TPZ treated tumor and 0.6737 for untreated control tumor. This is a strong metric for determining how similar two images are, taking into consideration luminance, structure, and contrast between images to measure image similarity. R^2 values were also collected for both hypoxic regions as well as tumor boundaries, shown in figure 3.12. A high correlation was obtained between the boundaries of the DAPI stained image and the corresponding T_2 weighted image. The R^2 comparisons didn't show favorably between the hypoxic maps of the modalities as did the structural similarity index. Mean-squared errors were very small, however, further showing strong correlation between modalities.



	Pimo Hypoxic Fraction	MR Hypoxic Fraction	Boundary R ²	Hypoxia R ²	Image Similarity Index	Root Mean-Squared Error
Untreated control	0.5281	0.4790	0.9391	0.2900	0.6737	0.1208
TPZ treated	0.6631	0.8127	0.9265	0.5243	0.7295	0.0817

Figure 3.12: The correlation analysis between pimonidazole stained tumors vs. MR obtained hypoxia maps.

T₂ weighted reference image

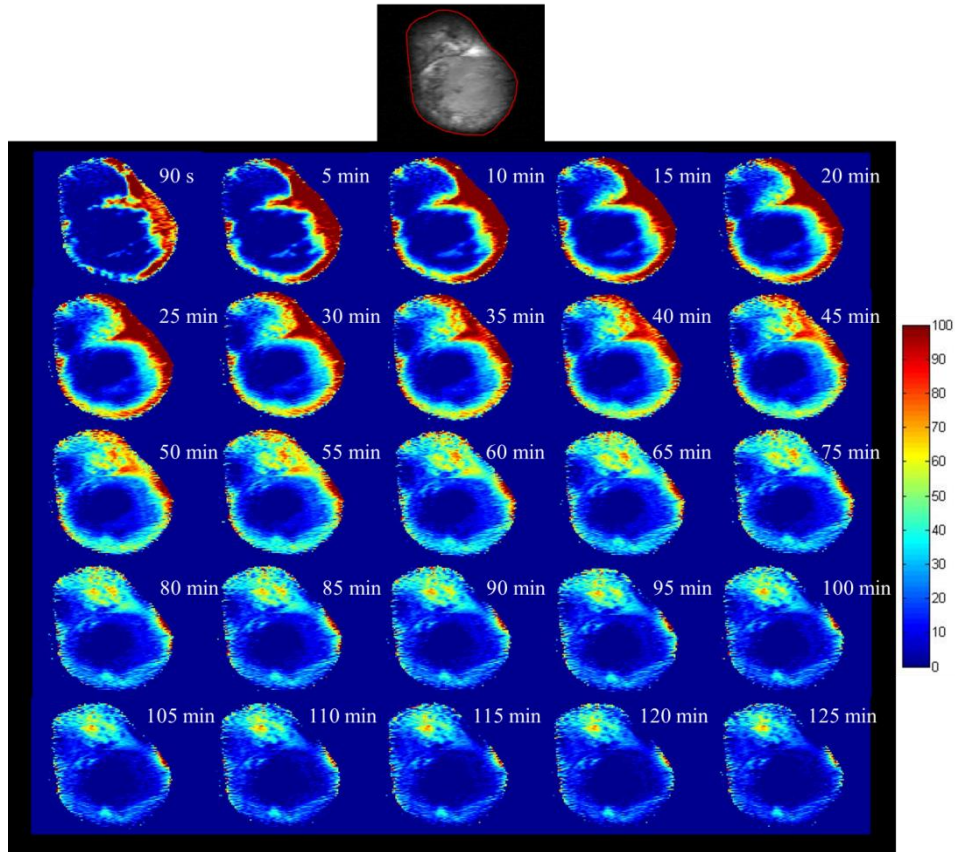


Figure 3.13: Percentage enhancement maps of a single slice of untreated control NCI-H1975 tumor at 125 minutes post-injection of GdDO3NI with respect to pre-injection intensity. The region of interest used to delineate the tumor is shown in the T₂ weighted reference image.

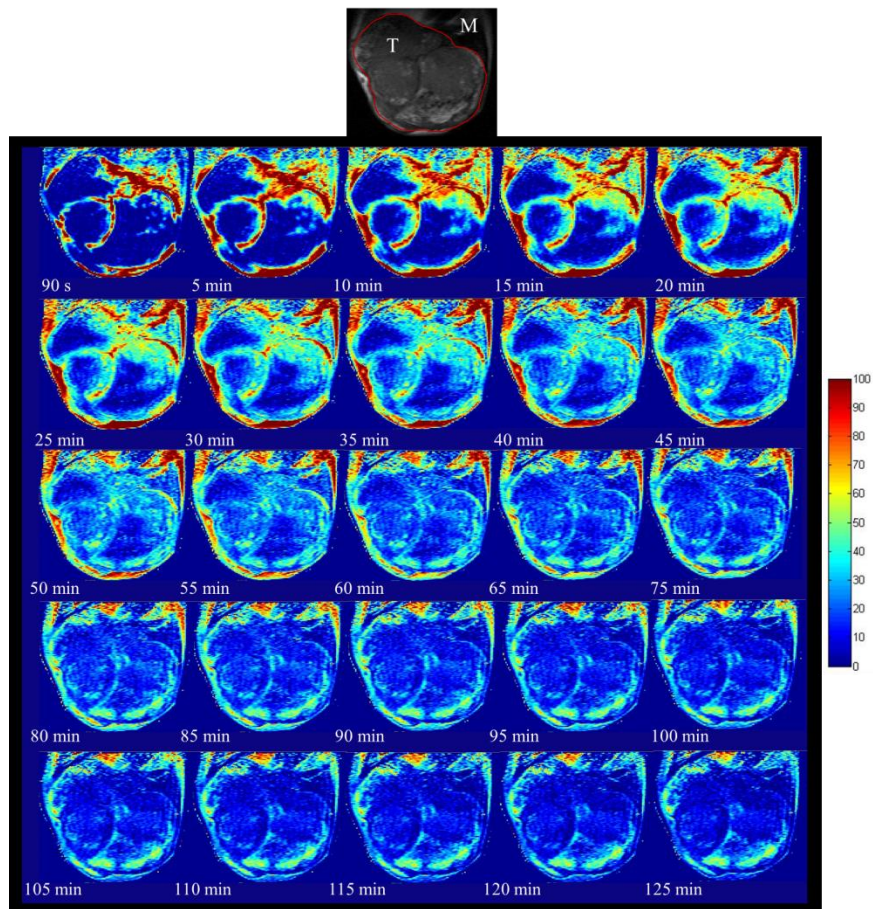


Figure 3.14: Percentage enhancement maps of a single slice from the same NCI-H1975 untreated tumor (at a distance of 5 mm from the previous slice) at 125 minutes post-injection of GdDO3NI with respect to pre-injection intensity. The region of interest used to delineate the tumor is shown in the T₂ weighted reference image. T and M represent the tumor and muscle regions.

T₂ weighted reference image

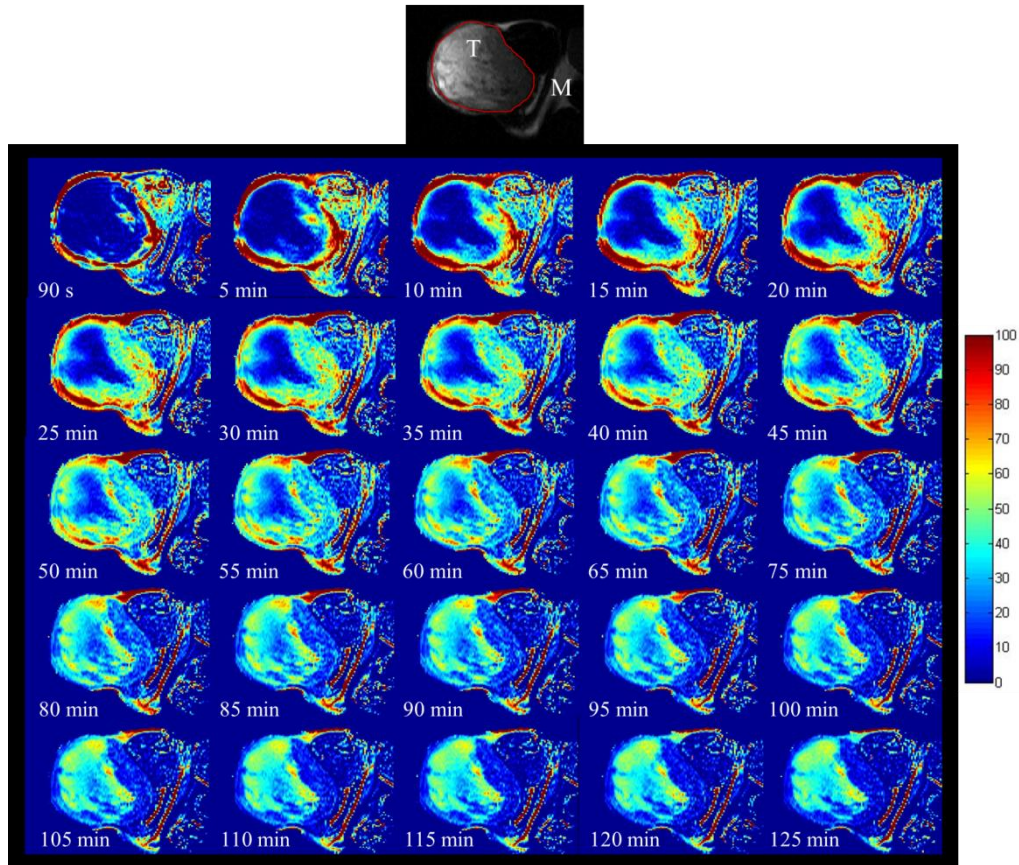


Figure 3.15: Percentage enhancement maps of a single slice of TPZ treated NCI-H1975 tumor at 125 minutes post-injection of GdDO3NI with respect to pre-injection intensity. The region of interest used to delineate the tumor is shown in the T₂ weighted reference image. T and M represent the tumor and muscle regions.

3.5 Discussion

The hypoxia targeting ability of GdDO3NI has been validated previously in-vitro and in-vivo using 9L glioma cells incubated under hypoxia and AT1 xenograft models respectively [147, 151]. The goal of this study was to demonstrate the efficacy of our hypoxia binding T_1 contrast agent GdDO3NI in reporting the distribution and extent of tumor hypoxia, evaluate the efficacy of TPZ and its effect over the hypoxia of non-small cell lung cancer tumors.

The non-small cell lung cancer model NCI-H1975 was chosen to be studied as the preliminary analysis conducted via GdDO3NI was able to show presence of hypoxia in the tumor model. The relaxivity properties of the agent at 7 T were found to be similar to the relaxivities obtained at 4.7 T [151] and also to the other conventional Gd based MR contrast agents [194]. The slight decrease in T_1 relaxivity can be attributed to the increase in magnetic field strength.

We first evaluated the baseline properties of hypoxia within the tumors. NCI-H1975 tumors had high hypoxic fraction of about 48%, which has been seen in previous studies conducted with ^{18}F -FMISO or ^{18}F -FETNIM [195, 196].

It is important to note that solid tumors that are grown subcutaneously are prone to be more hypoxic than the orthotopic models [30]. The contribution of necrotic regions were excluded from all the analysis as the agent is prone to accumulate in those regions due to passive diffusion which has been seen by both targeted as well as non-targeted contrast agents [193]. HAPs impart their toxicity to hypoxic cells by converting into their toxic counterpart in the presence of hypoxia, thus baseline oxygenation of the tumors

could aid in predicting the therapeutic response. TPZ treatment resulted in a significant decrease in tumor growth as compared to the untreated control, which is consistent with the observation of baseline hypoxia within the NCI-H1975 tumors.

Therapeutic modulation of tumor hypoxia is an important indicator for therapy effect and the changes have not been well studied. The hypoxic fraction results indicate an increase in the distribution of hypoxia within the tumors post TPZ as well as untreated control tumors. Several studies have documented that effective TPZ treatment results in vascular shutdown in xenograft models of tumors, resulting in increased hypoxia in the central regions of the tumors [188-191]. TPZ gets converted into its toxic counterpart at relatively moderate hypoxia, thus tumors with higher distribution of moderate hypoxia have the inclination to be more responsive to TPZ treatment.

The variations in the retention of GdDO3NI in tumor regions represent the heterogeneity in the severity of hypoxia (as reflected in mean agent concentrations). GdDO3NI was able to report the treatment induced changes in severity of hypoxia post treatment. Untreated control tumors had a significant increase in the severity of hypoxia ($p < 0.05$), but no significant difference in the distribution of hypoxia. It is important to note that the TPZ resulted in significantly more regions of hypoxia than the untreated control ($p < 0.05$) and a higher percentage enhancement but the difference was not statistically significant for the latter ($p < 0.09$).

The time course evolution of mean percentage enhancement and derived concentrations indicate a delay in accumulation and higher retention of the agent in the hypoxic regions as compared to the normoxic regions. Normoxic regions show faster

accumulation for both pre and post-treatment time points and a fast wash-out. The slower buildup of the GdDO3NI in hypoxic regions is similar to the kinetics of other targeted contrast agents [197].

In order to validate the efficacy of GdDO3NI in reporting regions of hypoxia, I decided to carry out a correlation analysis of MR percentage enhancement images with pimonidazole stained images of the tumors. Pimonidazole is a gold-standard hypoxia marker that is extensively used in the clinic to detect regions of hypoxia [119]. It also contains the 2-nitroimidazole moiety and has a hypoxia binding threshold of <10 torr. Pimonidazole staining confirmed the presence of hypoxia within the tumors which is consistent with the hypoxia maps obtained from MR enhancement images. The correlation between MR hypoxic fractions and pimonidazole hypoxic fraction on a whole tumor level showed much lower R^2 values are much smaller than expected. However, this might be due to the difference in slice thickness between the modalities (1mm for MRI, 30 μm for IHC). The discrepancies in the amount of tissue imaged between the two modalities might lead to significant mismatch in hypoxia assessment between the two techniques. Visually, the hypoxia distribution pattern correlates between the pimonidazole images and GdDO3NI contrast enhancement maps obtained and highlight the agent's ability to effectively report regions of hypoxia. Future work will involve the collection of serial sections of tumor tissues ex-vivo and reconstruction of tumor volume corresponding to the thickness of MR images.

Targeted, non-invasive in-vivo imaging of hypoxia using GdDO3NI has the potential to determine regions with poor oxygenation and differentiate between normoxic

vs. hypoxic tissues. The response of NCI-H1975 tumors to TPZ treatment was in agreement with the baseline distribution of hypoxia as detected by GdDO3NI. A higher resolution imaging of tumor oxygenation is preferable for imaging the spatial heterogeneity of hypoxia which might vary even at smaller distances of $<150\ \mu\text{m}$. MRI can facilitate acquisition of higher resolution 2D images but with longer acquisition times. The clinical imaging with PET is mostly acquired at a resolution of 5 mm and recent developments have led to acquisition at 1 mm resolution [198, 199]. In the current study, we were able to acquire multi-slice T_1 weighted images and 3D gradient echo images at a high resolution of $156\ \mu\text{m}$ which is better suited for evaluating the heterogeneity in tumor hypoxia. GdDO3NI has shown the ability to bind to hypoxic regions in both well and poorly perfused regions of a tumor. The agent can also be utilized to monitor the behavior of tumor hypoxia as a response to hyperoxic breathing for patient stratification. The voxel-by voxel analysis of GdDO3NI kinetics can provide crucial information regarding the tumor's perfusion. Further advancement in the understanding of contrast kinetics of the agent can facilitate extraction of quantitative $p\text{O}_2$ values and differentiate between the mild, moderate and severe levels of hypoxia.

CHAPTER 4

MRI ASSESSMENT OF CHANGES IN HYPOXIA AND OXYGENATION IN PATIENT DERIVED XENOGRAFT MODELS OF NSCLC POST HYPOXIA ACTIVATED THERAPY

4.1 Abstract

The development and screening of novel hypoxia activated therapeutics rely on tumor models that can represent the same microenvironmental conditions as seen clinically. Patient derived xenograft models have emerged as an improved platform for pre-clinical evaluation of tumor properties (such genomic and phenotypic markers) and the pharmacokinetics and pharmacodynamics of novel drugs. The goal of the current study was to examine the hypoxic environment of two different non-small cell lung cancer PDX models and their response to hypoxia activated pro-drug, tirapazamine. The efficacy of both PISTOL and GdDO3NI as hypoxia imaging techniques were examined and compared. The M112004 PDX models had significantly higher baseline hypoxia than the M1005 PDX model ($p < 0.01$) as measured by PISTOL and GdDO3NI. The tirapazamine treatment resulted in an increase in extent and severity of hypoxia in the M1005 tumors ($p < 0.05$). The application of both the oximetry techniques has the advantage of providing functional and physiological information of hypoxia that can benefit the scientific community in improving the treatment protocol.

4.2 Introduction

Animal models of rodents with compromised immune system are routinely used in pre-clinical studies to screen novel chemotherapeutic agents for their toxicity, efficacy and pharmacokinetics [200-203]. The subcutaneous xenograft models of established cell lines have been the most studied models in-vivo because of their ease of development and extensive genetic information available, but they lack the relevant heterogeneity in mutations and sub-population of tumor cell types that are present in a patient's tumor [204, 205]. Thus, these models might fail in representing the clinical therapeutic response. The failure of recent promising HAPs in the clinical trials have called for inclusion of patient stratification strategies based on hypoxia and also for improved pre-clinical tumor models that can faithfully replicate the environment and characteristics of a clinical tumor. Patient derived xenograft models are developed by extracting tumor fragments from a patient's tumor and propagating them in rodent models, thus eliminating the 2D growth cycle which removes the selection bias that 2D cell culture go through. Patient derived xenograft models retain the genetic mutations and phenotypic heterogeneity of the parent patient tumor [205-209]. They also represent the tumor vasculature, invasiveness, metastatic potential, morphology, molecular markers and cellular diversity of the tumor [203, 210-214]. Thus, patient derived xenograft models are better suited for pre-clinical evaluation of tumor properties.

I have previously reported the behavior of a NCI-H1975 cell line based model of NSCLC before and after tirapazamine intervention in chapters 2 and 3. Given the importance of tumor microenvironment and its components in defining the effect of a

treatment, we decided to evaluate the baseline oxygenation of NSCLC PDXs in-vivo and their response to the tirapazamine. Multi-modality imaging of hypoxia has the advantage of generating a more comprehensive analysis of tumor hypoxia by combining the strengths of two complimentary imaging techniques, e.g. PET imaging agents combined with quantitative assessment of hypoxia via polarographic needle electrodes [114, 199, 215-218] The hypoxia binding contrast agent GdDO3NI and oxygenation mapping technique PISTOL (Proton Imaging of Siloxanes to Map Tissue Oxygenation Level) have shown the efficacy in reporting regions of hypoxia qualitatively and quantitatively respectively. The combined assessment of oxygenation via GdDO3NI and PISTOL has the potential to provide a more detailed representation of hypoxia that can be used for better treatment planning. In this chapter I report the baseline expression of hypoxia in PDX models of NSCLC and their response to tirapazamine treatment via PISTOL and GdDO3NI imaging.

4.3 Materials and Methods

The MRI contrast agent GdDO3NI was prepared as published previously [147, 151]. All the MR Studies were performed on a Bruker BioSpec 7 Tesla (7 T) preclinical scanner (Bruker BioSpin Corporation, USA).

4.3.1 Animal models

Human non-small cell lung cancer PDX models M112004 and M1005 were provided by Dr. Landon J. Inge (Assistant Professor Norton Thoracic Institute, St. Joseph's Hospital and Medical Center, Phoenix, AZ USA). The PDX models were

passaged in immunocompromised nu/nu mice by implanting tumor chunks of the respective tumor model subcutaneously. The tumors were then extracted and ground using a tissue grinder to form a homogenous tumor slurry and 100 μ l of the slurry was implanted subcutaneously in two cohorts of 10 immunocompromised nu/nu mice for each PDX model (therefore 20 mice for each PDX model in total). The animals were monitored and maintained as per the guidelines by The Arizona State University Institutional Animal Care and Use Committee (IACUC).

The NSCLC PDXs were derived from patient tumors collected under an IRB approved protocol (#07HL029) at St. Joseph's Hospital and Medical Center. NSCLC PDXs (M1005, M112004) were derived from patients without evidence of metastatic disease and previous treatment, undergoing routine resection [219].

4.3.2 Hypoxia activated treatment

As stated in earlier studies it is important to examine the correlation between the baseline levels of hypoxia in our tumor model with HAP efficacy. The efficacy of hypoxic activated pro-drug tirapazamine (SR 4233) was analyzed in this study. TPZ was administered intraperitoneally at the dosage of 60 μ mole/kg/body-weight in 5% dextrose to each mouse after the completion of baseline MR imaging. 5% dextrose was administered to the untreated control cohort. Tumor volume measurements were made and analyzed using the same protocol described in chapter 2 and 3.

4.3.3 MR imaging protocol

The imaging was conducted on the mice once the tumors reached $\sim 300 \text{ mm}^3$ in volume. The following imaging protocol was followed for both the tumor models: Baseline (day 0) PISTOL maps were acquired by following the same protocol as described in chapter 2. Briefly, neat HMDSO (Sigma Aldrich., 10-50 μL) droplets were deposited in a fan pattern along a single plane in the tumors and mice were then placed on a mouse bed. A mouse surface receiver coil was placed over the tumor. The body temperature of mice was maintained by keeping them on a heated water-bed at 37°C . Pre GdDO3NI injection multi-slice T_1 and T_2 maps were acquired with the following parameters: T_1 mapping with a variable TR of 0.2 s – 5 s (9 TRs) and a TE of 8 ms and T_2 mapping with a variable TE of 8-160 ms (15 TEs) and TR of 3 s (FOV= 2 cm \times 2 cm, matrix=128 \times 64 (RO x PE, reconstructed to 128 x 128), slice thickness = 1 mm, resolution 156 μm). Three consecutive PISTOL T_1 maps were then acquired followed by acquisition of a 3D gradient echo imaging with a TE of 3 ms, TR of 80 ms and an alpha of 35° (FOV= 2 cm \times 2 cm \times 2 cm, matrix=128 \times 64 \times 64 (RO x PE₁ x PE₂, reconstructed to 128 x 128 x 128)). Three consecutive multi-slice T_1 -weighted images (TR/TE = 200/8 ms, FOV= 2 cm \times 2 cm, matrix=128 \times 64 (RO x PE reconstructed to 128 x 128), slice thickness = 1 mm) were then acquired and were immediately followed by intravenous administration of 0.1 mmol/kg/body-weight of GdDO3NI. T_1 -weighted images with the same parameters were then acquired every 5 min for a total of 130 min. Two 3D gradient echo images were acquired at 60 min and 125 min post-GdDO3NI injection. Post

injection T_1 and T_2 maps were acquired with the same imaging parameters as pre-injection. At the end of the day 0 imaging protocol, respective therapy (TPZ or 5% dextrose) was injected intraperitoneally. Pimonidazole HCL (60 mgs/kg/body-weight (Hypoxyprobe Inc, Burlington, Massachusetts, USA)) was administered along with GdDO3NI on day 5.

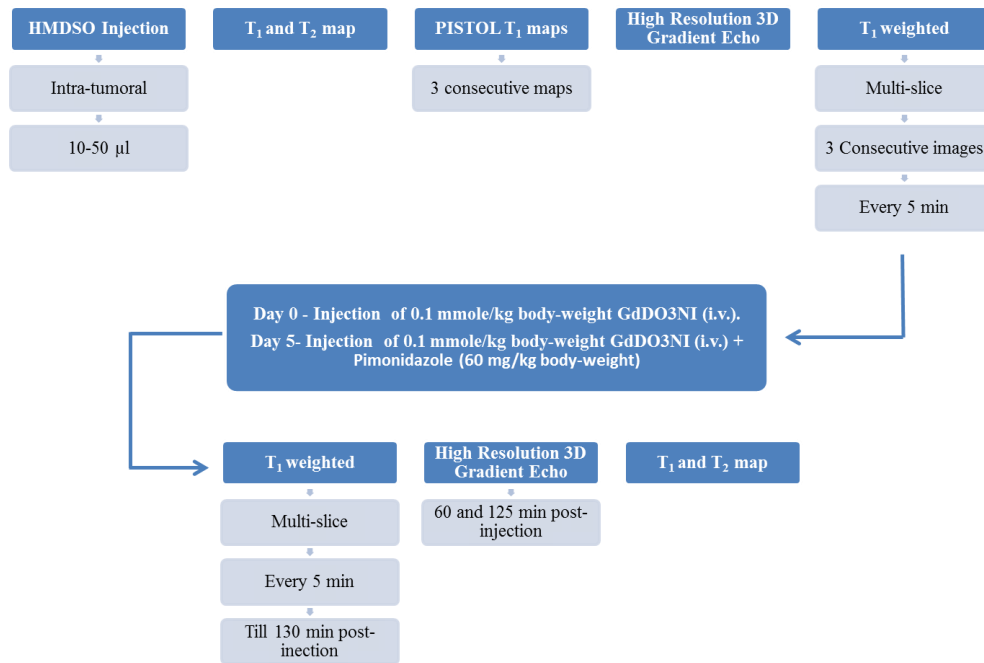


Figure 4.1: Schematic representation of the imaging protocol.

4.3.4 Data analysis

The oxygenation maps from the PISTOL sequence were obtained via the same procedure as described in chapter 2. The pre and post GdDO3NI MR images were also analyzed as described in chapter 3. Edema fraction analysis was also conducted via the

same protocol. For statistical analysis, t-tests (unpaired or paired) were used and an alpha of <0.05 was considered significant.

4.4 Results

4.4.1 Baseline tumor oxygenation and edema fraction

18 M1005 and 14 M112004 tumor-bearing animals were studied in total using PISTOL technique. The M1005 tumors had a mean baseline oxygenation of 43 ± 16 torr, similar to the mean baseline oxygenation of M112004 tumors at 47 ± 10 torr (figure 4.2). The tumors were segmented into center and periphery based on the T_2 weighted images. The M112004 tumors had higher baseline intra-tumor heterogeneity in the tumor oxygenation with center being more hypoxic than the periphery, while M1005 tumors had similar oxygenation throughout the tumor. The hypoxic fraction (a measure of distribution of hypoxia) of the M1005 (0.59 ± 0.21) and M112004 (0.70 ± 0.29) tumors were similar (figure 4.3 B). Due to unforeseen loss of few mice with M112004 tumors resulted in a small sample size for the GdDO3NI imaging ($n = 2$ for untreated control and $n = 4$ for TPZ treated). A threshold of 10% and above enhancement from the baseline was used to calculate the hypoxic fractions. The mean hypoxic intensity (i.e. mean percentage enhancement $>10\%$) analysis showed that M112004 tumors ($30 \pm 9\%$) were significantly more hypoxic than the M1005 tumors ($19 \pm 3\%$, $p < 0.01$, (figure 4.3 A)). The comparison between the baseline oxygenation of tumor centers of both the PDXs also confirmed the observation with M112004 (38 ± 17 torr) having significantly lower oxygenation than the M1005 tumors (47 ± 14 torr). M112004 (0.14 ± 0.08) had

significantly higher mean baseline edema fraction than the M1005 tumors (0.08 ± 0.03 , $p < 0.01$, (figure 4.4)).

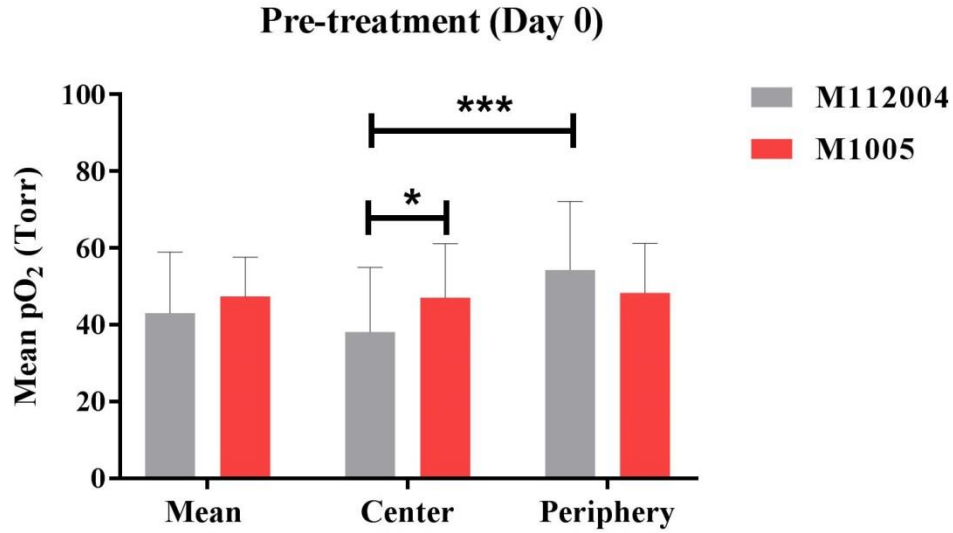


Figure 4.2: Baseline mean oxygenation of M112004 (n = 14) and M1005 PDX tumors (n = 18, * represents $p < 0.05$ and *** represent $p < 0.001$). Note: the error bars represents standard deviations.

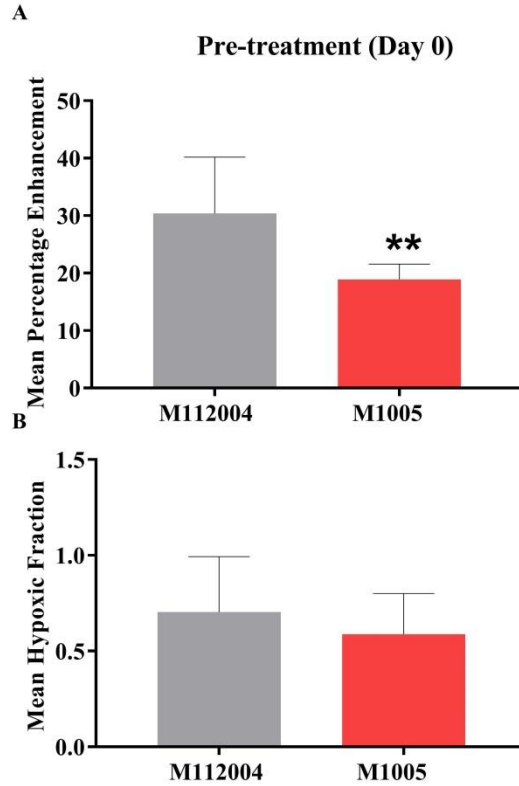


Figure 4.3: The baseline distribution and intensity of M112004 (n = 6) and M1005 PDX tumors (n = 11, ** represents $p < 0.01$). Note: the error bars represents standard deviations.

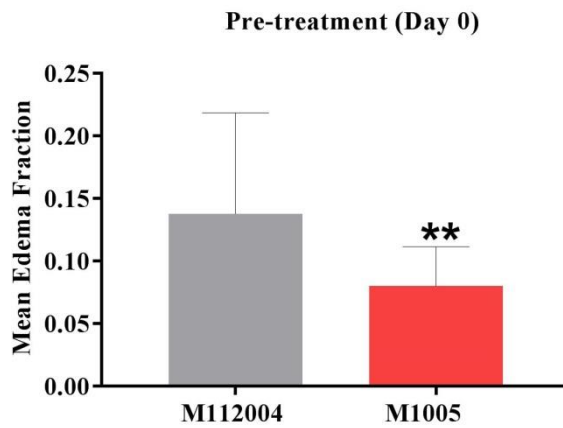


Figure 4.4: Baseline mean edema fraction of M112004 (n = 14) and M1005 PDX tumors (n = 16, ** represents $p < 0.01$). Note: the error bars represents standard deviations.

4.4.2 Treatment response

4.4.2.1 Tumor volume and edema fraction

The efficacy of HAP treatment was evaluated by comparing the tumor volumes pre and post treatment as well as changes in the baseline oxygenation. The mean normalized tumor volumes of both the TPZ treated PDX tumors were not significantly different than the untreated control tumors (figure 4.5). No significant changes were observed in the edema fraction too for both the PDX models (figure 4.6).

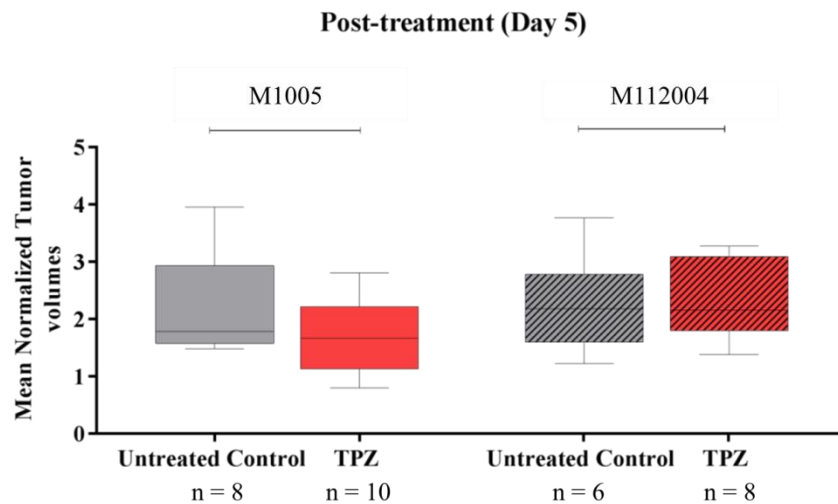


Figure 4.5: The mean of normalized tumor volumes post-treatment of M112004 and M1005 PDX tumors. Note: the error bars represents standard deviations.

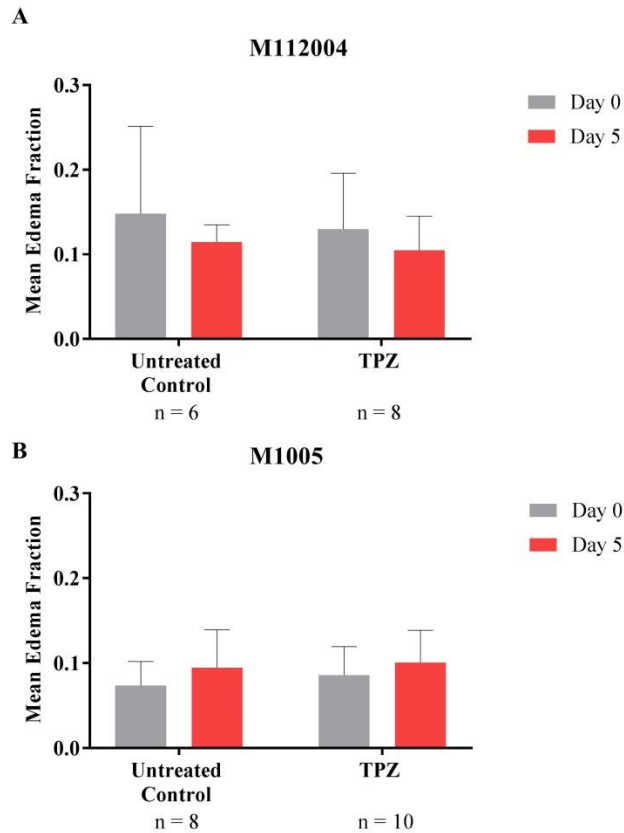


Figure 4.6: The mean edema fraction post-treatment of M112004 and M1005 PDX tumors. Note: the error bars represents standard deviations.

4.4.2.2 Treatment induced changes in oxygenation

Because our goal was to investigate the treatment induced changes in oxygenation, we compared the mean oxygenation between pre and post treatment. The untreated control M1005 and M112004 tumors did not show any significant changes in the mean oxygenation from baseline (figure 4.7 (A) and figure 4.8 (A) respectively). The center of TPZ treated M1005 tumors showed a significant decrease in the oxygenation from baseline (figure 4.7 B) while M112004 tumors showed no significant changes from the baseline (figure 4.8 B).

The comparison between oxygenation of center and periphery post-treatment to evaluate intra-tumor heterogeneity showed that the centers of M12004 untreated control tumors were significantly more hypoxic than the periphery (figure 4.8 A). The M1005 untreated control tumors also had lower oxygenation in the tumor centers as compared to the periphery, but the difference was only close to significance ($p < 0.06$, figure 4.7 A).

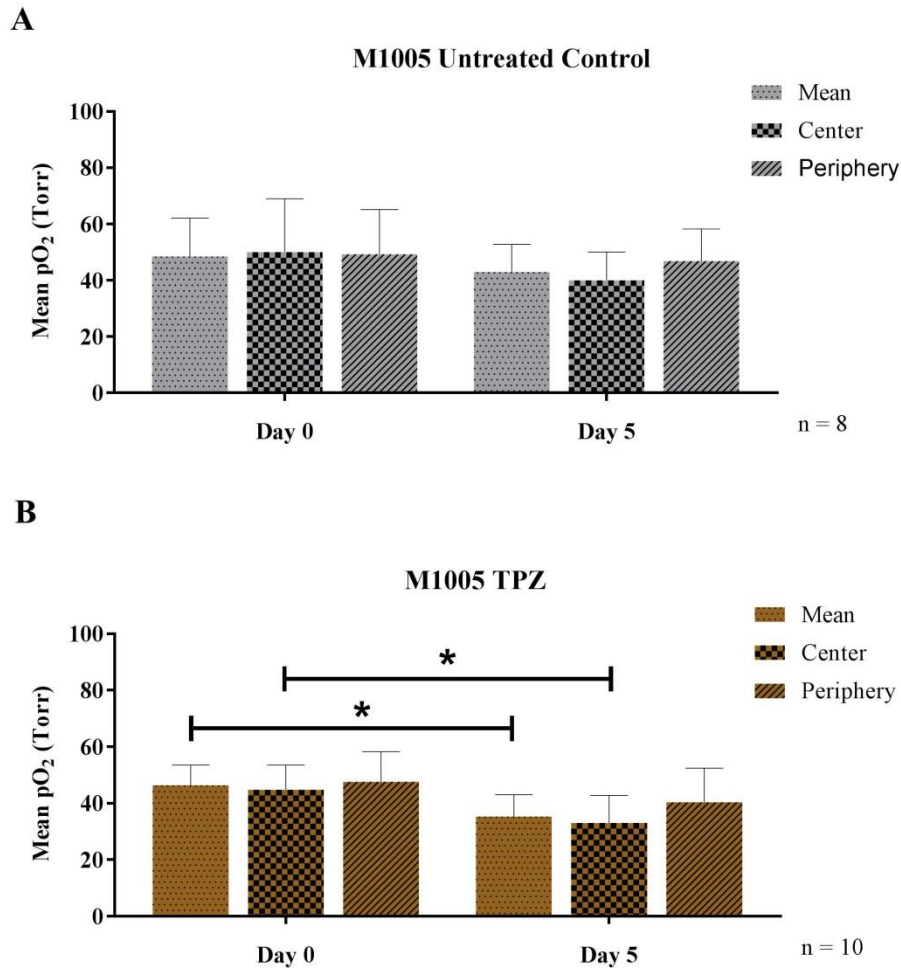


Figure 4.7: The changes in oxygenation post therapy in M1005 PDX tumors (* represents $p < 0.05$). Note: the error bars represents standard deviations.

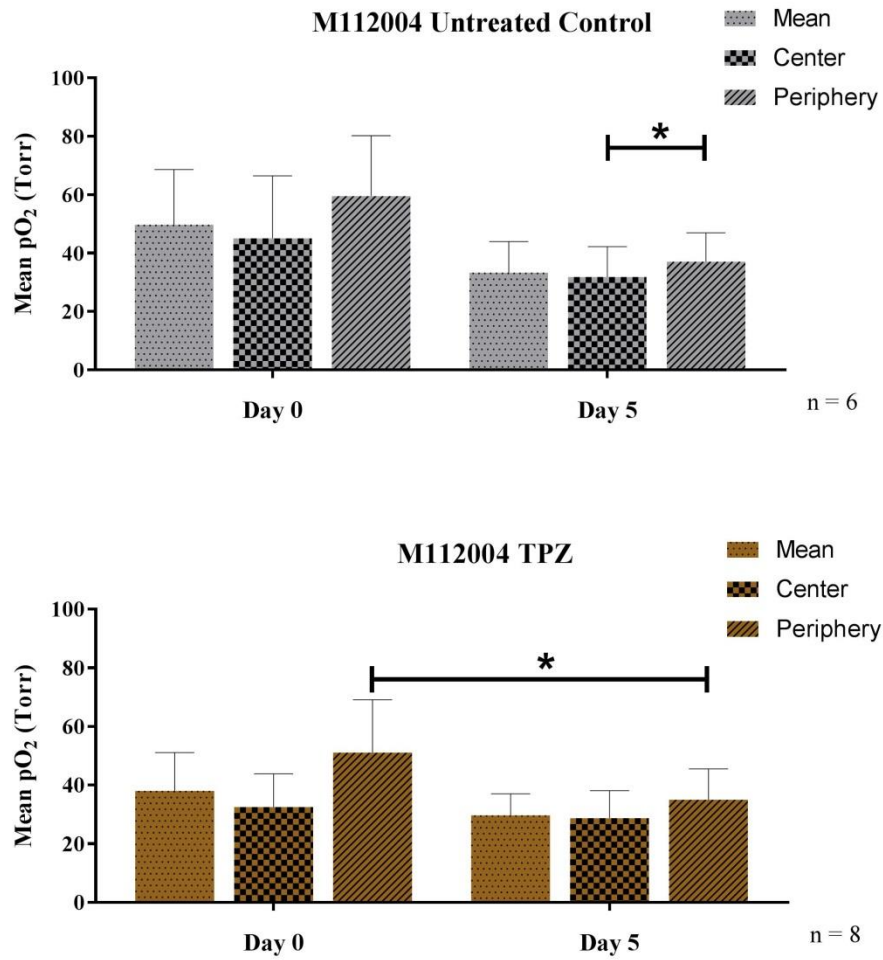


Figure 4.8: The changes in oxygenation post therapy in M112004 PDX tumors (* represents $p < 0.05$). Note: the error bars represents standard deviations.

Table 4.1: Mean oxygenation of M112004 and M1005 PDX tumor models pre and post-treatment.

Tumor Model	Treatment		Mean pO ₂ (torr)	
			Day 0	Day 5
M112004	Untreated Control (n = 6)	Mean	50 ± 18	33 ± 11
		Center	45 ± 21	32 ± 10
		Periphery	58 ± 18	37 ± 10*
	TPZ (n = 8)	Mean	38 ± 13	30 ± 7
		Center	32 ± 11	29 ± 9
		Periphery	51 ± 18	35 ± 11
M1005	Untreated Control (n = 8)	Mean	49 ± 14	43 ± 10
		Center	50 ± 19	40 ± 10
		Periphery	49 ± 16	47 ± 11
	TPZ (n = 10)	Mean	46 ± 7	35 ± 8
		Center	45 ± 9	33 ± 10
		Periphery	48 ± 11	40 ± 12

4.4.2.3 Hypoxic fraction and intensity

Next, I analyzed the hypoxic fraction and mean percentage enhancement of the treated and untreated control PDX models to evaluate the treatment induced changes in the entire tumor. While PISTOL is efficient in providing the quantitative information, it is limited to the regions receiving the HMDSO droplets. No significant difference was observed in the distribution of hypoxia in M112004 tumors post-therapy (figure 4.9 A). The TPZ treatment of M1005 tumors resulted in significant increase in the hypoxic fraction of the tumors, while no significant difference was observed in the untreated control tumors (figure 4.9 B).

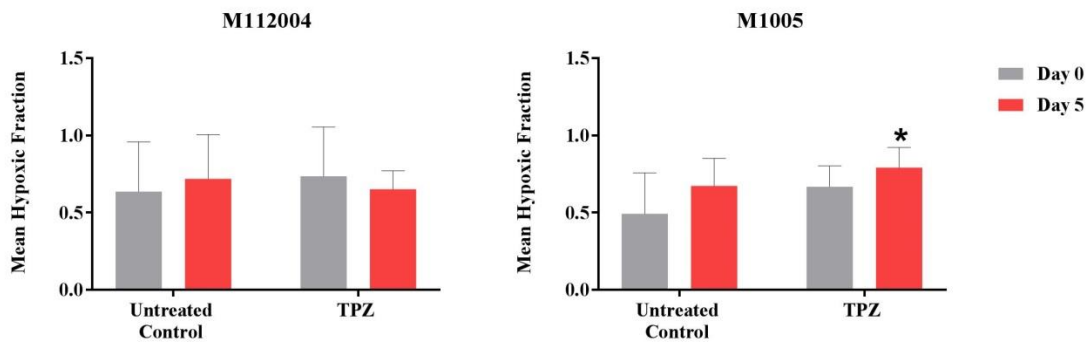


Figure 4.9: The changes in hypoxic fraction post therapy in M112004 and M1005 PDX tumors (Untreated control and TPZ treated M1005 n = 5 and 6 respectively, untreated control and TPZ treated M112004 n = 2 and 4 respectively).

The mean percentage enhancement for M1005 tumors treated with TPZ increased from their baseline levels, although the difference was only close to significance ($p < 0.08$, figure 4.10 B). The comparison between the PDX cohorts (i.e. TPZ/Untreated control-M1005 vs. TPZ/ Untreated control -M112004) showed no significant differences, which

means that the distribution and severity of hypoxia were similar for both the tumor models post therapy.

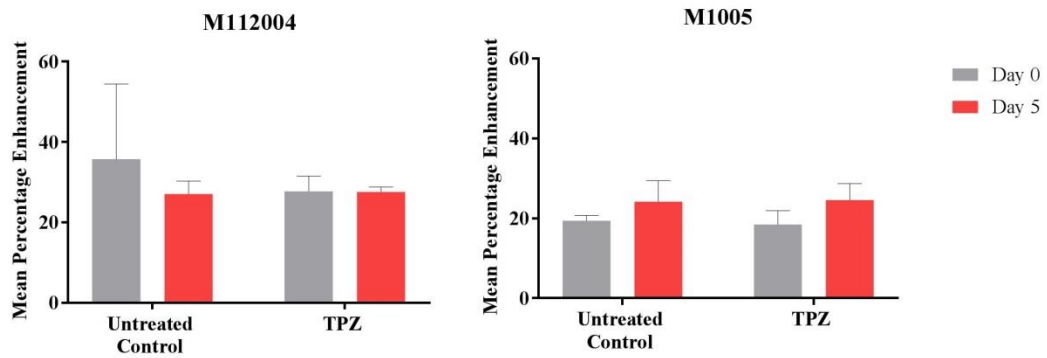


Figure 4.10: The changes in hypoxic intensity post therapy in M112004 and M1005 PDX tumors (Untreated control and TPZ treated M1005 n = 5 and 6 respectively, untreated control and TPZ treated M112004 n = 2 and 4 respectively).

4.5 Discussion

The constituents of the tumor stroma are a key contributor towards the development of tumor microenvironment and play a major role in promoting proliferation, invasion, angiogenesis, and metastasis and also in response to therapy [15, 220]. The tumor stromal components and the induced microenvironment differ significantly between different tumor types, tumor grades and might also differ between different patients with the same tumor type. The NSCLC tumors in humans have a cocktail of mutations that are unique to each patient's tumor [221, 222]. These mutations are relevant in determining the therapeutic efficacy of targeted drugs that are dependent on the expression of molecular targets for imparting toxicity. The PDX models maintain the mutation characteristics of the clinical tumors, thus the drug efficacy can be expected to closely resemble that seen in clinical studies. Previous studies have shown that PDX models were able to replicate the chemotherapeutic responses as seen in parent tumor [212, 223, 224].

The goal of this study was to investigate the behavior of two different patient derived xenograft models of non-small cell lung cancer (M112004 and M1005), that showed resistance to conventional therapies, as a response to hypoxia activated therapy tirapazamine. The changes in distribution and severity of hypoxia therapy were studied via both quantitative and qualitative oximetry techniques, simultaneously.

The oximetry studies via PISTOL and GdDO3NI showed that M112004 were more hypoxic and had more intra-tumor heterogeneity than M1005. The higher edema fraction points towards higher fluid build-up in the tumors and lack of vasculature in

poorly-differentiation M112004 tumors as compared to the well-differentiated M1005 tumors [219].

M1005 tumors were more responsive towards the TPZ treatment than M112004 tumors. Ideally, we would expect tumors with higher oxygenation to be less responsive to the hypoxia activated therapeutics and vice a versa. Tumors with severe hypoxia or larger tumor volumes might exacerbate the penetration of TPZ into the central regions of the tumors. The tumor centers of M112004 were more hypoxic than the periphery, which might result in the inability of TPZ to reach the more hypoxic and aggressive regions of the tumor. As discussed before, TPZ has a mild hypoxia activation threshold and suffers from a poor bystander effect. But as discussed in detail before, the presence of hypoxia is not the only factor responsible for governing the treatment efficacy. Hypoxic regions are known to be distributed throughout the tumor, but not all the regions equally contribute to the treatment resistance, thus is it important to locate the treatment limiting hypoxic regions of the tumor that provide a niche for the more aggressive phenotype and cancer stem cells.

We would expect a higher efficacy of the drug TPZ in M112004 tumors, but the tumors were completely un-responsive to TPZ. Results have also shown that TPZ does not work well with dense tumor models as its early metabolism due to mild activation threshold in the low density hypoxic regions compromises its penetration towards more hypoxic regions. The post-TPZ treatment reduction in the oxygenation in M1005 tumor centers might be due to the vascular disruptive nature of TPZ. There was a decrease in

oxygenation and also an increase in the regions with hypoxia in M1005 tumors post TPZ therapy.

Because the goal was to investigate the differences between the hypoxic behaviors of PDX models vs. the established cell line model, we compared the oxygenation data between NCI-H1975 and the PDXs. No significant differences were observed in the distribution of hypoxia between the NCI-H1975 and PDX models. Quantitative oxygenation data showed that M112004 tumor centers were found to be more hypoxic than the NCI-H1975 tumors.

These results show that the complexity of the tumor microenvironment and its interaction with HAPs is a multifactor process. The incidence of hypoxia, its severity, its effect on the treatment resistance and tumor progression needs to be evaluated for efficient treatment planning. As discussed in chapter 2, the efficacy of any HAP is dependent on several factors. Molecular profiling of both the tumor models will give an idea of all the genetic mutations that could be relevant to predicting the outcome of HAP therapies that target specific molecular markers. The PDX models are an excellent platform to test the novel therapeutics, test the different combinatorial treatment protocols and for novel drug designing due to their ability to maintain the clinical genetic and phenotypic state of the tumor. Studies conducted in pancreatic tumor xenografts in both subcutaneous and orthotopic models showed unusually high levels of hypoxia in subcutaneous models as compared to orthotopic models [225]. Studies have also shown that the response of tumors against therapies was dependent on the location and microenvironment of the tumor [226, 227]. It is important to note that the genetic

framework of a tumor results in the characteristic tumor microenvironment, thus PDX models are an efficient model for replicating the interaction of the HAP with the tumors. But the lack of an efficient vascular network and immune response are some of the limitations faced by subcutaneous models grown in immunocompromised mice. The relationship between the incidence of hypoxia and immune response are still being understood. Thus, orthotopic tumor models with clinically relevant expression of hypoxia and tumor vasculature might be a better platform than subcutaneous models for evaluating the novel HAPs.

Our study shows that the combined application of PISTOL and GdDO3NI has the potential to provide quantitative and qualitative oxygenation data of a tumor which can aid in selecting and categorizing patients based on their hypoxic distribution and severity, for designing of better therapeutic protocol based on the tumor's response and for determining the optimum time and region of impact for maximum outcome of radiation therapy.

CHAPTER 5

CONCLUSIONS & FUTURE DIRECTIONS

Cancer is a ‘rogue’ organ with its own unique microenvironment, molecular markers, signaling pathways and organization of vasculature that have all been transformed to promote its growth [4]. Since hypoxia plays an important role on the tumor progression and disease resistance, it is important to develop and evaluate hypoxia targeting and imaging techniques that can improve the clinical therapeutic response. The primary goal of these studies was to test the hypothesis that prospective identification of hypoxic tumors is important in predicting the therapeutic response and for development of personalized treatment protocols. I analyzed the baseline characteristics of hypoxia in pre-clinical models of human cancer using two MRI oximetry techniques unique to our lab (GdDO3NI and PISTOL) and monitored their response to hypoxia activated therapy in terms of tumor size and changes in oxygenation.

First, I investigated the efficacy of a novel HAP called PR509, its effector PR509E and tirapazamine in tumor xenograft models of non-small cell lung cancer (NCI-H1975) and epidermoid carcinoma (A431). I used the recently developed PISTOL technique to map the tumor’s baseline oxygenation and the therapy-induced changes. A lower baseline oxygenation in A431 as well as higher intra-tumor heterogeneity in the distribution of hypoxia was observed as compared to NCI-H1975 tumors. The treatment efficacy of PR509 was in agreement with the expression profile of EGFRs in NCI-H1975 (mutated EGFR) and A431 (wild-type EGFR) as well as with the baseline expression of hypoxia. The effects demonstrated the importance of evaluating the sensitivity of the

tumors towards the effector as well as the ability of HAPs to impart toxicity to the treatment limiting and tumor promoting sub-population of the tumor cells. Next, I reported the ability of GdDO3NI in mapping the distribution and extent of hypoxia in NCI-H1975 and two NSCLC patient derived xenograft models M1005 and M112004 tumors as a response to TPZ treatment. The agent showed r_1 relaxivity comparable to other clinical contrast agents at 7 T [194]. Since hypoxia imaging with GdDO3NI confirmed the presence of hypoxia in NCI-H1975s as reported earlier by PISTOL imaging. The baseline and therapy induced characteristics of hypoxia of both the PDX tumor models were studied via PISTOL as well as GdDO3NI. M112004 tumors were more hypoxic, had more intra-tumor heterogeneity and higher edema fraction than M1005 pre-treatment (i.e. baseline characteristics). The post-TPZ treatment reduction in the oxygenation in M1005 tumor centers might be due to the vascular disruptive nature of TPZ. We observed a decrease in oxygenation but also an increase in the regions with hypoxia in M1005 tumors post TPZ therapy. The TPZ-induced changes in oxygenation of NCI-H1975 tumors, where it was able to slow down the tumor growth, proved the anti-angiogenic property of TPZ, which was in agreement with the previous studies that show tirapazamine causes vascular shutdown in the center of the tumor [188-190].

The response of NCI-H1975, A431, M1005 and M112004 tumors to TPZ revealed that an effective HAP needs to have higher hypoxic threshold, ability to penetrate into the more dense and hypoxic regions of the tumor (potentially containing the cells with more aggressive phenotype) and exert a good bystander effect.

The clinical performance of HAPs has been unsatisfactory. With the inclusion of a hypoxia imaging technique for stratification of patients, the outcome of the drug trials can be improved. The response of our tumor models to HAPs has highlighted the importance of assessing nitroreductase levels, cytotoxicity of the drug, sensitivity of the tumor models to the drug, ability of the drug to kill high-proliferating as well as non-proliferating cells, drug penetration and bystander effect. As discussed before, hypoxia although present in most tumors is not always treatment limiting and it is important to differentiate the treatment limiting regions for predicting the therapeutic efficacy of HAPs. It is important to include the analysis of all the above mentioned factors in assessing the efficacy of a novel HAP in different pre-clinical as well as clinical tumor models for improving the clinical translatability of the drugs.

The pre-clinical screening of novel therapeutic drugs is critical in predicting their efficacy in clinical trials. An efficient model for screening the HAPs should not only have the clinically relevant mutations and also correctly representation of the clinical tumor's vasculature and hypoxia. The tumor vasculature is fundamentally different from the host tissue's vasculature in structure, function and organization [23, 32]. Initially the tumor coopts the vasculature of surrounding tissue and initiates angiogenesis as the tumor grade increases [228, 229]. The occurrence of hypoxia is correlated with the pattern of vasculature and vice a versa, thus hypoxia and tumor vasculature both are important parameters in tumor's growth [230-234]. Recent studies have shown that the location and microenvironment of the tumor defines the pattern of vasculature and hypoxia and in turn the response of tumor to targeted therapies [226, 235]. The incidence of hypoxia is

intertwined with the tumor's microenvironment, thus it is important to screen the efficacy of hypoxia activated therapeutics within in-vivo models that show more clinically relevant representation of hypoxia. PDX models are a better platform than the established cell-line based models due to their ability to maintain the original characteristics of the parent clinical tumor.

The subcutaneous tumors, especially of lung cancer models, are prone to be more hypoxic and necrotic due to the lack of vasculature that is found in orthotopic lung cancer tumors [30]. They also lack the interface between the host tissue and tumor that exists between the orthotopic tumors. The interface of the subcutaneous tumors with fat, muscle and connective tissue found beneath the skin contributes towards variation from the clinical tumors. Thus, incorporation of orthotopic models of NSCLC for evaluation of their baseline oxygenation and response to HAPs via our oximetry techniques should yield more clinically relevant results.

In chapter 4 I was able to show the efficacy in reporting hypoxia by combined application of PISTOL and GdDO3NI imaging. The direct injection of HMDSO into the tumors allows us to measure the oxygenation of regions that might be perfusion limited and thus not able to be reported by GdDO3NI. Similarly, HMDSO droplets cannot be injected over the entire region of the tumors while GdDO3NI can be used to generate 3D maps of hypoxia. For the clinical translation of PISTOL, it is necessary to develop a nano-emulsion based platform for the systemic delivery of HMDSO or other siloxane based reporter molecules. Currently, the oxygenation information via PISTOL is limited to single slice, and implementation of spectral spatial pulses could allow for multi-slice or

3D acquisition of PISTOL maps. Extensive studies have been conducted on the PET hypoxia imaging agent ^{18}F -FMISO or ^{18}F -FAZA and a correlation analysis of GdDO3NI with the PET could be helpful in evaluating the clinical translatability of the MR agent.

I also reported the correlation between the hypoxic maps obtained via GdDO3NI and immunohistochemical staining with pimonidazole. Visually, the hypoxia distribution pattern correlates between the pimonidazole images and GdDO3NI contrast enhancement maps obtained and highlight the agent's ability to effectively report regions of hypoxia. Further modifications in the comparative analysis have potential to improve the correlation results between GdDO3NI and pimonidazole hypoxia maps.

The cancer imaging community could be positively impacted by the availability of two new imaging techniques (one PISTOL and one contrast agent) for imaging tumor hypoxia. Thus this work could impact the broader medical research community by opening a new window into the progression of metastatic diseases. The techniques can be incorporated into routine examination of hypoxia in tumors as they undergo treatments in order to determine the window of opportunity at which the HAPs will be able to result in better treatment outcome. The imaging techniques could also be used to monitor the response of tumors towards the therapies and accordingly modify the treatment plan and dosage. The HAPs have been in development since the past 40 years and yet no single agent has been approved for clinical use. Our techniques have the potential to improve the outcome of clinical results involving HAPs by allowing the clinicians to extract quantitative as well as qualitative distribution and severity of hypoxia within the tumors. The information can be used to formulate the therapy protocol that will result in the

maximum impact. The administration of HAPs as a single therapy is unlikely and combination therapeutic protocols involving HAPs is the future. The goal of combination therapeutics would be to ensure the eradication of hypoxic as well as the normoxic fraction of the tumors. Administration of HAPs with conventional therapies and guided with hypoxia imaging techniques for patient selection has the potential to significantly improve the treatment outcome and clinical translation of HAPs. The combination therapies can be designed based on the mechanism of action of drugs e.g. cytotoxic drugs such as TPZ and TH302 could be administered in combination with radiotherapies and chemotherapies which are inhibited by the hypoxia mediated resistance. The combination therapy of PR509 with anti-angiogenic drugs such as cyclophosphamide could increase the regions that will be affected by PR509 as cyclophosphamide would facilitate the increase in hypoxia. PR509 could also be administered with chemotherapies such as cisplatin and docetaxel that are cytotoxic and target the highly proliferative cells in the tumor. The dosing and schedule of the therapies would be dependent on the mechanism of action of the drugs being administered. Anti-angiogenic drugs could be administered first to increase the regions with hypoxia followed by administration of HAPs. Thus the imaging techniques could impact future patients by aiding the design and development of personalized therapy (e.g. patient stratification for novel hypoxia activated pro-drugs) particularly for cancer and by the potential to improve how radiotherapy is planned and delivered in the clinic.

Possible Future Experimentation: The imaging protocol for generation of oxygenation maps using PISTOL were acquired at a time interval of 5 days, although

smaller intervals of 2 to 3 days could be incorporated into future studies for evaluating of oxygenation changes at early time points post administration of therapy. The acquisition of T₁-weighted images at a higher temporal resolution (< 15 s) up to 15 minutes post-injection of GdDO3NI agent could facilitate the determination of parameters such as volume transfer constant (K^{trans}), extravascular and extracellular volume fraction (v_e) and the rates of transfer of contrast agent (CA) etc using a three compartment model [236-238]. The length of the post-injection scan time can be increased to, say, 180 min from 130 min to evaluate the time course behavior of hypoxic and normoxic regions at later time points. The goal of increasing the number of T₁-weighted scans post-injection would be to achieve a complete clearance of the contrast agent from normoxic regions and analysis of concentration of the agent in hypoxic regions at those time points. The 3D gradient echo images provide a 3D distribution of the regions with hypoxia and can be used to calculate the hypoxic fraction of the entire tumor volume. Future studies could also focus on evaluating the binding efficiency of GdDO3NI at various levels of hypoxia as they can be used for extracting quantitative oxygenation data. Immunohistochemical staining for multiple hypoxic markers such as HIF1 α along with pimonidazole could provide information regarding the regulation of hypoxia in tumors. Future studies could also involve the staining for tumor vasculature and angiogenesis related markers for evaluation of tumor perfusion and regulation of angiogenesis. The inclusion of ex-vivo staining for proliferation markers in tumors would be useful for evaluating the treatment effect involving HAPs. The therapy protocol for this study consisted of a single dosage of HAPs and future studies could evaluate the effect of multiple dosages (such as at

intervals of 5 days) of the agents on tumor volume and oxygenation. The dosing time interval could be decided based on the imaging protocol. The effect of combination therapies such as HAPs with cyclophosphamide (anti-angiogenic drug), cisplatin or chemo radiation could be exploited in future studies.

Experimental Challenges: The oxygenation data obtained using PISTOL technique is dependent on the distribution of neat HMDSO in the tumors. The goal is to have a uniform distribution of HMDSO droplets throughout the tumor. The physical properties of each tumor model affect the ability of the experimenter to distribute the probe uniformly. For example, a tumor with higher structural integrity and high interstitial pressure would show higher resistance which might result in difficulty in depositing the HMSO in tumor centers, while a tumor with higher edema or fluid fraction would facilitate an easier injection of the probe. Multiple droplets (~ 2 μ l in volume) should be deposited at equal distance as the needle is pulled of the tumor. HMDSO is hydrophobic thus care needs to be taken when injecting the probe so that it does not enter the blood stream and cause an embolism in the mouse. The challenges involved with GdDO3NI imaging protocol include the intravenous injection of the contrast agent. The agent should be injected steadily and slowly in order to make a successful injection. It is important to maintain the animals at a stable temperature and respiration rate to facilitate correct evaluation of tumor perfusion. The correlation of pimonidazole staining tumor sections with the corresponding MR images is dependent on maintaining the same orientation of the extracted tumor between the cryosectioning and MR image acquisition. External markers can be drawn over the tumor as the tumor is placed over the mouse bed

for imaging and those markers can be used as a guide to orient to the tumor when placing in OCT for cryosectioning.

In conclusion, the techniques discussed in this thesis have a great potential for translation into the clinic. The field of hypoxia activated therapies is still evolving and inclusion of these techniques could improve the translatability of the drugs. Our imaging techniques could be exploited for validation of predictive biomarkers in patient subpopulation as well as studying the treatment response (e.g. the modifications in hypoxic fraction). Personalized medicine is an emerging paradigm and these techniques have the potential in facilitating development of personalized therapeutic protocol by detecting the hypoxic biomarkers at various stages of treatment course. The incorporation of these techniques in routine examination of hypoxia behavior of the tumor could also shed more light on the role of hypoxia in treatment outcome and disease progression.

REFERENCES

- [1] R. L. Siegel, K. D. Miller, and A. Jemal, "Cancer statistics, 2017," *CA Cancer J Clin*, vol. 67, pp. 7-30, Jan 2017.
- [2] R. K. Jain, "Transport of molecules, particles, and cells in solid tumors," *Annu Rev Biomed Eng*, vol. 1, pp. 241-63, 1999.
- [3] D. Hanahan and L. M. Coussens, "Accessories to the crime: Functions of cells recruited to the tumor microenvironment," *Cancer Cell*, vol. 21, pp. 309-22, Mar 20 2012.
- [4] F. R. Balkwill, M. Capasso, and T. Hagemann, "The tumor microenvironment at a glance," *J Cell Sci*, vol. 125, pp. 5591-6, Dec 01 2012.
- [5] D. Hanahan and R. A. Weinberg, "Hallmarks of cancer: The next generation," *Cell*, vol. 144, pp. 646-74, Mar 4 2011.
- [6] J. M. Brown, "Thomas antley pitts, ii, 1893-1991," *J S C Med Assoc*, vol. 94, pp. 34-5, Jan 1998.
- [7] J. M. Brown and A. J. Giaccia, "The unique physiology of solid tumors: Opportunities (and problems) for cancer therapy," *Cancer Res*, vol. 58, pp. 1408-16, Apr 1 1998.
- [8] I. P. Witz, "The tumor microenvironment: The making of a paradigm," *Cancer Microenviron*, vol. 2 Suppl 1, pp. 9-17, Sep 2009.
- [9] T. L. Whiteside, "The tumor microenvironment and its role in promoting tumor growth," *Oncogene*, vol. 27, pp. 5904-12, Oct 06 2008.
- [10] M. Hockel and P. Vaupel, "Tumor hypoxia: Definitions and current clinical, biologic, and molecular aspects," *J Natl Cancer Inst*, vol. 93, pp. 266-76, Feb 21 2001.
- [11] J. L. Tatum, G. J. Kelloff, R. J. Gillies, J. M. Arbeit, J. M. Brown, K. S. Chao, J. D. Chapman, W. C. Eckelman, A. W. Fyles, A. J. Giaccia, R. P. Hill, C. J. Koch, M. C. Krishna, K. A. Krohn, J. S. Lewis, R. P. Mason, G. Melillo, A. R. Padhani, G. Powis, J. G. Rajendran, R. Reba, S. P. Robinson, G. L. Semenza, H. M. Swartz, P. Vaupel, D. Yang, B. Croft, J. Hoffman, G. Liu, H. Stone, and D. Sullivan, "Hypoxia: Importance in tumor biology, noninvasive measurement by imaging, and value of its measurement in the management of cancer therapy," *Int J Radiat Biol*, vol. 82, pp. 699-757, Oct 2006.

- [12] R. M. Bremnes, T. Donnem, S. Al-Saad, K. Al-Shibli, S. Andersen, R. Sirera, C. Camps, I. Marinez, and L. T. Busund, "The role of tumor stroma in cancer progression and prognosis: Emphasis on carcinoma-associated fibroblasts and non-small cell lung cancer," *J Thorac Oncol*, vol. 6, pp. 209-17, Jan 2011.
- [13] R. M. Bremnes, K. Al-Shibli, T. Donnem, R. Sirera, S. Al-Saad, S. Andersen, H. Stenvold, C. Camps, and L. T. Busund, "The role of tumor-infiltrating immune cells and chronic inflammation at the tumor site on cancer development, progression, and prognosis: Emphasis on non-small cell lung cancer," *J Thorac Oncol*, vol. 6, pp. 824-33, Apr 2011.
- [14] O. De Wever and M. Mareel, "Role of tissue stroma in cancer cell invasion," *J Pathol*, vol. 200, pp. 429-47, Jul 2003.
- [15] K. M. Bussard, L. Mutkus, K. Stumpf, C. Gomez-Manzano, and F. C. Marini, "Tumor-associated stromal cells as key contributors to the tumor microenvironment," *Breast Cancer Res*, vol. 18, p. 84, Aug 11 2016.
- [16] A. Cretu and P. C. Brooks, "Impact of the non-cellular tumor microenvironment on metastasis: Potential therapeutic and imaging opportunities," *J Cell Physiol*, vol. 213, pp. 391-402, Nov 2007.
- [17] L. Fass, "Imaging and cancer: A review," *Mol Oncol*, vol. 2, pp. 115-52, Aug 2008.
- [18] W. R. Wilson and M. P. Hay, "Targeting hypoxia in cancer therapy," *Nat Rev Cancer*, vol. 11, pp. 393-410, Jun 2011.
- [19] E. Blanco, A. Hsiao, A. P. Mann, M. G. Landry, F. Meric-Bernstam, and M. Ferrari, "Nanomedicine in cancer therapy: Innovative trends and prospects," *Cancer Sci*, vol. 102, pp. 1247-52, Jul 2011.
- [20] A. Hellebust and R. Richards-Kortum, "Advances in molecular imaging: Targeted optical contrast agents for cancer diagnostics," *Nanomedicine (Lond)*, vol. 7, pp. 429-45, Mar 2012.
- [21] D. W. Siemann and M. R. Horsman, "Modulation of the tumor vasculature and oxygenation to improve therapy," *Pharmacol Ther*, vol. 153, pp. 107-24, Sep 2015.
- [22] R. H. Farnsworth, M. Lackmann, M. G. Achen, and S. A. Stacker, "Vascular remodeling in cancer," *Oncogene*, vol. 33, pp. 3496-505, Jul 03 2014.
- [23] D. W. Siemann, "The unique characteristics of tumor vasculature and preclinical evidence for its selective disruption by tumor-vascular disrupting agents," *Cancer Treat Rev*, vol. 37, pp. 63-74, Feb 2011.

- [24] C. Michiels, C. Tellier, and O. Feron, "Cycling hypoxia: A key feature of the tumor microenvironment," *Biochim Biophys Acta*, vol. 1866, pp. 76-86, Aug 2016.
- [25] R. H. Thomlinson and L. H. Gray, "The histological structure of some human lung cancers and the possible implications for radiotherapy," *Br J Cancer*, vol. 9, pp. 539-49, Dec 1955.
- [26] J. M. Brown, "Evidence for acutely hypoxic cells in mouse tumours, and a possible mechanism of reoxygenation," *Br J Radiol*, vol. 52, pp. 650-6, Aug 1979.
- [27] P. N. Span and J. Bussink, "Biology of hypoxia," *Semin Nucl Med*, vol. 45, pp. 101-9, Mar 2015.
- [28] P. Vaupel and A. Mayer, "Hypoxia in tumors: Pathogenesis-related classification, characterization of hypoxia subtypes, and associated biological and clinical implications," *Adv Exp Med Biol*, vol. 812, pp. 19-24, 2014.
- [29] E. E. Graves, A. Maity, and Q. T. Le, "The tumor microenvironment in non-small-cell lung cancer," *Semin Radiat Oncol*, vol. 20, pp. 156-63, Jul 2010.
- [30] E. E. Graves, M. Vilalta, I. K. Cecic, J. T. Erler, P. T. Tran, D. Felsher, L. Sayles, A. Sweet-Cordero, Q. T. Le, and A. J. Giaccia, "Hypoxia in models of lung cancer: Implications for targeted therapeutics," *Clin Cancer Res*, vol. 16, pp. 4843-52, Oct 1 2010.
- [31] J. G. Foster, S. C. Wong, and T. V. Sharp, "The hypoxic tumor microenvironment: Driving the tumorigenesis of non-small-cell lung cancer," *Future Oncol*, vol. 10, pp. 2659-74, Dec 2014.
- [32] J. A. Nagy, S. H. Chang, A. M. Dvorak, and H. F. Dvorak, "Why are tumour blood vessels abnormal and why is it important to know?," *Br J Cancer*, vol. 100, pp. 865-9, Mar 24 2009.
- [33] N. Ferrara, H. P. Gerber, and J. LeCouter, "The biology of vegf and its receptors," *Nat Med*, vol. 9, pp. 669-76, Jun 2003.
- [34] P. Carmeliet and R. K. Jain, "Angiogenesis in cancer and other diseases," *Nature*, vol. 407, pp. 249-57, Sep 14 2000.
- [35] B. L. Krock, N. Skuli, and M. C. Simon, "Hypoxia-induced angiogenesis: Good and evil," *Genes Cancer*, vol. 2, pp. 1117-33, Dec 2011.
- [36] M. A. Konerding, E. Fait, and A. Gaumann, "3d microvascular architecture of pre-cancerous lesions and invasive carcinomas of the colon," *Br J Cancer*, vol. 84, pp. 1354-62, May 18 2001.

- [37] D. M. McDonald and P. L. Choyke, "Imaging of angiogenesis: From microscope to clinic," *Nat Med*, vol. 9, pp. 713-25, Jun 2003.
- [38] A. J. Leu, D. A. Berk, A. Lymboussaki, K. Alitalo, and R. K. Jain, "Absence of functional lymphatics within a murine sarcoma: A molecular and functional evaluation," *Cancer Res*, vol. 60, pp. 4324-7, Aug 15 2000.
- [39] R. T. Tong, Y. Boucher, S. V. Kozin, F. Winkler, D. J. Hicklin, and R. K. Jain, "Vascular normalization by vascular endothelial growth factor receptor 2 blockade induces a pressure gradient across the vasculature and improves drug penetration in tumors," *Cancer Res*, vol. 64, pp. 3731-6, Jun 01 2004.
- [40] G. Helmlinger, F. Yuan, M. Dellian, and R. K. Jain, "Interstitial pH and pO₂ gradients in solid tumors in vivo: High-resolution measurements reveal a lack of correlation," *Nat Med*, vol. 3, pp. 177-82, Feb 1997.
- [41] E. B. Rankin and A. J. Giaccia, "Hypoxic control of metastasis," *Science*, vol. 352, pp. 175-80, Apr 08 2016.
- [42] B. Muz, P. de la Puente, F. Azab, and A. K. Azab, "The role of hypoxia in cancer progression, angiogenesis, metastasis, and resistance to therapy," *Hypoxia (Auckl)*, vol. 3, pp. 83-92, 2015.
- [43] S. Rockwell, I. T. Dobrucki, E. Y. Kim, S. T. Marrison, and V. T. Vu, "Hypoxia and radiation therapy: Past history, ongoing research, and future promise," *Curr Mol Med*, vol. 9, pp. 442-58, May 2009.
- [44] J. C. Walsh, A. Lebedev, E. Aten, K. Madsen, L. Marciano, and H. C. Kolb, "The clinical importance of assessing tumor hypoxia: Relationship of tumor hypoxia to prognosis and therapeutic opportunities," *Antioxid Redox Signal*, vol. 21, pp. 1516-54, Oct 01 2014.
- [45] A. M. Shannon, D. J. Bouchier-Hayes, C. M. Condrón, and D. Toomey, "Tumour hypoxia, chemotherapeutic resistance and hypoxia-related therapies," *Cancer Treat Rev*, vol. 29, pp. 297-307, Aug 2003.
- [46] E. M. Hammond, M. C. Asselin, D. Forster, J. P. O'Connor, J. M. Senra, and K. J. Williams, "The meaning, measurement and modification of hypoxia in the laboratory and the clinic," *Clin Oncol (R Coll Radiol)*, vol. 26, pp. 277-88, May 2014.
- [47] K. Ruan, G. Song, and G. Ouyang, "Role of hypoxia in the hallmarks of human cancer," *J Cell Biochem*, vol. 107, pp. 1053-62, Aug 15 2009.
- [48] A. Patel and S. Sant, "Hypoxic tumor microenvironment: Opportunities to develop targeted therapies," *Biotechnol Adv*, vol. 34, pp. 803-12, Sep-Oct 2016.

- [49] D. M. Brizel, G. S. Sibley, L. R. Prosnitz, R. L. Scher, and M. W. Dewhirst, "Tumor hypoxia adversely affects the prognosis of carcinoma of the head and neck," *Int J Radiat Oncol Biol Phys*, vol. 38, pp. 285-9, May 01 1997.
- [50] A. L. Harris, "Hypoxia--a key regulatory factor in tumour growth," *Nat Rev Cancer*, vol. 2, pp. 38-47, Jan 2002.
- [51] J. M. Brown, "The hypoxic cell: A target for selective cancer therapy--eighteenth bruce f. Cain memorial award lecture," *Cancer Res*, vol. 59, pp. 5863-70, Dec 1 1999.
- [52] G. Melillo, "Targeting hypoxia cell signaling for cancer therapy," *Cancer Metastasis Rev*, vol. 26, pp. 341-52, Jun 2007.
- [53] C. Wigerup, S. Pahlman, and D. Bexell, "Therapeutic targeting of hypoxia and hypoxia-inducible factors in cancer," *Pharmacol Ther*, vol. 164, pp. 152-69, Aug 2016.
- [54] R. M. Phillips, "Targeting the hypoxic fraction of tumours using hypoxia-activated prodrugs," *Cancer Chemother Pharmacol*, vol. 77, pp. 441-57, Mar 2016.
- [55] F. W. Hunter, B. G. Wouters, and W. R. Wilson, "Hypoxia-activated prodrugs: Paths forward in the era of personalised medicine," *Br J Cancer*, vol. 114, pp. 1071-7, May 10 2016.
- [56] W. A. Denny, "Hypoxia-activated prodrugs in cancer therapy: Progress to the clinic," *Future Oncol*, vol. 6, pp. 419-28, Mar 2010.
- [57] J. X. Duan, H. Jiao, J. Kaizerman, T. Stanton, J. W. Evans, L. Lan, G. Lorente, M. Banica, D. Jung, J. Wang, H. Ma, X. Li, Z. Yang, R. M. Hoffman, W. S. Ammons, C. P. Hart, and M. Matteucci, "Potent and highly selective hypoxia-activated achiral phosphoramidate mustards as anticancer drugs," *J Med Chem*, vol. 51, pp. 2412-20, Apr 24 2008.
- [58] M. Baumann, M. Krause, and R. Hill, "Exploring the role of cancer stem cells in radioresistance," *Nat Rev Cancer*, vol. 8, pp. 545-54, Jul 2008.
- [59] C. T. Jordan, M. L. Guzman, and M. Noble, "Cancer stem cells," *N Engl J Med*, vol. 355, pp. 1253-61, Sep 21 2006.
- [60] P. B. Gupta, C. L. Chaffer, and R. A. Weinberg, "Cancer stem cells: Mirage or reality?," *Nat Med*, vol. 15, pp. 1010-2, Sep 2009.
- [61] R. Gupta, P. Vyas, and T. Enver, "Molecular targeting of cancer stem cells," *Cell Stem Cell*, vol. 5, pp. 125-6, Aug 07 2009.

- [62] R. Blum, R. Gupta, P. E. Burger, C. S. Ontiveros, S. N. Salm, X. Xiong, A. Kamb, H. Wesche, L. Marshall, G. Cutler, X. Wang, J. Zavadil, D. Moscatelli, and E. L. Wilson, "Molecular signatures of prostate stem cells reveal novel signaling pathways and provide insights into prostate cancer," *PLoS One*, vol. 4, p. e5722, May 29 2009.
- [63] F. Li, B. Tiede, J. Massague, and Y. Kang, "Beyond tumorigenesis: Cancer stem cells in metastasis," *Cell Res*, vol. 17, pp. 3-14, Jan 2007.
- [64] Y. Shiozawa, B. Nie, K. J. Pienta, T. M. Morgan, and R. S. Taichman, "Cancer stem cells and their role in metastasis," *Pharmacol Ther*, vol. 138, pp. 285-93, May 2013.
- [65] J. Mathieu, Z. Zhang, W. Zhou, A. J. Wang, J. M. Heddleston, C. M. Pinna, A. Hubaud, B. Stadler, M. Choi, M. Bar, M. Tewari, A. Liu, R. Vessella, R. Rostomily, D. Born, M. Horwitz, C. Ware, C. A. Blau, M. A. Cleary, J. N. Rich, and H. Ruohola-Baker, "Hif induces human embryonic stem cell markers in cancer cells," *Cancer Res*, vol. 71, pp. 4640-52, Jul 01 2011.
- [66] A. M. McCord, M. Jamal, U. T. Shankavaram, F. F. Lang, K. Camphausen, and P. J. Tofilon, "Physiologic oxygen concentration enhances the stem-like properties of cd133+ human glioblastoma cells in vitro," *Mol Cancer Res*, vol. 7, pp. 489-97, Apr 2009.
- [67] Z. Yun and Q. Lin, "Hypoxia and regulation of cancer cell stemness," *Adv Exp Med Biol*, vol. 772, pp. 41-53, 2014.
- [68] S. W. Crowder, D. A. Balikov, Y. S. Hwang, and H. J. Sung, "Cancer stem cells under hypoxia as a chemoresistance factor in breast and brain," *Curr Pathobiol Rep*, vol. 2, pp. 33-40, Mar 2014.
- [69] E. K. Rofstad and K. Maseide, "Radiobiological and immunohistochemical assessment of hypoxia in human melanoma xenografts: Acute and chronic hypoxia in individual tumours," *Int J Radiat Biol*, vol. 75, pp. 1377-93, Nov 1999.
- [70] S. J. Diaz-Cano, "Tumor heterogeneity: Mechanisms and bases for a reliable application of molecular marker design," *Int J Mol Sci*, vol. 13, pp. 1951-2011, 2012.
- [71] N. C. Dhani, S. Serra, M. Pintilie, J. Schwock, J. Xu, S. Gallinger, R. P. Hill, and D. W. Hedley, "Analysis of the intra- and intertumoral heterogeneity of hypoxia in pancreatic cancer patients receiving the nitroimidazole tracer pimonidazole," *Br J Cancer*, vol. 113, pp. 864-71, Sep 15 2015.

- [72] V. V. Iakovlev, M. Pintilie, A. Morrison, A. W. Fyles, R. P. Hill, and D. W. Hedley, "Effect of distributional heterogeneity on the analysis of tumor hypoxia based on carbonic anhydrase ix," *Lab Invest*, vol. 87, pp. 1206-17, Dec 2007.
- [73] P. Vaupel, A. Mayer, and M. Hockel, "Tumor hypoxia and malignant progression," *Methods Enzymol*, vol. 381, pp. 335-54, 2004.
- [74] J. K. Mohindra and A. M. Rauth, "Increased cell killing by metronidazole and nitrofurazone of hypoxic compared to aerobic mammalian cells," *Cancer Res*, vol. 36, pp. 930-6, Mar 1976.
- [75] W. A. Denny, W. R. Wilson, and M. P. Hay, "Recent developments in the design of bioreductive drugs," *Br J Cancer Suppl*, vol. 27, pp. S32-8, Jul 1996.
- [76] A. V. Patterson, D. M. Ferry, S. J. Edmunds, Y. Gu, R. S. Singleton, K. Patel, S. M. Pullen, K. O. Hicks, S. P. Syddall, G. J. Atwell, S. Yang, W. A. Denny, and W. R. Wilson, "Mechanism of action and preclinical antitumor activity of the novel hypoxia-activated DNA cross-linking agent pr-104," *Clin Cancer Res*, vol. 13, pp. 3922-32, Jul 01 2007.
- [77] C. R. Nishida and P. R. Ortiz de Montellano, "Reductive heme-dependent activation of the n-oxide prodrug aq4n by nitric oxide synthase," *J Med Chem*, vol. 51, pp. 5118-20, Aug 28 2008.
- [78] E. A. Oostveen and W. N. Speckamp, "Mitomycin analogs .1. Indoloquinones as (potential) bisalkylating agents," *Tetrahedron*, vol. 43, pp. 255-262, 1987.
- [79] Q. Liu, J. D. Sun, J. Wang, D. Ahluwalia, A. F. Baker, L. D. Cranmer, D. Ferraro, Y. Wang, J. X. Duan, W. S. Ammons, J. G. Curd, M. D. Matteucci, and C. P. Hart, "Th-302, a hypoxia-activated prodrug with broad in vivo preclinical combination therapy efficacy: Optimization of dosing regimens and schedules," *Cancer Chemother Pharmacol*, vol. 69, pp. 1487-98, Jun 2012.
- [80] A. V. Patterson, S. Silva, C. Guise, M. Abbattista, M. Bull, H. L. Hsu, C. Hart, J. Sun, A. Grey, A. Ashoorzadeh, R. Anderson, and J. B. Smaill, "The hypoxia-activated egfr-tni th-4000 overcomes erlotinib-resistance in preclinical nslc models at plasma levels achieved in a phase 1 clinical trial," *Cancer Research*, vol. 75, Aug 1 2015.
- [81] A. V. Patterson, S. Silva, C. Guise, M. Bull, M. Abbattista, A. Hsu, J. D. Sun, C. P. Hart, T. E. Pearce, and J. B. Smaill, "Th-4000, a hypoxia-activated egfr/her2 inhibitor to treat egfr-tni resistant t790m-negative nslc," *Journal of Clinical Oncology*, vol. 33, May 20 2015.

- [82] E. M. Zeman, J. M. Brown, M. J. Lemmon, V. K. Hirst, and W. W. Lee, "Sr-4233: A new bioreductive agent with high selective toxicity for hypoxic mammalian cells," *Int J Radiat Oncol Biol Phys*, vol. 12, pp. 1239-42, Jul 1986.
- [83] J. W. Evans, K. Yudoh, Y. M. Delahoussaye, and J. M. Brown, "Tirapazamine is metabolized to its DNA-damaging radical by intranuclear enzymes," *Cancer Res*, vol. 58, pp. 2098-101, May 15 1998.
- [84] D. Rischin, L. J. Peters, B. O'Sullivan, J. Giralt, R. Fisher, K. Yuen, A. Trotti, J. Bernier, J. Bourhis, J. Ringash, M. Henke, and L. Kenny, "Tirapazamine, cisplatin, and radiation versus cisplatin and radiation for advanced squamous cell carcinoma of the head and neck (trog 02.02, headstart): A phase iii trial of the trans-tasman radiation oncology group," *J Clin Oncol*, vol. 28, pp. 2989-95, Jun 20 2010.
- [85] W. A. Denny and W. R. Wilson, "Tirapazamine: A bioreductive anticancer drug that exploits tumour hypoxia," *Expert Opin Investig Drugs*, vol. 9, pp. 2889-901, Dec 2000.
- [86] B. G. Wouters, L. H. Wang, and J. M. Brown, "Tirapazamine: A new drug producing tumor specific enhancement of platinum-based chemotherapy in non-small-cell lung cancer," *Ann Oncol*, vol. 10 Suppl 5, pp. S29-33, 1999.
- [87] L. Marcu and I. Olver, "Tirapazamine: From bench to clinical trials," *Curr Clin Pharmacol*, vol. 1, pp. 71-9, Jan 2006.
- [88] D. R. Gandara, P. N. Lara, Jr., Z. Goldberg, Q. T. Le, P. C. Mack, D. H. Lau, and P. H. Gumerlock, "Tirapazamine: Prototype for a novel class of therapeutic agents targeting tumor hypoxia," *Semin Oncol*, vol. 29, pp. 102-9, Feb 2002.
- [89] S. Masunaga, Y. Liu, Y. Sakurai, H. Tanaka, M. Suzuki, N. Kondo, A. Maruhashi, and K. Ono, "Usefulness of combined treatment with continuous administration of tirapazamine and mild temperature hyperthermia in gamma-ray irradiation in terms of local tumour response and lung metastatic potential," *Int J Hyperthermia*, vol. 28, pp. 636-44, 2012.
- [90] J. Del Rowe, C. Scott, M. Werner-Wasik, J. P. Bahary, W. J. Curran, R. C. Urtasun, and B. Fisher, "Single-arm, open-label phase ii study of intravenously administered tirapazamine and radiation therapy for glioblastoma multiforme," *J Clin Oncol*, vol. 18, pp. 1254-9, Mar 2000.
- [91] J. B. P. Smaill, A.V., Lu, G.L., Lee, H.H., Ashoorzadeh, A., Anderson, R.F. et al., "Kinase inhibitors, prodrug forms thereof and their use in cancer therapy.," Patent WO/2011/028135, 2011.

- [92] H. van Crujisen, G. Giaccone, and K. Hoekman, "Epidermal growth factor receptor and angiogenesis: Opportunities for combined anticancer strategies," *Int J Cancer*, vol. 117, pp. 883-8, Dec 20 2005.
- [93] R. M. Phillips, H. R. Hendriks, G. J. Peters, E. Pharmacology, and G. Molecular Mechanism, "Eo9 (apaziquone): From the clinic to the laboratory and back again," *Br J Pharmacol*, vol. 168, pp. 11-8, Jan 2013.
- [94] J. X. Duan, H. Jiao, J. Kaizerman, T. Stanton, J. W. Evans, L. Lan, G. Lorente, M. Banica, D. Jung, J. W. Wang, H. Y. Ma, X. M. Li, Z. J. Yang, R. M. Hoffman, W. S. Ammons, C. P. Hart, and M. Matteucci, "Potent and highly selective hypoxia-activated achiral phosphoramidate mustards as anticancer drugs," *Journal of Medicinal Chemistry*, vol. 51, pp. 2412-2420, Apr 24 2008.
- [95] J. D. Sun, Q. Liu, J. Wang, D. Ahluwalia, D. Ferraro, Y. Wang, J. X. Duan, W. S. Ammons, J. G. Curd, M. D. Matteucci, and C. P. Hart, "Selective tumor hypoxia targeting by hypoxia-activated prodrug th-302 inhibits tumor growth in preclinical models of cancer," *Clin Cancer Res*, vol. 18, pp. 758-70, Feb 01 2012.
- [96] J. Benito, M. S. Ramirez, N. Z. Millward, J. Velez, K. G. Harutyunyan, H. Lu, Y. X. Shi, P. Matre, R. Jacamo, H. Ma, S. Konoplev, T. McQueen, A. Volgin, M. Protopopova, H. Mu, J. Lee, P. K. Bhattacharya, J. R. Marszalek, R. E. Davis, J. A. Bankson, J. E. Cortes, C. P. Hart, M. Andreeff, and M. Konopleva, "Hypoxia-activated prodrug th-302 targets hypoxic bone marrow niches in preclinical leukemia models," *Clin Cancer Res*, vol. 22, pp. 1687-98, Apr 01 2016.
- [97] F. Meng, J. W. Evans, D. Bhupathi, M. Banica, L. Lan, G. Lorente, J. X. Duan, X. Cai, A. M. Mowday, C. P. Guise, A. Maroz, R. F. Anderson, A. V. Patterson, G. C. Stachelek, P. M. Glazer, M. D. Matteucci, and C. P. Hart, "Molecular and cellular pharmacology of the hypoxia-activated prodrug th-302," *Mol Cancer Ther*, vol. 11, pp. 740-51, Mar 2012.
- [98] M. R. Abbattista, S. M. Jamieson, Y. Gu, J. E. Nickel, S. M. Pullen, A. V. Patterson, W. R. Wilson, and C. P. Guise, "Pre-clinical activity of pr-104 as monotherapy and in combination with sorafenib in hepatocellular carcinoma," *Cancer Biol Ther*, vol. 16, pp. 610-22, 2015.
- [99] M. Konopleva, P. F. Thall, C. A. Yi, G. Borthakur, A. Coveler, C. Bueso-Ramos, J. Benito, S. Konoplev, Y. Gu, F. Ravandi, E. Jabbour, S. Faderl, D. Thomas, J. Cortes, T. Kadia, S. Kornblau, N. Daver, N. Pemmaraju, H. Q. Nguyen, J. Feliu, H. Lu, C. Wei, W. R. Wilson, T. J. Melink, J. C. Gutheil, M. Andreeff, E. H. Estey, and H. Kantarjian, "Phase i/ii study of the hypoxia-activated prodrug pr104 in refractory/relapsed acute myeloid leukemia and acute lymphoblastic leukemia," *Haematologica*, vol. 100, pp. 927-34, Jul 2015.

- [100] Z.-P. Liang, P. C. Lauterbur, and IEEE Engineering in Medicine and Biology Society., *Principles of magnetic resonance imaging : A signal processing perspective*. Bellingham, Wash. New York: SPIE Optical Engineering Press ; IEEE Press, 2000.
- [101] S. W. Atlas and S. W. Atlas, *Magnetic resonance imaging of the brain and spine*, 3rd ed. Philadelphia: Lippincott Williams & Wilkins, 2002.
- [102] R. Damadian, "Tumor detection by nuclear magnetic resonance," *Science*, vol. 171, pp. 1151-3, Mar 19 1971.
- [103] J. C. Gore, H. C. Manning, C. C. Quarles, K. W. Waddell, and T. E. Yankeelov, "Magnetic resonance in the era of molecular imaging of cancer," *Magn Reson Imaging*, vol. 29, pp. 587-600, Jun 2011.
- [104] E. M. Haacke, *Magnetic resonance imaging : Physical principles and sequence design*. New York: Wiley, 1999.
- [105] R. B. Lauffer, "Paramagnetic metal-complexes as water proton relaxation agents for nmr imaging - theory and design," *Chemical Reviews*, vol. 87, pp. 901-927, Oct 1987.
- [106] S. Aime, S. G. Crich, E. Gianolio, G. B. Giovenzana, L. Tei, and E. Terreno, "High sensitivity lanthanide(iii) based probes for mr-medical imaging," *Coordination Chemistry Reviews*, vol. 250, pp. 1562-1579, Jun 2006.
- [107] P. Caravan, "Strategies for increasing the sensitivity of gadolinium based mri contrast agents," *Chem Soc Rev*, vol. 35, pp. 512-23, Jun 2006.
- [108] E. J. Werner, A. Datta, C. J. Jocher, and K. N. Raymond, "High-relaxivity mri contrast agents: Where coordination chemistry meets medical imaging," *Angew Chem Int Ed Engl*, vol. 47, pp. 8568-80, 2008.
- [109] K. Glunde, D. Artemov, M. F. Penet, M. A. Jacobs, and Z. M. Bhujwala, "Magnetic resonance spectroscopy in metabolic and molecular imaging and diagnosis of cancer," *Chem Rev*, vol. 110, pp. 3043-59, May 12 2010.
- [110] A. J. Villaraza, A. Bumb, and M. W. Brechbiel, "Macromolecules, dendrimers, and nanomaterials in magnetic resonance imaging: The interplay between size, function, and pharmacokinetics," *Chem Rev*, vol. 110, pp. 2921-59, May 12 2010.
- [111] N. Kamaly, A. D. Miller, and J. D. Bell, "Chemistry of tumour targeted t1 based mri contrast agents," *Curr Top Med Chem*, vol. 10, pp. 1158-83, 2010.

- [112] M. Rohrer, H. Bauer, J. Mintorovitch, M. Requardt, and H. J. Weinmann, "Comparison of magnetic properties of mri contrast media solutions at different magnetic field strengths," *Invest Radiol*, vol. 40, pp. 715-24, Nov 2005.
- [113] P. Caravan, C. T. Farrar, L. Frullano, and R. Uppal, "Influence of molecular parameters and increasing magnetic field strength on relaxivity of gadolinium- and manganese-based t1 contrast agents," *Contrast Media Mol Imaging*, vol. 4, pp. 89-100, Mar-Apr 2009.
- [114] R. P. Mason, D. Zhao, J. Pacheco-Torres, W. Cui, V. D. Kodibagkar, P. K. Gulaka, G. Hao, P. Thorpe, E. W. Hahn, and P. Peschke, "Multimodality imaging of hypoxia in preclinical settings," *Q J Nucl Med Mol Imaging*, vol. 54, pp. 259-80, Jun 2010.
- [115] X. Sun, G. Niu, N. Chan, B. Shen, and X. Chen, "Tumor hypoxia imaging," *Mol Imaging Biol*, vol. 13, pp. 399-410, Jun 2011.
- [116] K. A. Yeh, S. Biade, R. M. Lanciano, D. Q. Brown, M. C. Fenning, J. S. Babb, G. E. Hanks, and D. C. Chapman, "Polarographic needle electrode measurements of oxygen in rat prostate carcinomas: Accuracy and reproducibility," *Int J Radiat Oncol Biol Phys*, vol. 33, pp. 111-8, Aug 30 1995.
- [117] J. R. Griffiths and S. P. Robinson, "The oxylyte: A fibre-optic oxygen sensor," *Br J Radiol*, vol. 72, pp. 627-30, Jul 1999.
- [118] S. M. Evans, S. Hahn, D. R. Pook, W. T. Jenkins, A. A. Chalian, P. Zhang, C. Stevens, R. Weber, G. Weinstein, I. Benjamin, N. Mirza, M. Morgan, S. Rubin, W. G. McKenna, E. M. Lord, and C. J. Koch, "Detection of hypoxia in human squamous cell carcinoma by ef5 binding," *Cancer Res*, vol. 60, pp. 2018-24, Apr 01 2000.
- [119] R. J. Young and A. Moller, "Immunohistochemical detection of tumour hypoxia," *Methods Mol Biol*, vol. 611, pp. 151-9, 2010.
- [120] S. E. Rademakers, J. Lok, A. J. van der Kogel, J. Bussink, and J. H. Kaanders, "Metabolic markers in relation to hypoxia; staining patterns and colocalization of pimonidazole, hif-1alpha, caix, ldh-5, glut-1, mct1 and mct4," *BMC Cancer*, vol. 11, p. 167, May 12 2011.
- [121] M. A. Varia, D. P. Calkins-Adams, L. H. Rinker, A. S. Kennedy, D. B. Novotny, W. C. Fowler, Jr., and J. A. Raleigh, "Pimonidazole: A novel hypoxia marker for complementary study of tumor hypoxia and cell proliferation in cervical carcinoma," *Gynecol Oncol*, vol. 71, pp. 270-7, Nov 1998.
- [122] J. M. Murkin and M. Arango, "Near-infrared spectroscopy as an index of brain and tissue oxygenation," *Br J Anaesth*, vol. 103 Suppl 1, pp. i3-13, Dec 2009.

- [123] M. J. Gandolfo, A. H. Kyle, and A. I. Minchinton, "Tissue discs: A 3d model for assessing modulation of tissue oxygenation," *Adv Exp Med Biol*, vol. 876, pp. 169-75, 2016.
- [124] J. S. Lewis, D. W. McCarthy, T. J. McCarthy, Y. Fujibayashi, and M. J. Welch, "Evaluation of ^{64}Cu -atasm in vitro and in vivo in a hypoxic tumor model," *J Nucl Med*, vol. 40, pp. 177-83, Jan 1999.
- [125] L. Li, J. Yu, L. Xing, K. Ma, H. Zhu, H. Guo, X. Sun, J. Li, G. Yang, W. Li, J. Yue, and B. Li, "Serial hypoxia imaging with $^{99\text{mTc}}$ -hl91 spect to predict radiotherapy response in nonsmall cell lung cancer," *Am J Clin Oncol*, vol. 29, pp. 628-33, Dec 2006.
- [126] M. Tamura, O. Hazeki, S. Nioka, and B. Chance, "In vivo study of tissue oxygen metabolism using optical and nuclear magnetic resonance spectroscopies," *Annu Rev Physiol*, vol. 51, pp. 813-34, 1989.
- [127] G. Reischl, D. S. Dorow, C. Cullinane, A. Katsifis, P. Roselt, D. Binns, and R. J. Hicks, "Imaging of tumor hypoxia with ^{124}I iaza in comparison with $^{18\text{F}}$ fmiso and $^{18\text{F}}$ faza--first small animal pet results," *J Pharm Pharm Sci*, vol. 10, pp. 203-11, 2007.
- [128] J. C. Asquith, M. E. Watts, K. Patel, C. E. Smithen, and G. E. Adams, "Electron affinic sensitization. V. Radiosensitization of hypoxic bacteria and mammalian cells in vitro by some nitroimidazoles and nitropyrazoles," *Radiat Res*, vol. 60, pp. 108-18, Oct 1974.
- [129] D. I. Edwards, "Mechanisms of selective toxicity of metronidazole and other nitroimidazole drugs," *Br J Vener Dis*, vol. 56, pp. 285-90, Oct 1980.
- [130] H. Monney, J. Parrick, and R. G. Wallace, "Nitroimidazole radiosensitizers: Approaches to their chemical synthesis," *Pharmacol Ther*, vol. 14, pp. 197-216, 1981.
- [131] J. D. Chapman, J. Lee, and B. E. Meeker, "Keynote address: Cellular reduction of nitroimidazole drugs: Potential for selective chemotherapy and diagnosis of hypoxic cells," *Int J Radiat Oncol Biol Phys*, vol. 16, pp. 911-7, Apr 1989.
- [132] E. J. Postema, A. J. McEwan, T. A. Riauka, P. Kumar, D. A. Richmond, D. N. Abrams, and L. I. Wiebe, "Initial results of hypoxia imaging using 1-alpha-d: -(5-deoxy-5-[$^{18\text{F}}$ -fluoroarabinofuranosyl)-2-nitroimidazole ($^{18\text{F}}$ -faza)," *Eur J Nucl Med Mol Imaging*, vol. 36, pp. 1565-73, Oct 2009.
- [133] J. G. Rajendran, D. A. Mankoff, F. O'Sullivan, L. M. Peterson, D. L. Schwartz, E. U. Conrad, A. M. Spence, M. Muzi, D. G. Farwell, and K. A. Krohn, "Hypoxia and glucose metabolism in malignant tumors: Evaluation by

- [18f]fluoromisonidazole and [18f]fluorodeoxyglucose positron emission tomography imaging," *Clin Cancer Res*, vol. 10, pp. 2245-52, Apr 01 2004.
- [134] J. G. Rajendran, D. C. Wilson, E. U. Conrad, L. M. Peterson, J. D. Bruckner, J. S. Rasey, L. K. Chin, P. D. Hofstrand, J. R. Grierson, J. F. Eary, and K. A. Krohn, "[18f]fmiso and [18f]fdg pet imaging in soft tissue sarcomas: Correlation of hypoxia, metabolism and vegf expression," *Eur J Nucl Med Mol Imaging*, vol. 30, pp. 695-704, May 2003.
- [135] C. Baudelet and B. Gallez, "How does blood oxygen level-dependent (bold) contrast correlate with oxygen partial pressure (po2) inside tumors?," *Magn Reson Med*, vol. 48, pp. 980-6, Dec 2002.
- [136] Y. Ding, R. P. Mason, R. W. McColl, Q. Yuan, R. R. Hallac, R. D. Sims, and P. T. Weatherall, "Simultaneous measurement of tissue oxygen level-dependent (told) and blood oxygenation level-dependent (bold) effects in abdominal tissue oxygenation level studies," *J Magn Reson Imaging*, vol. 38, pp. 1230-6, Nov 2013.
- [137] J. P. O'Connor, J. K. Boulton, Y. Jamin, M. Babur, K. G. Finegan, K. J. Williams, R. A. Little, A. Jackson, G. J. Parker, A. R. Reynolds, J. C. Waterton, and S. P. Robinson, "Oxygen-enhanced mri accurately identifies, quantifies, and maps tumor hypoxia in preclinical cancer models," *Cancer Res*, vol. 76, pp. 787-95, Feb 15 2016.
- [138] R. Ahmad and P. Kuppusamy, "Theory, instrumentation, and applications of electron paramagnetic resonance oximetry," *Chem Rev*, vol. 110, pp. 3212-36, May 12 2010.
- [139] R. P. Mason, W. Rodbumrung, and P. P. Antich, "Hexafluorobenzene: A sensitive 19f nmr indicator of tumor oxygenation," *NMR Biomed*, vol. 9, pp. 125-34, May 1996.
- [140] V. D. Kodibagkar, W. Cui, M. E. Merritt, and R. P. Mason, "Novel 1h nmr approach to quantitative tissue oximetry using hexamethyldisiloxane," *Magn Reson Med*, vol. 55, pp. 743-8, Apr 2006.
- [141] V. D. Kodibagkar, X. Wang, J. Pacheco-Torres, P. Gulaka, and R. P. Mason, "Proton imaging of siloxanes to map tissue oxygenation levels (pistol): A tool for quantitative tissue oximetry," *NMR Biomed*, vol. 21, pp. 899-907, Oct 2008.
- [142] H. A. Al-Hallaq, J. N. River, M. Zamora, H. Oikawa, and G. S. Karczmar, "Correlation of magnetic resonance and oxygen microelectrode measurements of carbogen-induced changes in tumor oxygenation," *Int J Radiat Oncol Biol Phys*, vol. 41, pp. 151-9, Apr 01 1998.

- [143] M. W. Dewhirst and S. R. Birer, "Oxygen-enhanced mri is a major advance in tumor hypoxia imaging," *Cancer Res*, vol. 76, pp. 769-72, Feb 15 2016.
- [144] H. M. Swartz, H. Hou, N. Khan, L. A. Jarvis, E. Y. Chen, B. B. Williams, and P. Kuppasamy, "Advances in probes and methods for clinical epr oximetry," *Adv Exp Med Biol*, vol. 812, pp. 73-9, 2014.
- [145] B. J. Dardzinski and C. H. Sotak, "Rapid tissue oxygen tension mapping using 19f inversion-recovery echo-planar imaging of perfluoro-15-crown-5-ether," *Magn Reson Med*, vol. 32, pp. 88-97, Jul 1994.
- [146] P. K. Gulaka, U. Rastogi, M. A. McKay, X. Wang, R. P. Mason, and V. D. Kodibagkar, "Hexamethyldisiloxane-based nanoprobe for (1) h mri oximetry," *NMR Biomed*, vol. 24, pp. 1226-34, Dec 2011.
- [147] F. A. Rojas-Quijano, G. Tircso, E. Tircsone Benyo, Z. Baranyai, H. Tran Hoang, F. K. Kalman, P. K. Gulaka, V. D. Kodibagkar, S. Aime, Z. Kovacs, and A. D. Sherry, "Synthesis and characterization of a hypoxia-sensitive mri probe," *Chemistry*, vol. 18, pp. 9669-76, Jul 27 2012.
- [148] G. L. Kedderis and G. T. Miwa, "The metabolic activation of nitroheterocyclic therapeutic agents," *Drug Metab Rev*, vol. 19, pp. 33-62, 1988.
- [149] P. W. Sheldon, J. L. Foster, and J. F. Fowler, "Radiosensitization of c3h mouse mammary tumours by a 2-nitroimidazole drug," *Br J Cancer*, vol. 30, pp. 560-5, Dec 1974.
- [150] J. M. Brown, "Selective radiosensitization of the hypoxic cells of mouse tumors with the nitroimidazoles metronidazole and ro 7-0582," *Radiat Res*, vol. 64, pp. 633-47, Dec 1975.
- [151] P. K. Gulaka, F. Rojas-Quijano, Z. Kovacs, R. P. Mason, A. D. Sherry, and V. D. Kodibagkar, "Gddo3ni, a nitroimidazole-based t1 mri contrast agent for imaging tumor hypoxia in vivo," *J Biol Inorg Chem*, vol. 19, pp. 271-9, Feb 2014.
- [152] R. T. P. Gulaka, R. P. Mason, D. Sherry and V. D. Kodibagkar, "Imaging modulation of tumor hypoxia in vivo using a nitroimidazole based t1 mr contrast agent " in *Proceedings of the International Society for Magnetic Resonance in Medicine*, 2012.
- [153] B. Movsas, J. D. Chapman, A. L. Hanlon, E. M. Horwitz, R. E. Greenberg, C. Stobbe, G. E. Hanks, and A. Pollack, "Hypoxic prostate/muscle po2 ratio predicts for biochemical failure in patients with prostate cancer: Preliminary findings," *Urology*, vol. 60, pp. 634-9, Oct 2002.

- [154] P. Vaupel, M. Hockel, and A. Mayer, "Detection and characterization of tumor hypoxia using po₂ histography," *Antioxid Redox Signal*, vol. 9, pp. 1221-35, Aug 2007.
- [155] M. Hockel, C. Knoop, K. Schlenger, B. Vorndran, E. Baussmann, M. Mitze, P. G. Knapstein, and P. Vaupel, "Intratatumoral po₂ predicts survival in advanced cancer of the uterine cervix," *Radiother Oncol*, vol. 26, pp. 45-50, Jan 1993.
- [156] M. Munksgaard Persson, M. E. Johansson, N. Monsef, M. Planck, S. Beckman, M. J. Seckl, L. Ronnstrand, S. Pahlman, and H. M. Pettersson, "Hif-2alpha expression is suppressed in sclc cells, which survive in moderate and severe hypoxia when hif-1alpha is repressed," *Am J Pathol*, vol. 180, pp. 494-504, Feb 2012.
- [157] Y. Luan, C. Gao, Y. Miao, Y. Li, Z. Wang, and X. Qiu, "Clinicopathological and prognostic significance of hif-1alpha and hif-2alpha expression in small cell lung cancer," *Pathol Res Pract*, vol. 209, pp. 184-9, Mar 2013.
- [158] R. Polanski, C. L. Hodgkinson, A. Fusi, D. Nonaka, L. Priest, P. Kelly, F. Trapani, P. W. Bishop, A. White, S. E. Critchlow, P. D. Smith, F. Blackhall, C. Dive, and C. J. Morrow, "Activity of the monocarboxylate transporter 1 inhibitor azd3965 in small cell lung cancer," *Clin Cancer Res*, vol. 20, pp. 926-37, Feb 15 2014.
- [159] B. Kaur, F. W. Khwaja, E. A. Severson, S. L. Matheny, D. J. Brat, and E. G. Van Meir, "Hypoxia and the hypoxia-inducible-factor pathway in glioma growth and angiogenesis," *Neuro Oncol*, vol. 7, pp. 134-53, Apr 2005.
- [160] S. M. Evans, K. W. Jenkins, H. I. Chen, W. T. Jenkins, K. D. Judy, W. T. Hwang, R. A. Lustig, A. R. Judkins, M. S. Grady, S. M. Hahn, and C. J. Koch, "The relationship among hypoxia, proliferation, and outcome in patients with de novo glioblastoma: A pilot study," *Transl Oncol*, vol. 3, pp. 160-9, Jun 01 2010.
- [161] M. Nordsmark, M. Overgaard, and J. Overgaard, "Pretreatment oxygenation predicts radiation response in advanced squamous cell carcinoma of the head and neck," *Radiother Oncol*, vol. 41, pp. 31-9, Oct 1996.
- [162] H. Minn, T. J. Gronroos, G. Komar, O. Eskola, K. Lehtio, J. Tuomela, M. Seppanen, and O. Solin, "Imaging of tumor hypoxia to predict treatment sensitivity," *Curr Pharm Des*, vol. 14, pp. 2932-42, 2008.
- [163] D. Groshar, A. J. McEwan, M. B. Parliament, R. C. Urtasun, L. E. Golberg, M. Hoskinson, J. R. Mercer, R. H. Mannan, L. I. Wiebe, and J. D. Chapman, "Imaging tumor hypoxia and tumor perfusion," *J Nucl Med*, vol. 34, pp. 885-8, Jun 1993.

- [164] J. Pacheco-Torres, P. Lopez-Larrubia, P. Ballesteros, and S. Cerdan, "Imaging tumor hypoxia by magnetic resonance methods," *NMR Biomed*, vol. 24, pp. 1-16, Jan 2011.
- [165] C. T. Lee, M. K. Boss, and M. W. Dewhirst, "Imaging tumor hypoxia to advance radiation oncology," *Antioxid Redox Signal*, vol. 21, pp. 313-37, Jul 10 2014.
- [166] P. Vaupel and A. Mayer, "The clinical importance of assessing tumor hypoxia: Relationship of tumor hypoxia to prognosis and therapeutic opportunities," *Antioxid Redox Signal*, vol. 22, pp. 878-80, Apr 01 2015.
- [167] D. Zhao, L. Jiang, and R. P. Mason, "Measuring changes in tumor oxygenation," *Methods Enzymol*, vol. 386, pp. 378-418, 2004.
- [168] M. Hoehn-Berlage, T. Tolxdorff, K. Bockhorst, Y. Okada, and R. I. Ernestus, "In vivo nmr t2 relaxation of experimental brain tumors in the cat: A multiparameter tissue characterization," *Magn Reson Imaging*, vol. 10, pp. 935-47, 1992.
- [169] A. N. Dula, D. F. Gochberg, H. L. Valentine, W. M. Valentine, and M. D. Does, "Multiexponential t2, magnetization transfer, and quantitative histology in white matter tracts of rat spinal cord," *Magn Reson Med*, vol. 63, pp. 902-9, Apr 2010.
- [170] K. D. Harkins, W. M. Valentine, D. F. Gochberg, and M. D. Does, "In-vivo multi-exponential t2, magnetization transfer and quantitative histology in a rat model of intramyelinic edema," *Neuroimage Clin*, vol. 2, pp. 810-7, 2013.
- [171] A. M. Stokes, C. P. Hart, and C. C. Quarles, "Hypoxia imaging with pet correlates with antitumor activity of the hypoxia-activated prodrug evofosfamide (th-302) in rodent glioma models," *Tomography*, vol. 2, pp. 229-237, Sep 2016.
- [172] Y. Takakusagi, S. Matsumoto, K. Saito, M. Matsuo, S. Kishimoto, J. W. Wojtkowiak, W. DeGraff, A. H. Kesarwala, R. Choudhuri, N. Devasahayam, S. Subramanian, J. P. Munasinghe, R. J. Gillies, J. B. Mitchell, C. P. Hart, and M. C. Krishna, "Pyruvate induces transient tumor hypoxia by enhancing mitochondrial oxygen consumption and potentiates the anti-tumor effect of a hypoxia-activated prodrug th-302," *PLoS One*, vol. 9, p. e107995, 2014.
- [173] B. Solomon, D. Binns, P. Roselt, L. I. Weibe, G. A. McArthur, C. Cullinane, and R. J. Hicks, "Modulation of intratumoral hypoxia by the epidermal growth factor receptor inhibitor gefitinib detected using small animal pet imaging," *Mol Cancer Ther*, vol. 4, pp. 1417-22, Sep 2005.
- [174] M. Piert, H. J. Machulla, M. Picchio, G. Reischl, S. Ziegler, P. Kumar, H. J. Wester, R. Beck, A. J. McEwan, L. I. Wiebe, and M. Schwaiger, "Hypoxia-specific tumor imaging with 18f-fluoroazomycin arabinoside," *J Nucl Med*, vol. 46, pp. 106-13, Jan 2005.

- [175] M. H. Cherk, S. S. Foo, A. M. Poon, S. R. Knight, C. Murone, A. T. Papenfuss, J. I. Sachinidis, T. H. Saunder, G. J. O'Keefe, and A. M. Scott, "Lack of correlation of hypoxic cell fraction and angiogenesis with glucose metabolic rate in non-small cell lung cancer assessed by 18f-fluoromisonidazole and 18f-fdg pet," *J Nucl Med*, vol. 47, pp. 1921-6, Dec 2006.
- [176] Y. Lin, X. Wang, and H. Jin, "Egfr-tki resistance in nslc patients: Mechanisms and strategies," *Am J Cancer Res*, vol. 4, pp. 411-35, 2014.
- [177] K. Choi, C. J. Creighton, D. Stivers, N. Fujimoto, and J. M. Kurie, "Transcriptional profiling of non-small cell lung cancer cells with activating egfr somatic mutations," *PLoS One*, vol. 2, p. e1226, 2007.
- [178] N. G. Anderson, T. Ahmad, K. Chan, R. Dobson, and N. J. Bundred, "Zd1839 (iressa), a novel epidermal growth factor receptor (egfr) tyrosine kinase inhibitor, potently inhibits the growth of egfr-positive cancer cell lines with or without erbb2 overexpression," *Int J Cancer*, vol. 94, pp. 774-82, Dec 15 2001.
- [179] D. Hanahan and R. A. Weinberg, "The hallmarks of cancer," *Cell*, vol. 100, pp. 57-70, Jan 07 2000.
- [180] J. M. Brown and W. R. Wilson, "Exploiting tumour hypoxia in cancer treatment," *Nat Rev Cancer*, vol. 4, pp. 437-47, Jun 2004.
- [181] K. O. Hicks, Y. Fleming, B. G. Siim, C. J. Koch, and W. R. Wilson, "Extravascular diffusion of tirapazamine: Effect of metabolic consumption assessed using the multicellular layer model," *Int J Radiat Oncol Biol Phys*, vol. 42, pp. 641-9, Oct 01 1998.
- [182] K. O. Hicks, F. B. Pruijn, J. R. Sturman, W. A. Denny, and W. R. Wilson, "Multicellular resistance to tirapazamine is due to restricted extravascular transport: A pharmacokinetic/pharmacodynamic study in ht29 multicellular layer cultures," *Cancer Res*, vol. 63, pp. 5970-7, Sep 15 2003.
- [183] A. H. Kyle and A. I. Minchinton, "Measurement of delivery and metabolism of tirapazamine to tumour tissue using the multilayered cell culture model," *Cancer Chemother Pharmacol*, vol. 43, pp. 213-20, 1999.
- [184] K. O. Hicks, B. G. Siim, F. B. Pruijn, and W. R. Wilson, "Oxygen dependence of the metabolic activation and cytotoxicity of tirapazamine: Implications for extravascular transport and activity in tumors," *Radiat Res*, vol. 161, pp. 656-66, Jun 2004.
- [185] W. R. Wilson, K. O. Hicks, S. M. Pullen, D. M. Ferry, N. A. Helsby, and A. V. Patterson, "Bystander effects of bioreductive drugs: Potential for exploiting

- pathological tumor hypoxia with dinitrobenzamide mustards," *Radiat Res*, vol. 167, pp. 625-36, Jun 2007.
- [186] N. D. Arvold, P. Heidari, A. Kunawudhi, L. V. Sequist, and U. Mahmood, "Tumor hypoxia response after targeted therapy in egfr-mutant non-small cell lung cancer: Proof of concept for fmiso-pet," *Technol Cancer Res Treat*, vol. 15, pp. 234-42, Apr 2016.
- [187] L. Yen, N. Benlimame, Z. R. Nie, D. Xiao, T. Wang, A. E. Al Moustafa, H. Esumi, J. Milanini, N. E. Hynes, G. Pages, and M. A. Alaoui-Jamali, "Differential regulation of tumor angiogenesis by distinct erbb homo- and heterodimers," *Mol Biol Cell*, vol. 13, pp. 4029-44, Nov 2002.
- [188] L. A. Huxham, A. H. Kyle, J. H. Baker, K. L. McNicol, and A. I. Minchinton, "Tirapazamine causes vascular dysfunction in hct-116 tumour xenografts," *Radiother Oncol*, vol. 78, pp. 138-45, Feb 2006.
- [189] L. A. Huxham, A. H. Kyle, J. H. Baker, K. L. McNicol, and A. I. Minchinton, "Exploring vascular dysfunction caused by tirapazamine," *Microvasc Res*, vol. 75, pp. 247-55, Mar 2008.
- [190] L. J. Bains, J. H. Baker, A. H. Kyle, A. I. Minchinton, and S. A. Reinsberg, "Detecting vascular-targeting effects of the hypoxic cytotoxin tirapazamine in tumor xenografts using magnetic resonance imaging," *Int J Radiat Oncol Biol Phys*, vol. 74, pp. 957-65, Jul 01 2009.
- [191] J. H. Baker, A. H. Kyle, K. L. Bartels, S. P. Methot, E. J. Flanagan, A. Balbirnie, J. D. Cran, and A. I. Minchinton, "Targeting the tumour vasculature: Exploitation of low oxygenation and sensitivity to nos inhibition by treatment with a hypoxic cytotoxin," *PLoS One*, vol. 8, p. e76832, 2013.
- [192] C. Michiels, "Physiological and pathological responses to hypoxia," *Am J Pathol*, vol. 164, pp. 1875-82, Jun 2004.
- [193] J. U. Fluckiger, M. E. Loveless, S. L. Barnes, M. Lepage, and T. E. Yankeelov, "A diffusion-compensated model for the analysis of dce-mri data: Theory, simulations and experimental results," *Phys Med Biol*, vol. 58, pp. 1983-98, Mar 21 2013.
- [194] Y. Shen, F. L. Goerner, C. Snyder, J. N. Morelli, D. Hao, D. Hu, X. Li, and V. M. Runge, "T1 relaxivities of gadolinium-based magnetic resonance contrast agents in human whole blood at 1.5, 3, and 7 t," *Invest Radiol*, vol. 50, pp. 330-8, May 2015.
- [195] Y. Wei, W. Zhao, Y. Huang, Q. Yu, S. Zhu, S. Wang, S. Zhao, X. Hu, J. Yu, and S. Yuan, "A comparative study of noninvasive hypoxia imaging with 18f-

- fluoroerythronitroimidazole and 18f-fluoromisonidazole pet/ct in patients with lung cancer," *PLoS One*, vol. 11, p. e0157606, 2016.
- [196] E. E. Verwer, R. Boellaard, and A. A. van der Veldt, "Positron emission tomography to assess hypoxia and perfusion in lung cancer," *World J Clin Oncol*, vol. 5, pp. 824-44, Dec 10 2014.
- [197] S. C. Davis, K. S. Samkoe, K. M. Tichauer, K. J. Sexton, J. R. Gunn, S. J. Deharvengt, T. Hasan, and B. W. Pogue, "Dynamic dual-tracer mri-guided fluorescence tomography to quantify receptor density in vivo," *Proc Natl Acad Sci U S A*, vol. 110, pp. 9025-30, May 28 2013.
- [198] Y. C. Tai, A. F. Chatziioannou, Y. Yang, R. W. Silverman, K. Meadors, S. Siegel, D. F. Newport, J. R. Stickel, and S. R. Cherry, "Micropet ii: Design, development and initial performance of an improved micropet scanner for small-animal imaging," *Phys Med Biol*, vol. 48, pp. 1519-37, Jun 07 2003.
- [199] H. Cho, E. Ackerstaff, S. Carlin, M. E. Lupu, Y. Wang, A. Rizwan, J. O'Donoghue, C. C. Ling, J. L. Humm, P. B. Zanzonico, and J. A. Koutcher, "Noninvasive multimodality imaging of the tumor microenvironment: Registered dynamic magnetic resonance imaging and positron emission tomography studies of a preclinical tumor model of tumor hypoxia," *Neoplasia*, vol. 11, pp. 247-59, 2p following 259, Mar 2009.
- [200] J. Jung, "Human tumor xenograft models for preclinical assessment of anticancer drug development," *Toxicol Res*, vol. 30, pp. 1-5, Mar 2014.
- [201] B. Firestone, "The challenge of selecting the 'right' in vivo oncology pharmacology model," *Curr Opin Pharmacol*, vol. 10, pp. 391-6, Aug 2010.
- [202] J. K. Peterson and P. J. Houghton, "Integrating pharmacology and in vivo cancer models in preclinical and clinical drug development," *Eur J Cancer*, vol. 40, pp. 837-44, Apr 2004.
- [203] J. J. Tentler, A. C. Tan, C. D. Weekes, A. Jimeno, S. Leong, T. M. Pitts, J. J. Arcaroli, W. A. Messersmith, and S. G. Eckhardt, "Patient-derived tumour xenografts as models for oncology drug development," *Nat Rev Clin Oncol*, vol. 9, pp. 338-50, Apr 17 2012.
- [204] B. C. Giovanella, D. M. Vardeman, L. J. Williams, D. J. Taylor, P. D. de Ipolyi, P. J. Greeff, J. S. Stehlin, A. Ullrich, R. Cailleau, D. J. Slamon, and et al., "Heterotransplantation of human breast carcinomas in nude mice. Correlation between successful heterotransplants, poor prognosis and amplification of the her-2/neu oncogene," *Int J Cancer*, vol. 47, pp. 66-71, Jan 02 1991.

- [205] M. de Jong, J. Essers, and W. M. van Weerden, "Imaging preclinical tumour models: Improving translational power," *Nat Rev Cancer*, vol. 14, pp. 481-93, Jul 2014.
- [206] F. Nemati, X. Sastre-Garau, C. Laurent, J. Couturier, P. Mariani, L. Desjardins, S. Piperno-Neumann, O. Lantz, B. Asselain, C. Plancher, D. Robert, I. Peguillet, M. H. Donnadieu, A. Dahmani, M. A. Bessard, D. Gentien, C. Reyes, S. Saule, E. Barillot, S. Roman-Roman, and D. Decaudin, "Establishment and characterization of a panel of human uveal melanoma xenografts derived from primary and/or metastatic tumors," *Clin Cancer Res*, vol. 16, pp. 2352-62, Apr 15 2010.
- [207] W. M. van Weerden and G. J. van Steenbrugge, "Human prostate tumor xenografts as representative models for clinical prostate cancer," *Urol Oncol*, vol. 2, pp. 122-5, Jul-Aug 1996.
- [208] J. Z. Press, J. A. Kenyon, H. Xue, M. A. Miller, A. De Luca, D. M. Miller, D. G. Huntsman, C. B. Gilks, J. N. McAlpine, and Y. Z. Wang, "Xenografts of primary human gynecological tumors grown under the renal capsule of nod/scid mice show genetic stability during serial transplantation and respond to cytotoxic chemotherapy," *Gynecol Oncol*, vol. 110, pp. 256-64, Aug 2008.
- [209] K. Jin, L. Teng, Y. Shen, K. He, Z. Xu, and G. Li, "Patient-derived human tumour tissue xenografts in immunodeficient mice: A systematic review," *Clin Transl Oncol*, vol. 12, pp. 473-80, Jul 2010.
- [210] R. J. Vlietstra, D. C. van Alewijk, K. G. Hermans, G. J. van Steenbrugge, and J. Trapman, "Frequent inactivation of pten in prostate cancer cell lines and xenografts," *Cancer Res*, vol. 58, pp. 2720-3, Jul 01 1998.
- [211] R. S. Kerbel, "Human tumor xenografts as predictive preclinical models for anticancer drug activity in humans: Better than commonly perceived-but they can be improved," *Cancer Biol Ther*, vol. 2, pp. S134-9, Jul-Aug 2003.
- [212] I. Fichtner, J. Rolff, R. Soong, J. Hoffmann, S. Hammer, A. Sommer, M. Becker, and J. Merk, "Establishment of patient-derived non-small cell lung cancer xenografts as models for the identification of predictive biomarkers," *Clin Cancer Res*, vol. 14, pp. 6456-68, Oct 15 2008.
- [213] Y. S. DeRose, G. Wang, Y. C. Lin, P. S. Bernard, S. S. Buys, M. T. Ebbert, R. Factor, C. Matsen, B. A. Milash, E. Nelson, L. Neumayer, R. L. Randall, I. J. Stijleman, B. E. Welm, and A. L. Welm, "Tumor grafts derived from women with breast cancer authentically reflect tumor pathology, growth, metastasis and disease outcomes," *Nat Med*, vol. 17, pp. 1514-20, Oct 23 2011.
- [214] M. Moro, G. Bertolini, M. Tortoreto, U. Pastorino, G. Sozzi, and L. Roz, "Patient-derived xenografts of non small cell lung cancer: Resurgence of an old model for

- investigation of modern concepts of tailored therapy and cancer stem cells," *J Biomed Biotechnol*, vol. 2012, p. 568567, 2012.
- [215] J. F. Jansen, H. Schoder, N. Y. Lee, Y. Wang, D. G. Pfister, M. G. Fury, H. E. Stambuk, J. L. Humm, J. A. Koutcher, and A. Shukla-Dave, "Noninvasive assessment of tumor microenvironment using dynamic contrast-enhanced magnetic resonance imaging and 18f-fluoromisonidazole positron emission tomography imaging in neck nodal metastases," *Int J Radiat Oncol Biol Phys*, vol. 77, pp. 1403-10, Aug 01 2010.
- [216] L. Bentzen, S. Keiding, M. Nordmark, L. Falborg, S. B. Hansen, J. Keller, O. S. Nielsen, and J. Overgaard, "Tumour oxygenation assessed by 18f-fluoromisonidazole pet and polarographic needle electrodes in human soft tissue tumours," *Radiother Oncol*, vol. 67, pp. 339-44, Jun 2003.
- [217] L. Bentzen, S. Keiding, M. R. Horsman, T. Gronroos, S. B. Hansen, and J. Overgaard, "Assessment of hypoxia in experimental mice tumours by [18f]fluoromisonidazole pet and po2 electrode measurements. Influence of tumour volume and carbogen breathing," *Acta Oncol*, vol. 41, pp. 304-12, 2002.
- [218] B. Gagel, P. Reinartz, E. Dimartino, M. Zimny, M. Pinkawa, P. Maneschi, S. Stanzel, K. Hamacher, H. H. Coenen, M. Westhofen, U. Bull, and M. J. Eble, "Po(2) polarography versus positron emission tomography ([18f] fluoromisonidazole, [(18)f]-2-fluoro-2'-deoxyglucose). An appraisal of radiotherapeutically relevant hypoxia," *Strahlenther Onkol*, vol. 180, pp. 616-22, Oct 2004.
- [219] L. J. Inge, *Personal Communication*.
- [220] A. Giatromanolaki, E. Sivridis, and M. I. Koukourakis, "The pathology of tumor stromatogenesis," *Cancer Biol Ther*, vol. 6, pp. 639-45, 2007.
- [221] B. A. Helfrich, D. Raben, M. Varella-Garcia, D. Gustafson, D. C. Chan, L. Bemis, C. Coldren, A. Baron, C. Zeng, W. A. Franklin, F. R. Hirsch, A. Gazdar, J. Minna, and P. A. Bunn, Jr., "Antitumor activity of the epidermal growth factor receptor (egfr) tyrosine kinase inhibitor gefitinib (zd1839, iressa) in non-small cell lung cancer cell lines correlates with gene copy number and egfr mutations but not egfr protein levels," *Clin Cancer Res*, vol. 12, pp. 7117-25, Dec 01 2006.
- [222] S. K. Chan, W. J. Gullick, and M. E. Hill, "Mutations of the epidermal growth factor receptor in non-small cell lung cancer -- search and destroy," *Eur J Cancer*, vol. 42, pp. 17-23, Jan 2006.
- [223] J. Merk, J. Rolff, M. Becker, G. Leschber, and I. Fichtner, "Patient-derived xenografts of non-small-cell lung cancer: A pre-clinical model to evaluate adjuvant chemotherapy?," *Eur J Cardiothorac Surg*, vol. 36, pp. 454-9, Sep 2009.

- [224] D. Roife, B. Dai, Y. Kang, M. V. Rios Perez, M. Pratt, X. Li, and J. B. Fleming, "Ex vivo testing of patient-derived xenografts mirrors the clinical outcome of patients with pancreatic ductal adenocarcinoma," *Clin Cancer Res*, vol. 22, pp. 6021-6030, Dec 15 2016.
- [225] I. Lohse, C. Lourenco, E. Ibrahimov, M. Pintilie, M. S. Tsao, and D. W. Hedley, "Assessment of hypoxia in the stroma of patient-derived pancreatic tumor xenografts," *Cancers (Basel)*, vol. 6, pp. 459-71, Feb 26 2014.
- [226] B. Blouw, H. Song, T. Tihan, J. Bosze, N. Ferrara, H. P. Gerber, R. S. Johnson, and G. Bergers, "The hypoxic response of tumors is dependent on their microenvironment," *Cancer Cell*, vol. 4, pp. 133-46, Aug 2003.
- [227] A. S. Fung, C. Lee, M. Yu, and I. F. Tannock, "The effect of chemotherapeutic agents on tumor vasculature in subcutaneous and orthotopic human tumor xenografts," *BMC Cancer*, vol. 15, p. 112, Mar 10 2015.
- [228] R. S. Kerbel, "Tumor angiogenesis: Past, present and the near future," *Carcinogenesis*, vol. 21, pp. 505-15, Mar 2000.
- [229] D. Hanahan and J. Folkman, "Patterns and emerging mechanisms of the angiogenic switch during tumorigenesis," *Cell*, vol. 86, pp. 353-64, Aug 09 1996.
- [230] J. Rak, J. L. Yu, G. Klement, and R. S. Kerbel, "Oncogenes and angiogenesis: Signaling three-dimensional tumor growth," *J Invest Dermatol Symp Proc*, vol. 5, pp. 24-33, Dec 2000.
- [231] J. Rak, Y. Mitsuhashi, C. Sheehan, A. Tamir, A. Vilorio-Petit, J. Filmus, S. J. Mansour, N. G. Ahn, and R. S. Kerbel, "Oncogenes and tumor angiogenesis: Differential modes of vascular endothelial growth factor up-regulation in ras-transformed epithelial cells and fibroblasts," *Cancer Res*, vol. 60, pp. 490-8, Jan 15 2000.
- [232] D. E. Richard, E. Berra, and J. Pouyssegur, "Angiogenesis: How a tumor adapts to hypoxia," *Biochem Biophys Res Commun*, vol. 266, pp. 718-22, Dec 29 1999.
- [233] A. Giatromanolaki and A. L. Harris, "Tumour hypoxia, hypoxia signaling pathways and hypoxia inducible factor expression in human cancer," *Anticancer Res*, vol. 21, pp. 4317-24, Nov-Dec 2001.
- [234] L. A. Liotta, P. S. Steeg, and W. G. Stetler-Stevenson, "Cancer metastasis and angiogenesis: An imbalance of positive and negative regulation," *Cell*, vol. 64, pp. 327-36, Jan 25 1991.
- [235] A. Maity and C. Koumenis, "Location, location, location-makes all the difference for hypoxia in lung tumors," *Clin Cancer Res*, vol. 16, pp. 4685-7, Oct 01 2010.

- [236] C. A. Cuenod and D. Balvay, "Perfusion and vascular permeability: Basic concepts and measurement in dce-ct and dce-mri," *Diagn Interv Imaging*, vol. 94, pp. 1187-204, Dec 2013.
- [237] F. Li, J. T. Joergensen, A. E. Hansen, and A. Kjaer, "Kinetic modeling in pet imaging of hypoxia," *Am J Nucl Med Mol Imaging*, vol. 4, pp. 490-506, 2014.
- [238] O. Schimpf, S. Hindel, and L. Ludemann, "Assessment of micronecrotic tumor tissue using dynamic contrast-enhanced magnetic resonance imaging," *Phys Med*, vol. 34, pp. 38-47, Feb 2017.
- [239] V. A. Bourke, D. Zhao, J. Gilio, C. H. Chang, L. Jiang, E. W. Hahn, and R. P. Mason, "Correlation of radiation response with tumor oxygenation in the dunning prostate r3327-at1 tumor," *Int J Radiat Oncol Biol Phys*, vol. 67, pp. 1179-86, Mar 15 2007.
- [240] D. Zhao, A. Constantinescu, C. H. Chang, E. W. Hahn, and R. P. Mason, "Correlation of tumor oxygen dynamics with radiation response of the dunning prostate r3327-hi tumor," *Radiat Res*, vol. 159, pp. 621-31, May 2003.
- [241] V. D. Kodibagkar, X. Wang, and R. P. Mason, "Physical principles of quantitative nuclear magnetic resonance oximetry," *Front Biosci*, vol. 13, pp. 1371-84, 2008.
- [242] J. P. Korb and R. G. Bryant, "Magnetic field dependence of proton spin-lattice relaxation times," *Magn Reson Med*, vol. 48, pp. 21-6, Jul 2002.
- [243] P. A. Bottomley, T. H. Foster, R. E. Argersinger, and L. M. Pfeifer, "A review of normal tissue hydrogen nmr relaxation times and relaxation mechanisms from 1-100 mhz: Dependence on tissue type, nmr frequency, temperature, species, excision, and age," *Med Phys*, vol. 11, pp. 425-48, Jul-Aug 1984.
- [244] S. K. Sharma, K. C. Lowe, and S. S. Davis, "Emulsification methods for perfluorochemicals," *Drug Development and Industrial Pharmacy*, vol. 14, pp. 2371-2376, 1988.
- [245] W. A. Bruggeman, D. Weberfung, A. Opperhuizen, J. Vandersteen, A. Wijnbenga, and O. Hutzinger, "Absorption and retention of polydimethylsiloxanes (silicones) in fish - preliminary experiments," *Toxicological and Environmental Chemistry*, vol. 7, pp. 287-296, 1984.
- [246] S. Xu and B. Kropscott, "Evaluation of the three-phase equilibrium method for measuring temperature dependence of internally consistent partition coefficients (k_{ow}), k_{oa}), and k_{aw}) for volatile methylsiloxanes and trimethylsilanol," *Environ Toxicol Chem*, vol. 33, pp. 2702-10, Dec 2014.

- [247] J. U. Menon, P. K. Gulaka, M. A. McKay, S. Geethanath, L. Liu, and V. D. Kodibagkar, "Dual-modality, dual-functional nanoprobe for cellular and molecular imaging," *Theranostics*, vol. 2, pp. 1199-207, 2012.
- [248] R. P. Mason, "Non-invasive physiology: ^{19}F nmr of perfluorocarbons," *Artif Cells Blood Substit Immobil Biotechnol*, vol. 22, pp. 1141-53, 1994.

APPENDIX A

MORE BULLETS FOR PISTOL: LINEAR SILOXANE REPORTER PROBES FOR ^1H
OXIMETRY

A.1 ABSTRACT

We have previously reported the ability of HMDSO and HMDSO based nano-emulsions for accurate and repeated measurements of oxygen using the PISTOL technique. In this study, we report the feasibility of linear siloxanes hexadimethylsiloxane (HMDSO) octamethyltrisiloxane, (OMTSO) and polydimethylsiloxane (PDMSO) oxygen reporter molecules. The spin-lattice relaxation rate of all the siloxanes exhibited a linear relationship with the oxygenation (R_1 versus pO_2): R_1 (s^{-1}) = $0.1105 \pm 0.0011 * pO_2$, $0.1497 \pm 0.0013 * pO_2$ and $0.2091 \pm 0.0012 * pO_2$ at 7 T and 37 °C for neat HMDSO, OMTSO and PDMSO respectively. The sensitivity index decreased with an increase in chain length and the values ranged from $7.5 - 11.5 \times 10^{-3} \text{ torr}^{-1}$. We observed no substantial change in the relaxation time at higher magnetic fields for HMDSO and OMTSO, thus indicating no substantial increase in imaging time. A small temperature dependence (approximately 1-2 torr/ °C) in the calibration curves for HMDSO, OMTSO and PDMSO at higher magnetic fields was observed, similar to the previous report on neat HMDSO at 4.7 T. In summary, we have demonstrated the feasibility of various linear and cyclic siloxanes as pO_2 -sensing probes for 1H MR oximetry.

A.2 Introduction

The ^{19}F NMR oximetry uses exogenous perfluorocarbon reporters such as perfluoro-15-crown-5-ether (15C5[145]) as oxygen reporters. FREDOM (Fluorocarbon Relaxometry using Echo planar imaging for Dynamic Oxygen Mapping) is a technique that exploits the linear relationship of hexafluorobenzene (HFB) with oxygenation. Our group has previously shown the feasibility of accurate and repeated measurements of oxygen using HFB and hexamethyldisiloxane (HMDSO) in thigh and tumor regions in-vivo using the

^{19}F and ^1H NMR spectroscopy and imaging based sequences [141, 239-241] respectively. We have also shown the ability of HMDSO based nano-emulsions for tissue oximetry [146]. In this study, we have further characterized the calibration curves of various linear siloxanes and their utility as pO_2 sensing reporter molecules. The siloxanes characterized in this study are: linear siloxanes hexamethyldisiloxane, octamethyltrisiloxane (OMTSO), and polydimethylsiloxane (PDMSO, trimethylsiloxy terminated, M.W. 410) at 7 T.

A.3 Materials & methods

Preparation of siloxane samples for R_1 calibration

The linear siloxanes hexamethyldisiloxane (HMDSO), octamethyltrisiloxane (OMTSO), and polydimethylsiloxane (PDMSO) were purchased from Sigma-Aldrich (St. Louis, MO). All the materials were used as received.

For the sample preparation, each siloxane was placed in 4 gas-tight NMR glass tubes (Wilmad Taperlok 528SJH, Buena, NJ) and saturated by bubbling for 15 minutes with varying standard of gases including 0%, 5%, 10%, and 21% O_2 (balance N_2), respectively. Gases with varying oxygen concentrations were made by mixing nitrogen and air in varying proportions in a HypoxyDial™ (STARR Life Sciences Corp.; Oakmont, PA, USA). A pO_2 meter was connected in line with the output of the HypoxyDial™ in order to verify the accuracy of the HypoxyDial™. The tubes were then sealed. For measurement of the temperature dependence of T_1 , the temperature of the

water pad was varied between 17 to 52 °C. A fiber optic probe (FISO Technologies Inc., Quebec, Canada) was used to measure the temperature of the tubes.

MRI experiments were performed on a Bruker BioSpec 7 T horizontal bore system equipped with actively shielded gradients. The tubes were placed together on a pad with circulating water and imaged using a volume transceiver coil [146]. At all the magnetic field strengths T_1 was measured as a function of temperature in the physiologically relevant range of 17-52 °C. T_1 measurements were performed after the tube temperature was allowed to equilibrate at the desired value for 10-20 min.

Pulse sequence for measuring pO_2

A frequency selective 1H NMR spectroscopy based sequence as described in detail in reference [140] was used for determination of T_1 of the prepared samples at 4.7 T. A 1H MR spin-echo imaging based sequence as described in detail in reference [141] and an inversion recovery based sequence was used for T_1 determination at 7 T. T_1 data were fit to a single exponential, 3-parameter saturation-recovery equation (refer to equation [1]) using the Levenberg-Marquardt algorithm. The data at each temperature was then fit into the equations 1-3 to obtain the corresponding calibration constants and T_1 values.

$$R_1 = A' + B' * pO_2 \quad [1]$$

Where, A' is the diamagnetic i.e. anoxic component and B' is the paramagnetic component that is dependent on pO_2 .

The temperature dependence of the A' and B' components can be approximated as:

$$A' = A + C * T$$

$$B' = B + D * T \quad [2]$$

Thus, a temperature dependent model for estimation of pO_2 can be obtained by substituting the values from equation 1.8 in equation 1.7.

$$R_1 = A + B * pO_2 + C * T + D * T * pO_2 \quad [3]$$

The above equation can be used to determine oxygenation levels as well as errors in estimation $pO_2/^\circ C$, thus providing a more accurate and reliable quantification. The following equation can be used to determine error in pO_2 determination for change in temperature by $1^\circ C$ at a particular temperature T and oxygenation level:

$$\frac{\Delta pO_2}{\Delta T} = \frac{|C + D * pO_2|}{B + D * T} \quad [4]$$

Calculation of error in pO_2 determination

Using the characterization parameters A, B, C, D, the relative errors in the pO_2 determination were calculated at all the field strength using equation [4] for oxygenation levels in relevant a hypoxic range (0 Torr to 50 Torr) at $37^\circ C$ and for a change in temperature by $1^\circ C$.

A.4 Results

Calibration of HMDSO at 7 T

The calibration of HMDSO was conducted at 7 T to study the effect of variation of pO_2 and temperature on R_1 of HMDSO. R_1 values were obtained as a function of pO_2 while the temperature was kept constant. The acquired R_1 vs. temperature data was fit to the linear model described before to yield the calibration constants A' and B' at 7 T (figure A.1). The R_1 of the HMDSO showed a linear dependence with the pO_2 at a fixed temperature.

A' and B' were then plotted with respect to variations in temperature, in the physiologically relevant range of 17°C to 48°C , to yield characterization parameters A, B C and D at 7 T (figure A.1 C & D). For pO_2 of 5 Torr, the resulting error in pO_2 determination for a change in temperature by 1°C at 37°C was $\sim 0.1 \text{ Torr}/^\circ\text{C}$ at 7 T.

Table A.1: Calibration constants of HMDSO at 7 T and 9.4 T.

Magnetic field strength	A (s ⁻¹)	B (s*Torr) ⁻¹	C (s*°C) ⁻¹	D (s*Torr*°C) ⁻¹	Intercept A' (s ⁻¹) 37°C	Slope B' (s*torr) ⁻¹ 37°C	η (X10 ⁻³) =B'/A'
7 T	0.15 ± 2 x 10 ⁻³	0.0014 ± 3.09 x 10 ⁻⁵	-0.00103 ± 4.14 x 10 ⁻⁵	-9.44E-06 ± 8.87 x 10 ⁻⁷	0.11056 ± 6.54x10 ⁻⁴	0.00108 ± 1.7x10 ⁻⁵	9.7
9.4 T	0.1621 ± 3.45 x 10 ⁻⁴	0.0015 ± 8.17 x 10 ⁻⁶	-0.0014 ± 1.77 x 10 ⁻⁵	-7.75E-06 ± 3.5 x 10 ⁻⁷	0.11068425	0.0012 ± 8.81x10 ⁻⁶	11.33

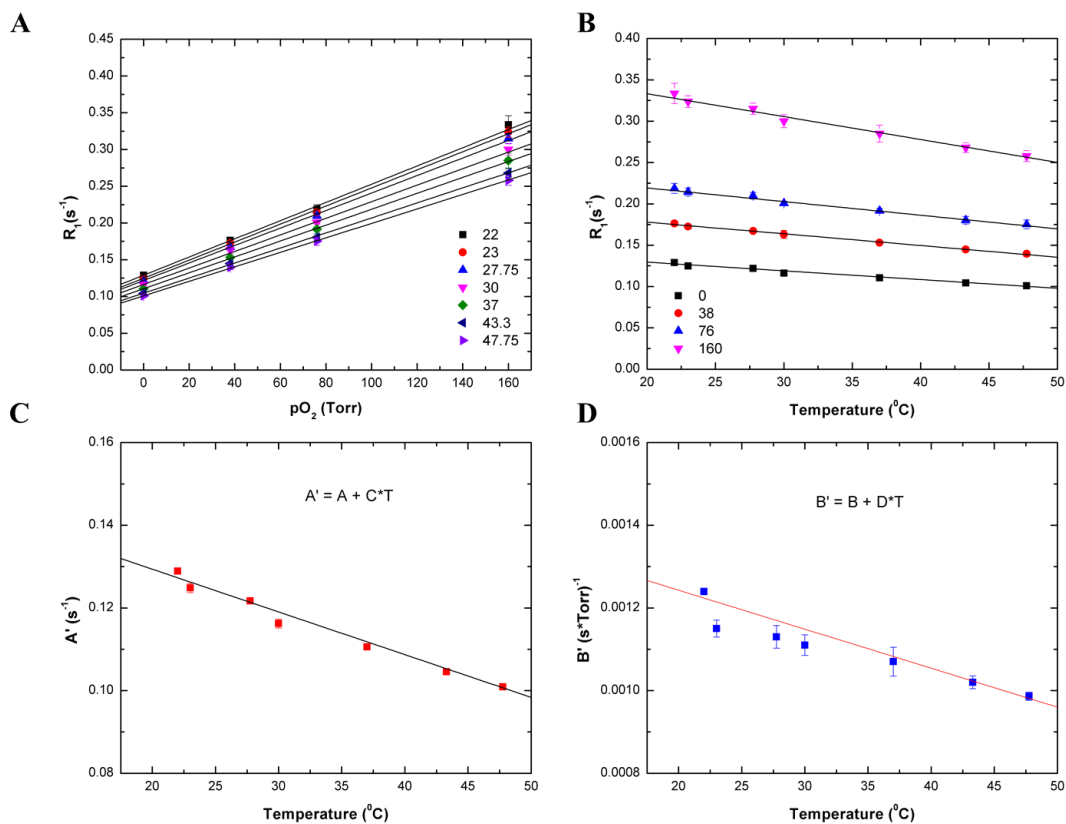


Figure A.1: Neat HMDSO R_1 dependence on pO_2 at different temperatures at 7 T.

Calibration of Octamethyltrisiloxane (OMTSO) at 7 T

OMTSO is a symmetric molecule with a single NMR resonance close to that of tetramethylsilane (TMS). OMTSO has characteristics similar to that of HMDSO and its R_1 showed a linear dependence on pO_2 . Calibration of OMTSO was done at 7 T and the acquired R_1 vs. temperature data was fit to the linear model described before to yield the calibration constants A' and B' .

The temperature dependence of constants A' and B' was determined by linear fitting the constants at different temperatures at 7 T. The error in pO_2 determination for a 1°C change in temperature was calculated to be $\sim 1 \text{ Torr}/^\circ\text{C}$ for a pO_2 of 5 Torr at 7 T.

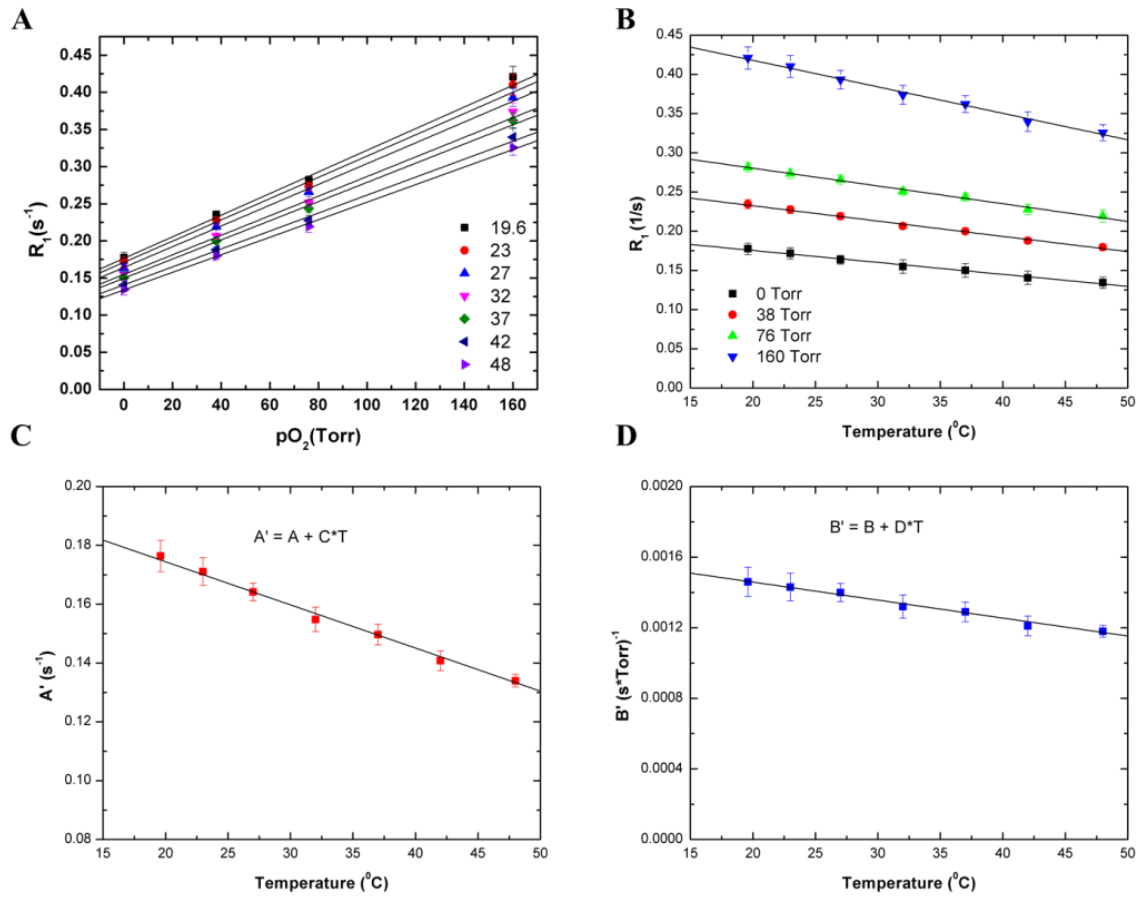


Figure A.2: Neat OMTSO R_1 dependence on pO_2 at different temperatures at 7 T

Table A.2: Calibration constants of OMTSO at 4.7 T, 7 T and 9.4 T.

Magnetic field strength	A (s ⁻¹)	B (s*Torr) ⁻¹	C (s*°C) ⁻¹	D (s*Torr*°C) ⁻¹	Intercept A' (s ⁻¹) 37°C	Slope B' (s*torr) ⁻¹ 37°C	η (X10 ⁻³) =B'/A'
4.7 T	0.2295 ± 2.1 x 10 ⁻³	0.002 ± 4.1x10 ⁻⁵	-2.09x10 ⁻⁵ ± 1.2x10 ⁻⁶	-2.09x10 ⁻⁵ ± 1.2x10 ⁻⁶	0.1555	0.0013 ± 2.66x10 ⁻⁵	10.4
7 T	0.2040 ± 1.8 x 10 ⁻³	0.0016 ± 2.17x10 ⁻⁵	-0.0015 ± 4.75 x10 ⁻⁵	-1.02x10 ⁻⁶ ± 5.56 x10 ⁻⁷	0.1497	0.0013 ± 5.55 x10 ⁻⁵	8.68
9.4 T	0.1985 ± 1.5 x 10 ⁻³	0.0015 ± 6.2x10 ⁻⁵	-0.0015 ± 5.3x10 ⁻⁵	-1.016x10 ⁻⁶ ± 2.05x10 ⁻⁶	0.143	0.0014 ± 8.66x10 ⁻⁵	10.4

Calibration of polydimethylsiloxane at 7 T

PDMSO (M.W. 410) is a polymer of dimethylsiloxane with a viscosity of 2 centistokes. The temperature dependence of constants A' and B' was determined by linear fitting the constants at different temperatures at 7 T (figure A.3). At 7 T the values were $A = 0.29023 \pm 0.0036 \text{ s}^{-1}$, $C = -0.0022 \pm 9.53 \times 10^{-5} (\text{s} \cdot ^\circ\text{C})^{-1}$ (figure A.3 C) and $B = 0.0015 \pm 3.13 \times 10^{-5} (\text{s} \cdot \text{Torr})^{-1}$ and $D = -8.61 \times 10^{-6} \pm 8.22 \times 10^{-7} (\text{s} \cdot \text{Torr} \cdot ^\circ\text{C})^{-1}$ (figure A.3 D). The error in $p\text{O}_2$ determination for a 1°C change in temperature was calculated to be $\sim 1.9 \text{ Torr}/^\circ\text{C}$ for a $p\text{O}_2$ of 5 Torr at 7 T (figure A.4 C).

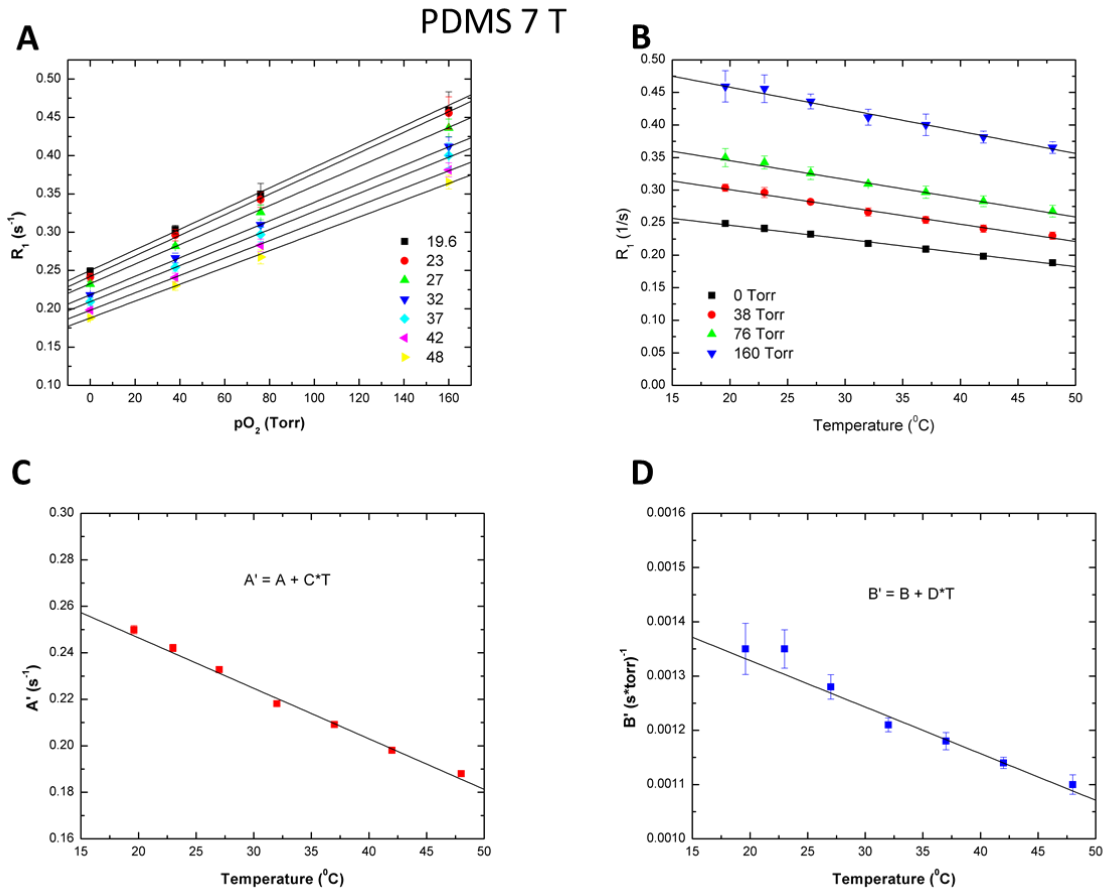


Figure A.3: Neat PDMSO R_1 dependence on $p\text{O}_2$ at 7 T.

Table A.3: Calibration constants of PDMSO at 7 T.

Magnetic field strength	A (s ⁻¹)	B (s*Torr) ⁻¹	C (s*°C) ⁻¹	D (s*Torr*°C) ⁻¹	Intercept A' (s ⁻¹) 37°C	Slope B' (s*torr) ⁻¹ 37°C	η (X10 ⁻³) =B'/A'
7 T	0.29023 ± 3.6 x 10 ⁻³	0.0015 ± 3.13x10 ⁻⁵	-0.0022 ± 9.53x10 ⁻⁵	8.61x10 ⁻⁶ ± 8.22x10 ⁻⁷	0.2091 ± 7.79x10 ⁻⁴	0.0012± 1.59x10 ⁻⁵	5.6

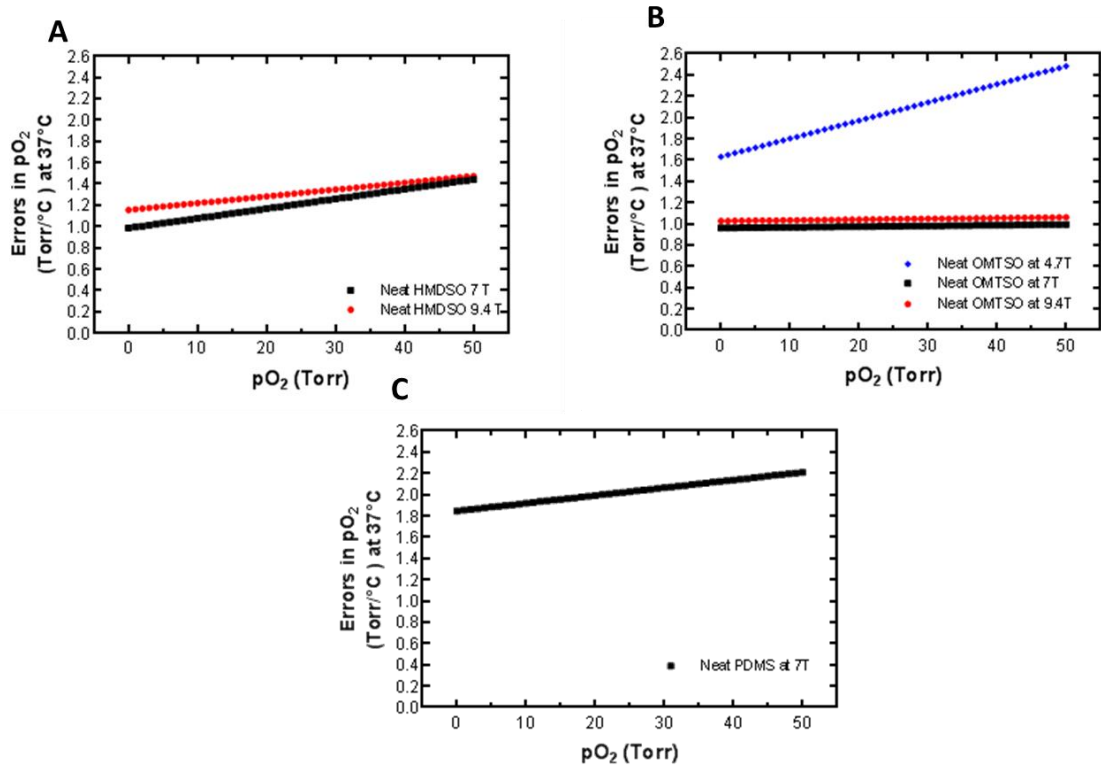


Figure A.4: The comparison of simulated error in pO₂ determination for neat (A) HMDSO, (B) OMTSO and (C) PDMSO with a 1°C change in temperature in a hypoxia relevant pO₂ range at 37°C at 4.7, 7 and 9.4 T.

A.5 Discussion

Accurate assessment of oxygenation is vital for monitoring tissue and organ functions and also for the diagnosis and characterization of pathophysiology. PISTOL has been established as a quantitative oximetry technique that allows for accurate, non-invasive and repeated measurement of tissue oxygenation. HMDSO has been characterized as the oxygen reporter agent and HMDSO based nanoemulsions have also shown their ability to report oxygenation in-vivo at 4.7 T [146]. Measuring tissue

oxygenation using siloxanes at higher magnetic field strength has the following advantages: 1) species have larger chemical shift separation between them which aids in selective excitation, 2) increase in net magnetization ($M_0 \propto B_0$). It is well known that at higher magnetic fields the relaxation time gets longer (for small molecules) which might result in an increase in the total imaging time [242, 243]. Our goal was to evaluate the relationship of T_1 s of HMDSO and OMTSO at 7 T and 9.4 T and also help in determining the choice of siloxane (smaller dynamic range of T_1 's across the pO_2 range) for applications requiring faster time resolution. Our results suggest that for neat HMDSO at 7 T, T_1 at 37°C ranged from 9 seconds ($pO_2=0$ Torr) to 3.5 seconds ($pO_2=160$ Torr) and at 9.4 T, T_1 ranged from 9 seconds ($pO_2=0$ Torr) to 3.21 seconds ($pO_2=160$ Torr) which differed by $\sim 2\%$ from T_1 obtained at 4.7 T [140] indicating no substantial increase in imaging time. Also, the calculated error in pO_2 determination as given by Equation [8] at 37°C for 1°C change in temperature was ~ 0.1 Torr/°C at 7 T and ~ 1.18 Torr/°C at 9.4 T when the actual pO_2 value was 5 Torr. Since the imaging time at 7 T and 9.4 T was same as for 4.7 T with no significant increase of error in pO_2 determination, imaging of HMDSO would be desired at higher magnetic field strengths. Similarly for OMTSO the T_1 ranged from 6.4 seconds at 4.7 T to 6.7 seconds at 7 T and 7 seconds at 9.4 T ($pO_2=0$ Torr) and from 2.1 seconds at 4.7 T to 2.7 at 7 T and 2.6 seconds at 9.4 T ($pO_2=160$ Torr). Thus, the changes in the T_1 did not result in a substantial increase in the imaging time for OMTSO.

The calibration of OMTSO and PDMSO demonstrated that longitudinal relaxation rate of both the siloxanes varied linearly with respect to changes in pO_2 ,

demonstrating the potential of OMTSO and PDMSO to measure dynamic changes in tissue pO_2 following intramuscular injection. At a constant temperature of 37°C OMTSO ($B'_{OMTSO@4.7 T} = 0.0013 \pm 2.66 \times 10^{-5}$, $B'_{OMTSO@7 T} = 0.0013 \pm 5.55 \times 10^{-5}$, $B'_{OMTSO@9.4 T} = 0.0014 \pm 8.66 \times 10^{-5}$) and PDMSO ($B'_{PDMSO@7 T} = 0.0012 \pm 1.59 \times 10^{-5}$) had oxygen sensitivity similar to HMDSO ($B'_{HMDSO@4.7 T} = 0.0013 \pm 5.5 \times 10^{-5}$, $B'_{HMDSO@7 T} = 0.00108 \pm 1.7 \times 10^{-5}$, $B'_{HMDSO@9.4 T} = 0.0012 \pm 8.81 \times 10^{-6}$). Another important observation was that PDMSO had higher anoxic relaxation rate (A') compared to neat HMDSO at 7 T and OMTSO at 7 T. OMTSO also had higher anoxic relaxation rate (A') compared to neat HMDSO at 4.7 T, 7 T and 9.4 T respectively. The higher anoxic relaxation rate indicates faster T_1 for the siloxanes which can be further exploited to map tissue oxygenation faster than HMDSO. It should be also noted that the boiling point of neat OMTSO (153°C) is higher than the boiling point of neat HMDSO (101°C) and neat PDMSO (85-105 °C) thus OMTSO is advantageous for the emulsification process as it would be less volatile during the emulsification process [244]. The errors in pO_2 determination for OMTSO as well as PDMSO were found to be in the same range as HMDSO at 4.7 T, 7 T and 9.4 T respectively at an actual pO_2 of 5 Torr with change in temperature by 1°C at 37°C. Thus, OMTSO and PDMSO can be identified as a promising pO_2 probe which could enable faster mapping of tissue oxygenation than HMDSO. Alternatively, for applications requiring faster time resolution, one can use cyclic or long chain linear siloxanes as the reporter molecules because of their smaller dynamic range of T_1 s.

As stated before, at a given temperature (and magnetic field) the linear relationship between pO_2 and temperature (defined by equation [4]) determines the

sensitivity of R_1 to changes in pO_2 . The ratio $\eta = \text{slope/intercept} (B'/A')$ is a parameter that helps in determining the sensitivity index of different MRI pO_2 reporter molecules. A larger slope and smaller intercept represents greater sensitivity to changes in pO_2 but also indicates longer imaging times. We observed a decrease in η with respect to an increase in chain length of the linear siloxanes and the η values ranged from $7.5 - 11.5 \times 10^{-3} \text{ torr}^{-1}$.

The octanol-water partition coefficient (K_{OW}) defines the hydrophobicity and lipophilicity of a compound and a higher K_{OW} represents higher hydrophobicity [245]. The octanol-water partition coefficient of HMDSO is 4.2 [245], octamethyltrisiloxane is 4.8 [245], decamethyltetrasiloxane is 5.4 [245], dodecamethylpentasiloxane is 6 [245], octamethylcyclotetrasiloxane (OMCTSO) is 6.98 [246] and decamethylcyclopentasiloxane (DMCPSO) is 8.09 [246] at $\sim 25^\circ\text{C}$. As evident, the hydrophobicity of organic siloxanes increases with increasing molecular weight.

Our previous studies have shown the feasibility of measuring oxygenation via direct injection of siloxanes into the region of interest. The direct injection of neat siloxane or nano-emulsions ensures the delivery of a sufficient dosage of the probe over the entire tissue or tumor, although this method of delivering the reporter agent is limited to regions that are accessible. Siloxane based nano-emulsions with systemic deliverability needs to be developed in order to map the oxygenation of inaccessible regions. Various HMDSO based oil in water nanoemulsions have been synthesized successfully using PEGylated non-ionic surfactant and have been characterized with respect to changes in pO_2 and temperature [146, 247]. These nanoemulsions have oxygen sensitivity similar to

neat HMDSO indicating potential of and being used as a pO₂ probes following systemic delivery.

In summary, we have demonstrated for the first time the feasibility of various linear and cyclic siloxanes as pO₂-sensing probes for ¹H MR oximetry. These siloxanes of different chain lengths with a broad range of boiling points, hydrophobicity and dynamic range of T₁s can be used for diversifying the application of ¹H MR oximetry. With systemic delivery for tissue oximetry in mind, we plan to further synthesize siloxane based nano-emulsions and optimize the synthesis procedure to obtain smaller sized nanoprobe, which could improve uptake in regions with restricted vascularization and reduce the bias in delivery to well vascularized regions as has been seen with the use of microemulsions [248].

APPENDIX B
PERMISSION TO USE FIGURES

1. Permission to reproduce and modify Figure 1.2 A

NATURE PUBLISHING GROUP LICENSE TERMS AND CONDITIONS

Apr 04, 2017

This Agreement between Shubhangi Agarwal ("You") and Nature Publishing Group ("Nature Publishing Group") consists of your license details and the terms and conditions provided by Nature Publishing Group and Copyright Clearance Center.

License Number	4082020851354
License date	Apr 04, 2017
Licensed Content Publisher	Nature Publishing Group
Licensed Content Publication	Oncogene
Licensed Content Title	Vascular remodeling in cancer
Licensed Content Author	R H Farnsworth, M Lackmann, M G Achen and S A Stacker
Licensed Content Date	Aug 5, 2013
Licensed Content Volume	33
Licensed Content Issue	27
Type of Use	reuse in a dissertation / thesis
Requestor type	academic/educational
Format	print and electronic
Portion	figures/tables/illustrations
Number of figures/tables/illustrations	1
High-res required	no
Figures	Figure 3
Author of this NPG article	no
Your reference number	
Title of your thesis / dissertation	MRI Guided Analysis of Changes in Tumor Oxygenation in Response to Hypoxia Activated/Targeted Therapeutics
Expected completion date	May 2017
Estimated size (number of pages)	160

3. Permission to reproduce and modify Figure 1.2 B

ELSEVIER LICENSE TERMS AND CONDITIONS

Apr 04, 2017

This Agreement between Shubhangi Agarwal ("You") and Elsevier ("Elsevier") consists of your license details and the terms and conditions provided by Elsevier and Copyright Clearance Center.

License Number	4082020731448
License date	Apr 04, 2017
Licensed Content Publisher	Elsevier
Licensed Content Publication	Pharmacology & Therapeutics
Licensed Content Title	Modulation of the tumor vasculature and oxygenation to improve therapy
Licensed Content Author	Dietmar W. Siemann,Michael R. Horsman
Licensed Content Date	September 2015
Licensed Content Volume	153
Licensed Content Issue	n/a
Licensed Content Pages	18
Start Page	107
End Page	124
Type of Use	reuse in a thesis/dissertation
Intended publisher of new work	other
Portion	figures/tables/illustrations
Number of figures/tables/illustrations	1
Format	both print and electronic
Are you the author of this Elsevier article?	No
Will you be translating?	No
Order reference number	
Original figure numbers	Figure 1 B

Title of your thesis/dissertation	MRI Guided Analysis of Changes in Tumor Oxygenation in Response to Hypoxia Activated/Targeted Therapeutics
Expected completion date	May 2017
Estimated size (number of pages)	160
Elsevier VAT number	GB 494 6272 12
Requestor Location	Shubhangi Agarwal 550 E. Orange St. # 181 CA TEMPE, AZ 85281 United States Attn: Shubhangi Agarwal
Publisher Tax ID	98-0397604
Total	0.00 USD

APPENDIX C

APPROVAL DOCUMENTS FOR STUDIES INVOLVING ANIMAL SUBJECTS

Institutional Animal Care and Use Committee (IACUC)

Office of Research Integrity and Assurance

Arizona State University

660 South Mill Avenue, Suite 315

Tempe, Arizona 85287-6111

Phone: (480) 965-4387 FAX: (480) 965-7772

Animal Protocol Review

ASU Protocol Number: 15-1433R
Protocol Title: Probes for Imaging Tumor Vulnerability
Principal Investigator: Vikram Kodibagkar
Date of Action: 04/23/2015

The animal protocol review was considered by the Committee and the following decisions were made:

The protocol was approved by Full Committee Review as presented.

If you have not already done so, documentation of Level III Training (i.e., procedure-specific training) will need to be provided to the IACUC office before participants can perform procedures independently. For more information on Level III requirements see <https://researchintegrity.asu.edu/training/animals/levelthree>.

Total # of Animals: 456
Species: Mice Pain Level: D-382
Species: Rats Pain Level: D-74
Protocol Approval Period: 04/23/2015 – 04/22/2018

Sponsor: N/A
ASU Proposal/Award #: N/A
Title: N/A

Signature: C. Johnson Date: 4/30/15
IACUC Chair or Designee

Cc: IACUC Office
IACUC Chair

Institutional Animal Care and Use Committee (IACUC)

Office of Research Integrity and Assurance

Arizona State University

660 South Mill Avenue, Suite 315

Tempe, Arizona 85287-6111

Phone: (480) 965-4387 FAX: (480) 965-7772

Animal Protocol Review

ASU Protocol Number: 15-1433R Amendment #1
Protocol Title: Probes for Imaging Tumor Vulnerability
Principal Investigator: Vikram Kodibagkar
Date of Action: 5/28/2015

The animal protocol review was considered by the Committee and the following decisions were made:

**The amendment was approved by Full Committee Review to add
new procedures to the protocol.**

If you have not already done so, documentation of Level III Training (i.e., procedure-specific training) will need to be provided to the IACUC office before participants can perform procedures independently. For more information on Level III requirements see <https://researchintegrity.asu.edu/training/animals/levelthree>.

Total # of Animals: 456
Species: Rats **Pain Level: D-74**
Species: Mice **Pain Level: D-382**

Protocol Approval Period: 4/23/2015 – 4/22/2018

Sponsor: N/A
ASU Proposal/Award #: N/A
Title: N/A

Signature: Augustouli for C Johnson Date: 6/3/2015
IACUC Chair or Designee

Cc: IACUC Office
IACUC Chair